# UNIVERSITY OF SOUTHAMPTON

FACULTY OF ENGINEERING, SCIENCE AND MATHEMATICS

School of Chemistry


## Gold Based Electrocatalysts


By

**Prabalini Kannan**


Thesis for the degree of Doctor of Philosophy

February 2011

UNIVERSITY OF SOUTHAMPTON

ABSTRACT

FACULTY OF ENGINEERING, SCIENCE AND MATHEMATICS

School of Chemistry

Doctor of Philosophy

# GOLD BASED ELECTROCATALYSTS

By Prabalini Kannan

Gold electrocatalysts have been of growing interest in recent years owing to their reactivity for a variety of important reactions such as the oxygen reduction reaction. This activity has been shown to be dependent on the size of the supported electrocatalyst nanoparticles. In this thesis the effects of Au nanoparticle size are explored for the oxygen reduction, ethanol oxidation and carbon monoxide oxidation reactions (Chapter four). The results show the oxygen reduction and ethanol oxidation reactions were favoured using larger particles, 6 nm in diameter, whilst the CO oxidation reaction was more facile on smaller particles, 3 nm in diameter. The effects of size are attributed to the size dependent strength of the Au-O (H) bond. Modified Au nanoparticles, in which the Au serves as a core for a Pt or Pd shell have also been of recent interest, as Au has been less expensive than Pt. These core-shell electrocatalysts thus affect both cost and activity advantages as the underlying Au core affect the properties of the shell. In this thesis the effects of the particle size of the Au core on the activity of Pt or Pd shells have been investigated (Chapter five). The results show that the oxygen reduction reaction is well again more facile when the core size is larger, whilst the ethanol oxidation reaction now is favoured with the small Au core size. The coverage of Pt or Pd on the Au core was also found to be dependent on the particle size, with smaller particles being covered by thinner shells. Thus, the size dependence of the oxygen reduction activity is once again attributed to O (H) coverage and bond strength, whilst the ethanol oxidation is attributed to either an electronic perturbation of the Pt or Pd by the Au core of an ensemble effect.

TABLE OF CONTENTS

**ABSTRACT.....III**

**TABLE OF CONTENTS..... V**

**DECLARATION OF AUTHORSHIP..... IX**

**ACKNOWLEDGEMENTS..... XI**

**Chapter One Introduction.....1**

1. Catalysis..... 1
2. Electrocatalysis.....2
3. Gold Electrochemistry..... 9
4. Bimetallic catalysts.....11
   - 4.1 Alloys ..... 11
   - 4.2 Core-shell catalysts .....12
5. Aims and Objectives..... 14
6. References..... .17

**Chapter Two Experimental Methods And Techniques.....21**

1. Reagents and Materials.....21
2. Preparation of gold electrocatalysts.....22
   - 2.1 Synthesis of nanoparticles.....22
   - 2.2 Loading on carbon.....23
   - 2.3 Heat treatment process .....23
3. Characterization of prepared catalysts.....24
   - 3.1 Transmission Electron Microscopy (TEM) .....24
     - 3.1.1 TEM measurements by JM .....24
   - 3.2 X-ray Diffraction Analysis (XRD).....26
     - 3.2.1 XRD measurement by JM.....29
   - 3.3 X- Ray absorption spectroscopy (XAS).....30
     - 3.3.1 XAS measurements.....32
   - 3.4 Electrochemical characterizations.....32
     - 3.4.1 Ink preparation .....33

3.4.2 Electrode preparation ..... 33
3.4.3 Cell and Instrumentation ..... 34
3.4.4 Cyclic voltammetry ..... 35
4. References ..... 42

**Chapter Three Characterisations of Catalysts ..... 43**
1. Introduction ..... 43
2. Results and Discussion ..... 43
2.1 Elemental analysis ..... 43
2.2 TEM ..... 44
2.3 XRD ..... 46
2.4 XAS ..... 49
2.5 Cyclic Voltammogram (CV) ..... 51
2.6 UPD ..... 53
2.7 Comparison of Techniques ..... 56
3. References ..... 58

**Chapter Four Particle Size Effect ..... 59**
1. Oxygen Reduction Reaction (ORR) ..... 59
1.1 Introduction ..... 59
1.2 Experimental procedure ..... 65
1.3 Results and Discussion ..... 66
1.3.1 CVs in Alkaline media ..... 66
1.3.2 Oxygen reduction on bulk gold ..... 67
1.3.3 Oxygen reduction on Au/C catalysts ..... 72
2. CO Oxidation Reaction ..... 78
2.1 Introduction ..... 78
2.2 Experimental ..... 81
2.3 Results and Discussion ..... 82
2.3.1 CO oxidation on bulk gold ..... 82
2.3.2 CO oxidation on Au/C catalysts ..... 84
3. Ethanol Oxidation Reaction ..... 90
3.1 Introduction ..... 90

3.2 Experimental procedure ....93
3.3 Results and Discussion....94
3.3.1 Ethanol oxidation on bulk gold....94
3.3.2 Ethanol oxidation on Au/C catalysts....96
4. Conclusion....100
5. References....102

**Chapter Five Modification of the Surface Core-Shell Catalysts....111**
1. Preparation of Core – Shell catalysts....107
2. CV characteristics of the core–shell catalysts....112
2.1 Pt modified Au catalysts ....112
2.1.1 Voltammetric features of the 20 wt % Pt/C ....112
2.1.2 Voltammetric features of the Pt modified Au catalysts ....115
2.2 Pd modified Au catalysts ....118
2.2.1 Voltammetric features of the 20 wt % Pd/C ....118
2.2.2 Voltammetric features of the Pd modified Au catalysts ....121
3. Oxygen Reduction Reaction (ORR).... 123
3.1 ORR on 20 wt % Pt/C....123
3.2 ORR on Pt modified Au catalysts ....125
3.3 Pd modified catalysts ....132
3.3.1 ORR on 20 wt % Pd/C ....132
3.3.2 ORR on Pd modified Au catalysts ....133
4. Ethanol Oxidation Reaction....139
4.1 Ethanol oxidation on Pt based catalysts .... 140
4.1.1 20 wt % Pt/C ....140
4.1.2 Pt modified Au catalysts ....142
4.2 Ethanol oxidation on Pd based catalysts ....146
4.2.1 20 wt % Pd/C ....146
4.2.2 Pd modified Au catalysts.... 147
5. Conclusion....151
6. References....152

**Chapter Six Conclusion……159**
References……161

# DECLARATION OF AUTHORSHIP

I, **Prabalini Kannan** declare that the thesis entitled:

**Gold Based Electrocatalysts**

and the work presented in it are my own. I confirm that:

- This work was done wholly or mainly while in candidature for a research degree at this University;
- Where any part of this thesis has previously been submitted for a degree or any other qualification at this University or any other institution, this has been clearly stated;
- Where I have consulted the published work of others, this is always clearly attributed;
- Where I have quoted from the work of others, the source is always given. With the exception of such quotations, this thesis is entirely my own work;
- I have acknowledged all main sources of help;
- Where the thesis is based on work done by myself jointly with others, I have made clear exactly what was done by others and what I have contributed myself;

Signed: _____

Date: February 2011

# ACKNOWLEDGEMENTS

Firstly, I'm deeply indebted to my supervisor Prof. Andrea E. Russell whose help, stimulating suggestions and motivation helped me throughout the time of my research. Moreover, I would also like to thank my advisor Dr. Guy Denuault, whose valuable feedback and great attitude helped me with the completion of my PhD. My thanks must also go to Francesco and rest of the members from Prof. Richard Whitby's group who helped me to prepare the nanoparticles. Many thanks to Dr Meritxell Casadesus (University of Cardiff) for teaching me the UPD measurements, Medac Ltd for the elemental analysis of the catalysts, Johnson Matthey Technology Centre for TEM and XRD measurements and Brookhaven National Laboratory for EXAFS data collection. I would like to express my sincere gratitude to staff from glassblowers, the mechanical workshop and the stores who have provided me many pieces of equipment and the chemicals. A special mention should be made of the staff from the school of chemistry for creating a good working environment. I am also grateful to Mr Alastair Clarke who helped me in various ways. In addition, particular thanks and gratitude will go to Miss. Louis Purdy who carried out the experiments while I was pregnant.

I would like to express my humble gratitude to the members of the Russell group. Firstly, the former members Peter, Suzanne, Fabrice, Collin, David, Piotr, Katie, Dai and Li for their guidance and encouragement; particular thanks to Gael who helped me in various ways not only in academicals point of view but also in chatting, fighting etc. during the extended working hours. My thanks should also go to Anna for correcting my Chapters. Further thanks go to Stephen for the EXAFS analysis. I am very thankful for his help while I was writing from home. I am very much thankful to Jonathon who helped with the new format of thesis. My thanks are also due to the rest of the Russell group members Sarah, Beatrice, Laura, Rosie and Peter. Further thanks will go to other group members George who was very helpful during my stay in Southampton, Magda and Hartini. Finally, thanks to all my friends for making my time here enjoyable.

This thesis would never have been taken shape without the proper proof reading, a big thanks to Mr. John Forester for your proof reading.

I would also like to thank the Dorothy Hodgkin fund for supporting this project.

I wish to thank my husband, parents and brother. They raised me, supported me, taught me and loved me. Lastly and most importantly I would like to thank my baby daughter for having let me to do my work without any disturbance with her loving smile.

# Chapter One: Introduction

## 1. Catalysis

Catalysis is one of the most important phenomena in various aspects of chemistry. It is noteworthy to say that life cannot exist without catalysts because the human body is regulated by many biological reactions that involve catalytic enzymes. The term catalysis was first proposed by Berzelius[1] in 1836, and he defined the term catalysis. Most researchers believe that the catalyst is a substance which increases the rate of a reaction without permanently changing itself. Generally, however the catalyst is chemically involved. The basic principle of catalysis is demonstrated by the potential energy diagram shown in Figure 1-1. This diagram compares the catalytic pathway and the non-catalytic pathway.

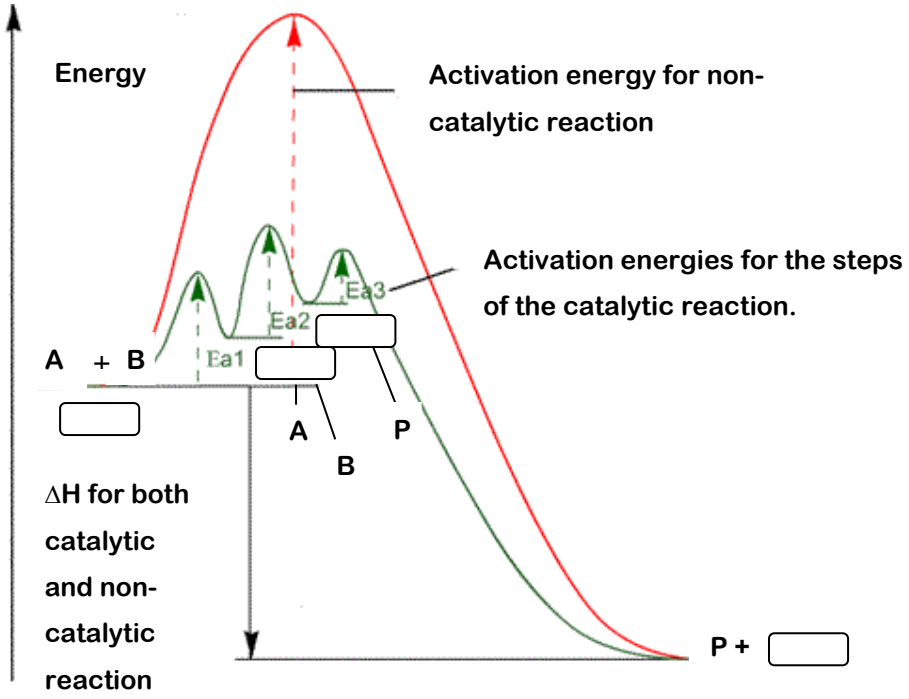


**Figure 1-1: Potential energy diagram of a catalytic reaction. Where ☐ indicates the catalysts.**

In the non-catalytic pathway, the reaction has to overcome a high energy barrier to form a product. However, in general, for heterogeneous catalysis a catalytic pathway involves three major steps. Initially, the reactants form a bond to the catalyst. Then the reaction takes place on the catalytic surface and forms the product. At the end, the product leaves the catalyst and regenerates the catalyst so that it can be used again for the next reaction. As the catalyst promotes the correct configuration for the reaction to occur, this barrier is lower than the barrier for the non-catalytic reaction.

# 2. Electrocatalysis

In electrochemistry, electrocatalysts play a vital role in various applications such as fuel cells, corrosion and batteries[2-10]. Electrocatalysts enhance the electrode kinetics by minimizing the overpotential of the reaction. Overpotential is defined as the additional potential in excess of the equilibrium potential for an electrode reaction to occur at a certain rate.

During the electrocatalytic process there will be a charge transfer between the metal and the species. When the metallic charge becomes negative the Fermi level gets raised, as a result there will be an electron transfer from the Fermi level of the metal to the LUMO (Lowest Unoccupied Molecular Orbital) of the species. In this case the species undergoes reduction. The reduction rate increases as the gap between the Fermi level and the LUMO increases. Similarly, when the metal becomes more positive the Fermi level gets lowered and the electron transfer from the HOMO (Highest Occupied Molecular Orbital) of the species to the metal occurs. In this case the species undergoes oxidation. Figure 1-2 shows the electron transformation between the metal and the species.

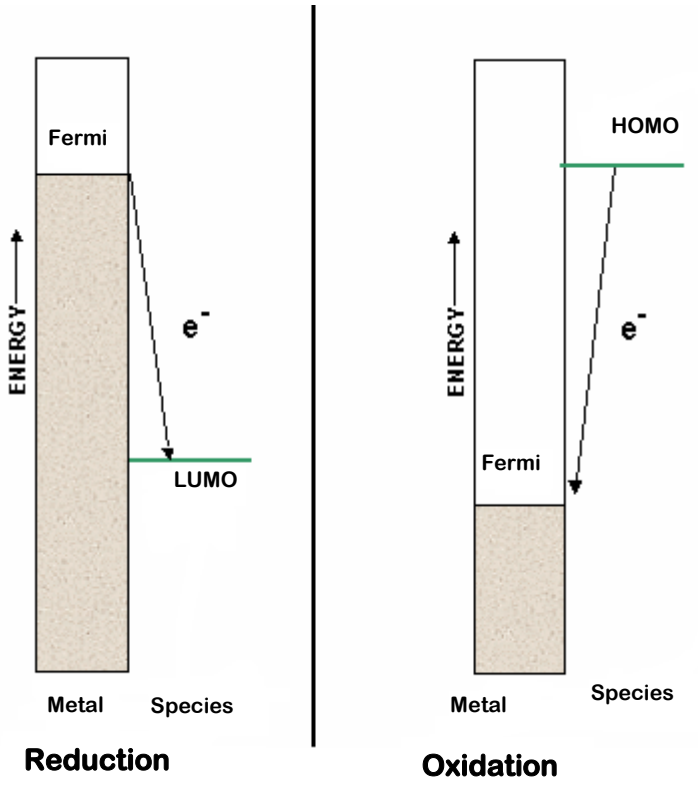


**Figure 1-2: Charge transfer energetic on a metal electrode**

In the catalytic reaction there will be a bond formation between the catalyst and the species. For example, in the case of hydrogen evolution in acidic solution the bond formation between the metal and the hydronium ion is the initial step.

$$H_3O^+ + M + e^- \rightarrow M - H_{ads} + H_2O \quad \textbf{[1-1]}$$

Here, the electron from the metal is transferred to the H-O bond which has attained suitable excited vibrational states, having energy equal to the Fermi energy of the metal.

Then the $H_2$ will be liberated either as electrochemical dissociation reaction,

$$H_3O^+ + M - H_{ads} + M + e^- \rightarrow 2M + H_2 + H_2O \quad \textbf{[1-2]}$$

or as chemical combination reaction.

$$M - H_{ads} + M - H_{ads} \rightarrow 2M + H_2 \quad \textbf{[1-3]}$$

Even though the chemical properties of the electrode material take an important role in governing the catalytic efficiency, the electronic and crystallographic feature, nature and the number of defects, size also form an important significant aspect in the process of electrocatalysis.

The electronic factor of the catalyst plays a decisive role in electrocatalytic activity. The activity of the catalyst commences with the formation of covalent bonds between the catalyst and the reactant molecules, which need to be strong enough for the reaction to occur. However, they should not be too strong as this will delay desorption of the products from the catalytic surface. The *d*-band character of the catalysts plays a major role in bonding. According to Pauling's valence bond theory of metals[11] excitation of electrons to a higher orbital is very important in the bonding mechanism. This promotion of electrons between the *d*, *s*, and *p* orbitals is referred to as *dsp* hybridization. The percentage of the *d*-band character is directly proportional to the extent of *dsp* hybridization. Metals with a higher number of unpaired electrons have lower percentage of *d*-band character and vice versa. For the catalytic bond formation, the catalyst acts as a donor or acceptor of electrons depending on the type of the reaction. The metal with higher *d*-band character (i.e. low unpaired electrons) favours the desorption reaction and the metal with lower *d*-band character (high unpaired electrons) favours the adsorption reaction[12].

The activity of a catalyst also depends on the size and the shape of the metal particles. The shape of the catalyst determines its surface atomic configuration. In other words the shape of the catalyst represents its crystal facets. Consequently the crystallographic facets are an essential parameter in the electrocatalytic activity. This difference in activity is mainly attributed to the variation in coordination geometry and the surface energy. This changes the interface between the exposed metal sites and the adsorbate[13].

Platinum is the most widely used electrocatalyst, on account of its favourable *d*-electron configuration and stability in a wide variety of media. Therefore, in the

general introduction presented here, Pt will be taken as an example, even though the work presented in this thesis is predominately on Au catalysts.

Generally it is accepted that the high index facets (with at least one of the *h, k, l* value equal to two or more) exhibit superior catalytic activity compared to the low index facets such as (100), (110), (111)[14]. These high index facets have low coordinated atoms that can readily react with the reactant molecule and lead to the bond breaking mechanism. It has been stated by Hoshi and collaborators[15] that the electro-oxidation of formic acid and the electro-reduction of carbon dioxide on Pt(210) exhibited high activity compared to the low index facets. The higher activities of high index crystals are mainly attributed to the many dangling bonds and the atomic steps; as a result the Pt can easily form reversible bond with the reactant molecules and there will not be any structural change during the reaction. However, the low index facets are generally smooth; as a result the reactant molecules can penetrate through the lattice plane and replace the Pt atoms. Due to this replacement, at the end of the reaction the ordered lattice will be destroyed and it will not be possible for them to continue to exist[16]. On the other hand, the preparations of high index facet nanoparticle catalysts are practically impossible. It has been known that the surface energies of different facets mainly increase in the order of $\gamma_{(111)} < \gamma_{(100)} \leq \gamma_{(110)} << \gamma_{(hkl)}$ ($h$ ,$k$ ,$l$ represents the high index facets)[17]. Therefore in the synthesis of nanoparticles high surface energies of high index facets grow much faster than the low index ones. However by thermodynamics the facets with high surface energies are unstable and as a result they are eliminated from the lattice. Due to the instability of the high index facets up to date various polyhedral shapes of nanoparticles bounded by low index facets have subsequently been prepared using shape controlled synthesis methods[18-22]. Figure 1-3 represents the basic shapes of Face Centred Cubic (FCC) metals enclosed by (100), (110) and (111) facets.

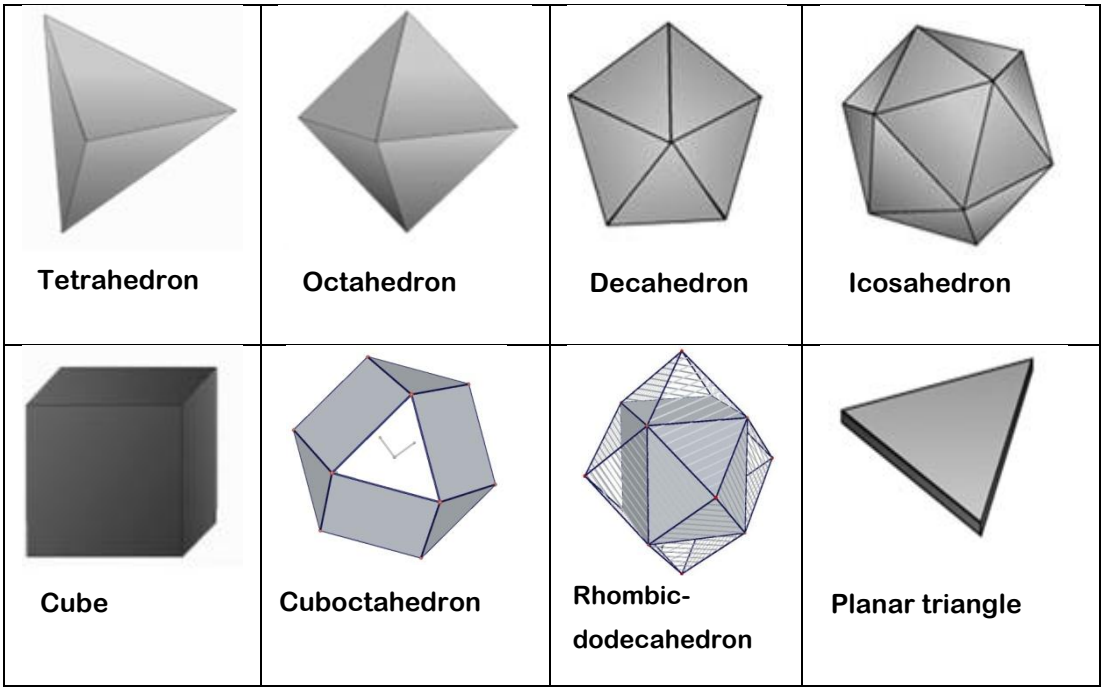


**Figure 1-3: Different shapes of FCC metals.**

Within the above FCC metals tetrahedron, octahedron, decahedron, planar triangle and icosahedron are formed by (111) facets, cube is by (100) facet, cuboctahedron is by (111) and (100) facets and rhombic dodecahedron is by (110) facet.

There are various electrocatalysts used as anode and cathode catalysts in fuel cell chemistry. The development of new electrocatalysts for the electrochemical reaction is an on-going challenge for surface electrochemists[23-28]. Pt based electrocatalysts have attracted great attention as electrocatalysts in various fuel cell reactions. The *d*-orbital vacancy of Pt makes it as an efficient catalyst. There have been various reports on the electrochemistry of Pt single crystals. Herrero *et al.*[29] reported on the methanol oxidation in acidic solutions using integrated voltammetric and chronoamperometric studies, showing that the methanol oxidation markedly depends on the surface geometry of Pt. They concluded that the activity of methanol oxidation is very high on Pt (110) facets and it is very low on Pt (111) facets. Similarly, the Pt (110) facets are very good for oxygen reduction reaction in acidic solutions as shown by Markovic *et al.*[30] on Pt single crystal surfaces using rotating ring disc experiments. According to their view, the activity of oxygen reduction increases in the order (111) < (100) < (110). They found out that the hydrogen

adsorption and the hydrogen peroxide reduction are nearly in the same potential region and the adsorption of hydrogen inhibits the hydrogen peroxide reduction. The adsorption of hydrogen is high in Pt (111) facets; as a result it blocks the adsorption sites for the hydrogen peroxide.

Another important factor that influences the activity of a catalyst is the size. It is commonly known that when the particle becomes smaller the active surface area increases; as a result more active sites are exposed for the catalytic reaction. Therefore in most of the cases small particles (< 10 nm) are more active compared to the larger ones. However, very small particles (< 2nm) are catalytically inactive, as they need high overpotential to drive the electrochemical reaction. In addition to that, the small size of the catalyst can penetrate through the support being therefore not available for the reaction. The electrochemical reactions are size specific reactions. In other words, in some kind of reactions the smaller particles favour the reaction while in other cases the larger ones favour. Therefore in general it is important to note that when making electrocatalysts the catalysts need to be a critical size for the particular type of reaction. Kinoshita[31] analysed the size effect for oxygen reduction on Pt catalysts. He considered a cuboctahedral particles of Pt that contains eight (111) octahedron crystals faces and six (100) cubic crystal faces. The plot of Mass Average Distribution (MAD) and the Surface Average Distribution (SAD) for different sizes of cuboctahedral Pt particles with (100) and (111) facets is given in Figure 1-4.

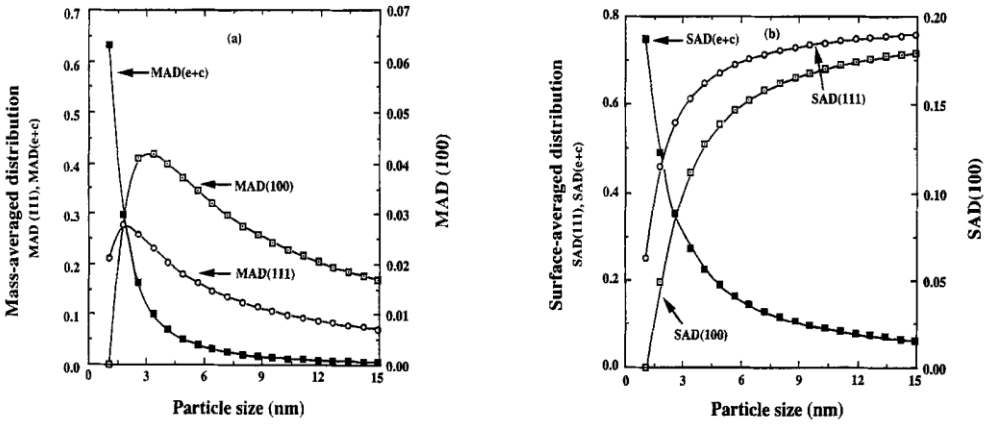


**Figure 1-4: MAD and SAD of atoms on the (111) and (100) crystal faces and on the edge and corner sites of cuboctahedral (a) MAD (b) SAD [32].**

According to the Figure 1-4 the maximum MAD for (100) and (111) facets are observed for the Pt particle sizes ~3.5 and ~2 nm respectively, and also the MAD at the edge and corners (e + g) sharply decreases with the size of Pt. The SAD for (100) facet and (111) facet increases with the particle size and the SAD (e + g) decreases with the size of Pt. Kinoshita also proved that the maximum mass activity (MA) of Pt can be obtained when the particle size is between 3 and 5 nm and also that the specific activity (SA) increases with the size of Pt. Decrease in SA value of smaller particles is also explained by Mukerjee *et al.*[33] with the aid of in situ X-ray absorption studies. They observed a stronger interaction of hydroxyl ion on smaller particles compared to larger ones and this interaction interfere the oxygen reduction. Size effect will be discussed in detail in Chapter four.

The support on which the catalyst particles are dispersed is another essential parameter in determining the electrocatalytic activity of the fuel cell system. Usually there will be a weak covalent bond between the support and the catalyst which will stabilize the catalyst throughout the reaction. It is generally recognized that the support has a very strong influence on the performance of a dispersed metal catalyst. The suitable support for the catalyst should be conductive and be stable throughout the reaction[34]. The most widely used support is carbon, although it can undergo corrosion during the reaction. Alternatively, various metal oxides such as $TiO_2$, $IrO_2$, $RuO_2$ have been used as supports in electrochemical technology[35-37].

Pd is also an important Pt group metal with high catalytic activity although not used in the past as widely as Pt electrocatalyst [38,39]. The major drawback of Pd is the dissolution at high anodic potentials, which is worst in acidic solutions. Also anion adsorption on Pd occurs at relatively lower potential compared to many electrochemical reactions. This blocks the Pd surface which results in a decrease in Pd activity. However much more recently, work has focused on Pd based chemistry. They are economically friendly compared to Pt and exhibit unique activity in the process of electrocatalysis. The Pd catalysts also show superior activity in formic acid oxidation, oxygen reduction, and ethanol oxidation reactions[40-44].

Apart from those catalysts, there is a great interest in developing gold based catalysts.

# 3. Gold Electrochemistry

Gold is a chemical element with the symbol Au and an atomic number 79. The atomic weight of Au is 196.96 a.m.u and the density at 20 °C is 19.32 g $cm^{-3}$. Gold melts at 1,063 °C and vaporises at 2,966 °C. It crystallizes in the FCC structure and the closest metallic inter nuclear distance is 288.4 pm. It is a soft and yellow metal with the highest ductility and the malleability of all the elements. Pure gold has a bright yellow colour and traditionally considered as inactive, not oxidizing in water or air. Gold is considered as one of the coinage metals and served as a symbol of wealth and a store of value throughout history. It has also been associated with a variety of symbolism and ideologies.

Chemically, gold, a transition element has the electronic configuration [Xe] $4f^{14}5d^{10}6s^{1}$ and it belongs to group 1B of the periodic table. It can form univalent and trivalent cations in solution. Compared to other metals pure gold has low chemical activity.

However, there are distinguished features between the properties of gold in the bulk form and those properties exhibited when they are present in the form of tiny nanoparticles. The unique properties of gold at the nanoscale lead to its use in various applications. Gold has generally been regarded as a poor catalyst until the dramatic results reported by Haruta *et al.*[45] much more recently. They proved that nanometre scale materials exhibit a superior electrocatalytic behaviour compared to their bulk counterparts. The small size of these particles makes them ideal catalysts for many chemical as well as electrochemical applications. Gold nanoparticles were found to have extraordinary electrocatalytic properties towards various electrochemical reactions that take place in fuel cells. Two major parameters control the chemical, physical and electrocatalytic properties of the nanoparticles, these are

the particle size and the shape (in other words the crystallographic orientations) of the prepared nanometre scale material[46].

Gold metal particles are normally dispersed on a support to maximize their specific surface area and minimize the overall cost of the metal. Lopez and collaborators[47] explained the unusual catalytic activity for CO oxidation of these nanoparticles using the density functional theory. Furthermore they claimed that the enhanced activities of these nanoparticles are mainly attributed to the different geometries present in smaller particles coupling with the presence of atoms with very low coordination number. Many electrochemical reactions are known to be structure sensitive; therefore the surface structure of the catalyst also may play a very important role in the performance of such a catalyst.

Pioneering recent research has suggested that the gold-based catalysts are potentially capable of being effectively employed in fuel cell processing. The most likely first use for gold catalysts in fuel cell systems is for the removal of carbon monoxide impurities from the hydrogen streams used for fuel cells. This excellent reason for developing the gold catalyst technologies described is not only based on their promising technological performance, but also the relatively low price and greater availability of gold compared to the more expensive platinum group metals, thereby potentially reducing significantly capital cost of fuel cell applications[48].

Nanosized gold catalysts play a significant role in various catalytic reactions taking place in fuel cells. In alkaline electrolytes gold is an efficient oxygen reduction catalyst (being used in Space Shuttle Orbiter fuel cells)[49], and is also capable of catalysing the direct oxidation of sodium borohydride[50] with high utilisation. CO poisoning is one of the major problem in the fuel cell chemistry. However gold catalyst is able to oxidize the solution phase CO from hydrogen feedstock or in the fuel cell membrane[51].

Based on the current research efforts being devoted to gold there is some confidence that many new practical applications for gold based catalysts could emerge over the next decade.

# 4. Bimetallic catalysts

Currently bimetallic catalysts have gained much attention due to their unique structural arrangements[52,53]. The outstanding potential of these bimetallic catalysts such as alloys and core-shell catalysts lies in the ability to achieve structures with combination of properties that neither individual material possesses alone.

## 4.1 Alloys

In electrochemistry, research on bimetallic/trimetallic alloys is very popular particularly in low temperature fuel cells[54]. Anodically they are used mainly in hydrogen oxidation and methanol oxidation reactions; cathodically they are very good oxygen reduction catalysts. Recent studies proved that Pt alloys exhibit higher electrocatalytic activity than Pt alone[55-57]. This superior electrocatalytic activity can be explained in terms of bifunctional mechanism occurring at the alloy surface and the electronic effect i.e. one metal alters the electronic property of the other metal and creates more active catalytic surface[58]. Marc and Koper[58] stated that on Pt-Ru and Pt-Sn alloys the electrochemical oxidation of CO is mostly dominated by bifunctional mechanism. They believed that Ru and Sn provide the oxygen donor for the active removal of CO.

Initially, adsorption of water occurs on the activated Ru or Sn surface.

$$H_2O + *_{Ru\ or\ Sn} \rightarrow OH_{Ru\ or\ Sn} + H^+ + e^- \quad \textbf{[1-4]}$$

Then CO adsorbed on Pt reacts with Ru or Sn adsorbed OH to produce $CO_2$.

$$CO_{Pt} + OH_{Ru\ or\ Sn} \rightarrow CO_2 + H^+ + e^- + *_{Pt} + *_{Ru\ or\ Sn} \quad \textbf{[1-5]}$$

In addition, an electronic effect also plays a role in the electrochemical oxidation of CO. The combination of Pt and Ru leads to a weaker bond of Pt-CO and stronger bond of Ru-CO. The change in binding energy being explained by the *d*-band shift model as reported by Hammer and Norskov[59]. According to their view, there will be a transfer of *d* electrons from the Pt to Ru, Thereby to maintain the *d*-band filling, Pt *d*-band shifts down. As a result the Pt–CO bond get weakens. And on the other hand *d*-band of the Ru shifted upwards leads to a stronger adsorption sites at the Ru sites.

## 4.2 Core-shell catalysts

Currently core-shell catalysts are also very popular among the researchers[60-63]. Much recent effort being dedicated in developing core–shell electrocatalysts with higher activity. As the name suggests, core–shell catalysts consist of a core of one substance and a coating shell of another substance. The composition of the core and the shell can be varied to give a wide range of different properties. Most of the core–shell catalysts studied in electrochemistry have a Pt shell to minimize the Pt loading. The core–shell catalysts are expected to show increase in activity compared to the conventional Pt only electrocatalysts in a range of electrochemical reactions. These enhanced properties are attracted to both geometric and electronic effects induced between the core and the shell[61].

The core–shell catalysts can be prepared in a number of ways and Under Potential Deposition (UPD) plays a significant role in preparation of metal monolayers. UPD is defined as a process of the deposition of a metal on to a substrate at potentials positive to the Nernst potential for the subsequent bulk metal deposition[63]. The mechanism of metal (P) deposition on a substrate (S) is given as follows.

Initially there will be a formation of UPD ad-layer of metal M on to a substrate. For this to occur, the adsorbate–substrate interactions should be stronger than the adsorbate–adsorbate interactions. Secondly the metal ad-layer M is replaced by a more noble metal P by means of electroless deposition and the metal ad-layer M is oxidatively dissolved. This replacement is an irreversible spontaneous reaction. For

this is to take place the substrate S should be more noble than the metal undergoing deposition to prevent the substrate undergoing oxidation. The redox replacement reaction will be given as follows.

$$M^0_{UPD} + (m/z)P^{z+} \rightarrow M^{m+} + (m/z)P^0 \quad \textbf{[1-6]}$$

Where *z* indicates the valence of P.

For the above reaction to become more thermodynamically favourable,

$$\Delta E_{P^{z+}/P} - \Delta E^0_{M^{m+}/M} > 0 \quad \textbf{[1-7]}$$

Where $\Delta E_{P^{z+}/P}$ is the equilibrium potential of P and $\Delta E^0_{M^{m+}/M}$ is the equilibrium potential of UPD ad-layer.

Adzic and coworkers[64] were the first to prove that metal UPD can be used in redox replacement technique to deposit precious metals as electrocatalysts. They invented a new approach in designing low Pt content electrocatalysts for oxygen reduction reaction. This approach involves depositing a Pt sub-monolayer or monolayer on Au (111), Ir(111), Pd(111), Rh(111) and Ru(0001) single crystals, and Pd nanoparticles. They prepared these catalysts using the redox replacement of a Cu monolayer. The deposition of Cu monolayer on Au catalyst and the replacement of Cu by Pt using redox replacement technique are shown in Figure 1-5.

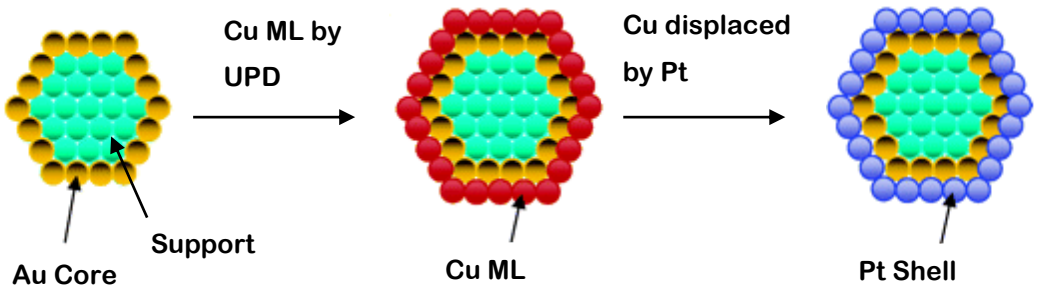


**Figure 1-5: Model for the synthesis of Pt monolayer catalysts on non noble metal–noble metal core–shell nanoparticles[65].**

This method not only reduces the amount of Pt but also gives better dispersion of the catalyst. The Pt shell can be able to protect the Au core from acid leaching.

Furthermore, the shell improves the electrocatalytic activity of the catalyst by affecting its electronic properties or by introducing a strain. Oxygen reduction on such monolayer catalysts exhibited an extraordinary catalytic activity compared with the Pt alone. This enhanced activity was recently demonstrated by Norskov and coworkers[61] and they concluded that the surface metal *d*–band character plays an important role in determining the surface activity. A *d*-band model connects the changes in energy centre of the valence *d*-band density of states at the surface sites with their capability of forming chemisorption bonds. According to this model, when an antibonding state shifts up through the Fermi level there will be a formation of stronger bond and, when it shifts down a weaker bond forms. They also stated that when a monolayer is deposited on a substrate, there will be a compressive or tensile strain through a substrate lattice parameter. In other words there will be an electronic interaction between the Pt monolayer and its substrate. This can cause a variation in the *d*-band widths and as a result shifting of *d*-band centre either up or down depends on the metal substrate interaction[66]. According to DFT theories a compressive strain leads to a downshift and tensile strain leads to up shift of *d*-band state[64].

Recently, Noel Kristian and collaborators[62] prepared the Pt shell-Au core/C electrocatalyst with a controlled shell thickness using a successive chemical reduction approach. They synthesised different molar ratios of Pt/Au catalysts and observed a decrease in specific activity of Pt with increasing Pt/Au ratio for methanol oxidation reaction, improved durability also being observed for these catalysts. More on core–shell catalysts will be discussed later in Chapter five.

# 5. Aims and Objectives

The review presented so far demonstrates the potential use of electrocatalysts in fuel cell systems and the current challenges hindering its development to commercialization. The work herein involves preparation of carbon supported gold catalysts and their characterization using a variety of techniques. The gold nanoparticles were prepared using thiol as an encapsulating agent. Those gold particles were loaded on to a carbon support and appropriate heat treatment

techniques were applied. The variety of techniques used to characterize the catalysts will include Cyclic Voltammetry (CV), Transmission Electron Microscopy (TEM), X- Ray Diffraction techniques (XRD) and X-ray Absorption Spectroscopy (XAS). The catalysts were studied for oxygen reduction, carbon monoxide oxidation and ethanol oxidation reactions. The particle size on the above reactions will be discussed.

As discussed earlier, Pt is considered as an effective electrocatalyst for various fuel cell reactions. However due to the limited supply and the high cost of Pt, the core–shell catalysts are of interest to reduce the usage of Pt. These were prepared using Pt or Pd as the shell. The Cu underpotential method was used to prepare the Pt or Pd monolayer or sub monolayer of gold catalysts. These Pt or Pd modified gold catalysts being characterized by CV measurements. Different electrochemical reactions including oxygen reduction and ethanol oxidation reactions were performed. The effect of the monolayer of Pt or Pd on these electrochemical reactions will be analysed. In all cases an alkaline medium was chosen as electrolyte. In alkaline solutions most of the materials are expected to be stable and show more favourable reactions due to the weakening of the adsorption energy[67].

In summary, the different kind of catalysts, their reaction mechanism and their applications in the fuel cell system are outlined in the introduction. Chapter two explains all the experimental methods used throughout this work. This includes the synthesis of Au catalysts and their basic characterization techniques. The general characterizations of the catalysts will be discussed in Chapter three. The size effect will be discussed in Chapter four, wherein, the size effect on oxygen reduction, ethanol oxidation and the carbon monoxide oxidation reactions are reviewed. Effect of surface modification will be investigated in Chapter five, focusing on the Pt or Pd monolayer on Au catalysts. This includes making the modified catalyst and their characterization, and the effect of these metal ad-layers on oxygen reduction and ethanol oxidation reactions. Finally Chapter six presents the conclusion from all the work carried out during the PhD program.

For clarity, it should be mentioned that all the work presented in this thesis is my work, except where specifically stated. In particular assistance was obtained in the following measurements.

- The elemental analysis was conducted at Medac Ltd by one of their technicians.
- The TEM and the XRD analysis of the prepared catalysts were carried out at Johnson Matthey Technology Centre by one of their technicians.
- XAS measurements were carried out at National Synchrotron Light Source (NSLS) at Brookhaven National Laboratories, USA. The analysis was carried out by one of my colleagues Mr. S.W. T Price.
- Preparation of the Pd modified catalysts and their characterizations were done by Miss Louis Alexandra Purdy under my close supervision. I.e. she took my place in the laboratory during my pregnancy, but I directed all the measurements and interpreted all the data.

# 6. References


(1) Berzelius, J. J. *Edin.New Phil.Jrnl* **1836**, *21*, 223.

(2) Mann, J.; Yao, N.; Bocarsly, A. B. *Langmuir* **2006**, *22*, 10432.

(3) Jusys, Z.; Kaiser, J.; Behm, R. J. *Langmuir* **2003**, *19*, 6759.

(4) Wagner, F. T.; Lakshmanan, B.; Mathias, M. F. *The Journal of Physical Chemistry Letters* **2010**, *1*, 2204.

(5) Girishkumar, G.; McCloskey, B.; Luntz, A. C.; Swanson, S.; Wilcke, W. *The Journal of Physical Chemistry Letters* **2010**, *1*, 2193.

(6) Medeiros, M. G.; Zoski, C. G. *The Journal of Physical Chemistry B* **1998**, *102*, 9908.

(7) Heck, R. M.; Farrauto, R. J. *Applied Catalysis A: General* **2001**, *221*, 443.

(8) Funabiki, M.; Yamada, T.; Kayano, K. *Catalysis Today* **1991**, *10*, 33.

(9) Hosokawa, M.; Nogi, K.; Naito, M.; Yokoyama, T. In *Nanoparticle Technology Handbook*; Masuo, H., Kiyoshi, N., Mario, N., Toyokaz, U. Y., Eds.; Elsevier: Amsterdam, 2008, p 550.

(10) Shao, Y.; Wang, J.; Kou, R.; Engelhard, M.; Liu, J.; Wang, Y.; Lin, Y. *Electrochimica Acta* **2009**, *54*, 3109.

(11) Pauling, L. *Proc. Nat. Acad. Sci. USA* **1975**, *72*, 3.

(12) Srinivasan, S. *Fuel cells: from fundamentals to applications* Springer, 2006.

(13) Koenigsmann, C.; Zhou, W.-p.; Adzic, R. R.; Sutter, E.; Wong, S. S. *Nano Letters* **2010**, *10*, 2806.

(14) Tian, N.; Zhou, Z.-Y.; Sun, S.-G. *The Journal of Physical Chemistry C* **2008**, *112*, 19801.

(15) Hoshi, N.; Kawatani, S.; Kudo, M.; Hori*, Y. *Journal of Electroanalytical Chemistry* **1999**, *467*, 67.

(16) Xiong, Y.; Wiley, B.; Xia, Y. *Angewandte Chemie International Edition* **2007**, *46*, 7157.

(17) Wen, Y.-N.; Zhang, J.-M. *Solid State Communications* **2007**, *144*, 163.

(18) Chen, J.; Lim, B.; Lee, E. P.; Xia, Y. *Nano Today* **2009**, *4*, 81.

(19) Xia, B. Y.; Wang, J. N.; Wang, X. X. *The Journal of Physical Chemistry C* **2009**, *113*, 18115.

(20) Niu, W.; Zhang, L.; Xu, G. *ACS Nano* **2010**, *4*, 1987.

(21) Watt, J.; Cheong, S.; Toney, M. F.; Ingham, B.; Cookson, J.; Bishop, P. T.; Tilley, R. D. *ACS Nano* **2009**, *4*, 396.

(22) Wang, D.; Huang, J.; Liu, Y.; Han, X.; You, T. *Journal of Nanoparticle Research* **2010**, 1.

(23) Seto, K.; Iannelli, A.; Love, B.; Lipkowski, J. *Journal of Electroanalytical Chemistry* **1987**, *226*, 351.

(24) Kita, H.; Ye, S.; Gao, Y. *Journal of Electroanalytical Chemistry* **1992**, *334*, 351.

(25) Barber, J.; Morin, S.; Conway, B. E. *Journal of Electroanalytical Chemistry* **1998**, *446*, 125.

(26) Markovic, N. M.; Adzic, R. R.; Cahan, B. D.; Yeager, E. B. *Journal of Electroanalytical Chemistry* **1994**, *377*, 249.

(27) Markovic, N.; Gasteiger, H.; Ross, P. N. *Journal of The Electrochemical Society* **1997**, *144*, 1591.

(28) El Kadiri, F.; Faure, R.; Durand, R. *Journal of Electroanalytical Chemistry* **1991**, *301*, 177.

(29) Herrero, E.; Franaszczuk, K.; Wieckowski, A. *The Journal of Physical Chemistry* **1994**, *98*, 5074.

(30) Markovic, N. M.; Gasteiger, H. A.; Ross, P. N. *The Journal of Physical Chemistry* **1995**, *99*, 3411.

(31) Kinoshita, K. *Journal of The Electrochemical Society* **1990**, *137*, 845.

(32) Kinoshita, K. *Journal of the Electrochemical Society* **1990**, *137*, 845.

(33) McBreen, J.; Mukerjee, S. *Journal of The Electrochemical Society* **1995**, *142*, 3399.

(34) Guerin, S.; Hayden, B. E.; Pletcher, D.; Rendall, M. E.; Suchsland, J.-P.; Williams, L. J. *Journal of Combinatorial Chemistry* **2006**, *8*, 791.

(35) Song, H.; Qiu, X.; Li, X.; Li, F.; Zhu, W.; Chen, L. *Journal of Power Sources* **2007**, *170*, 50.

(36) Durso, C.; Lizbeth, M.; Di Blasi, A.; Baglio, E.; Ornelas, R.; Orozco, G.; Arriaga, L. G.; Antonucci, V.; Arico, A. *ECS Transactions* **2007**, *11*, 191.

(37) Yu, H.; Zeng, K.; Fu, X.; Zhang, Y.; Peng, F.; Wang, H.; Yang, J. *The Journal of Physical Chemistry C* **2008**, *112*, 11875.

(38) Luna, S. F.; Varela, F. J. R.; Dabek, R.; Savadogo, O. *ECS Transactions* **2008**, *16*, 761.

(39) Xu, C.; Tian, Z.; Shen, P.; Jiang, S. P. *Electrochimica Acta* **2008**, *53*, 2610.

(40) Salvador-Pascual, J. J.; Citalán-Cigarroa, S.; Solorza-Feria, O. *Journal of Power Sources* **2007**, *172*, 229.

(41) Savadogo, O.; Lee, K.; Oishi, K.; Mitsushima, S.; Kamiya, N.; Ota, K. I. *Electrochemistry Communications* **2004**, *6*, 105.

(42) Shen, P. K.; Xu, C. *Electrochemistry Communications* **2006**, *8*, 184.

(43) Wang, Y.; Wu, B.; Gao, Y.; Tang, Y.; Lu, T.; Xing, W.; Liu, C. *Journal of Power Sources* **2009**, *192*, 372.

(44) Cui, G.; Song, S.; Shen, P. K.; Kowal, A.; Bianchini, C. *The Journal of Physical Chemistry C* **2009**, *113*, 15639.

(45) Haruta, M.; Date, M. *Applied Catalysis A: General* **2001**, *222*, 427.

(46) Jaramillo, T. F.; Baeck, S.-H.; Cuenya, B. R.; McFarland, E. W. *Journal of the American Chemical Society* **2003**, *125*, 7148.

(47) Lopez, N.; Nørskov, J. K. *Journal of the American Chemical Society* **2002**, *124*, 11262.

(48) Cameron, D.; Holliday, R.; Thompson, D. *Journal of Power Sources* **2003**, *118*, 298.

(49) Corti, C. W.; Holliday, R. J.; Thompson, D. T. *Applied Catalysis A: General* **2005**, *291*, 253.

(50) Chatenet, M.; Micoud, F.; Roche, I.; Chainet, E. *Electrochimica Acta* **2006**, *51*, 5459.

(51) S.Cameron, D. *Gold bulletin* **2003**, *36*, 17.

(52) Maroun, F.; Ozanam, F.; Magnussen, O. M.; Behm, R. J. *Science* **2001**, *293*, 1811.

(53) Soriaga, M. P. *Chemical Reviews* **1990**, *90*, 771.

(54) Markovic, N. M.; Ross, P. N. *Surface Science Reports* **2002**, *45*, 117.

(55) Schmidt, T. J.; Noeske, M.; Gasteiger, H. A.; Behm, R. J.; Britz, P.; Brijoux, W.; Bönnemann, H. *Langmuir* **1997**, *13*, 2591.

(56) Bardi, U.; Atrei, A.; Ross, P. N.; Zanazzi, E.; Rovida, G. *Surface Science* **1989**, *211-212*, 441.

(57) Bardi, U.; Beard, B. C.; Ross, P. N. *Journal of Catalysis* **1990**, *124*, 22.

(58) Koper, M. T. M. *Surface Science* **2004**, *548*, 1.

(59) Hammer, B.; Nørskov, J. K. In *Advances in Catalysis*; Bruce C. Gates, H. K., Ed.; Academic Press: 2000; Vol. Volume 45, p 71.

(60) Luo, J.; Wang, L.; Mott, D.; Njoki, P. N.; Lin, Y.; He, T.; Xu, Z.; Wanjana, B. N.; Lim, I. I. S.; Zhong, C. J. *Advanced Materials* **2008**, *20*, 4342.

(61) Kitchin, J. R.; Norskov, J. K.; Barteau, M. A.; Chen, J. G. *J. Chem. Phys.* **2004**, *120*, 10240.

(62) Kristian, N.; Wang, X. *Electrochemistry Communications* **2008**, *10*, 12.

(63) Adzic, R. R. *Bull.Soc.Chim.Beograd* **1983**, *48*, 1.

(64) J. Zhang, M. B. V., K. Sasaki,F. Uribe and R. R. Adzic *J. Serb. Chem. Soc.* **2005**, *70*, 513.

(65) Zhang, J.; Lima, F. H. B.; Shao, M. H.; Sasaki, K.; Wang, J. X.; Hanson, J.; Adzic, R. R. *The Journal of Physical Chemistry B* **2005**, *109*, 22701.

(66) Lima, F. H. B.; Zhang, J.; Shao, M. H.; Sasaki, K.; Vukmirovic, M. B.; Ticianelli, E. A.; Adzic, R. R. *The Journal of Physical Chemistry C* **2006**, *111*, 404.

(67) Jiang, L.; Hsu, A.; Chu, D.; Chen, R. *Journal of Electroanalytical Chemistry* **2009**, *629*, 87.

# Chapter Two: Experimental Methods and Techniques

This Chapter describes the experimental methods that were used throughout this work. This includes the catalyst preparation and characterization techniques, with particular emphasis on testing activity for fuel cell reactions.

## 1. Reagents and Materials

The reagents and materials used in this work are listed with their respective suppliers.

**Table 2-1 : List of the reagents/materials used and their suppliers.**

| Reagents and Materials | Suppliers |
|---|---|
| XC-72R carbon black | Cabot Corporation |
| Hydrogen tetrachloroaurate (purity 95 %) | Alfa Aeser |
| Tetraoctylammonium bromide (purity 98 %) | Fisher |
| Toluene (reagent grade) | Fisher |
| Dodecanethiol (purity 98 %) | Sigma Aldrich |
| Sodium borohydride (general purpose grade) | Sigma Aldrich |
| Ethanol (HPLC grade) | Rathburn chemicals |
| Hexane (purity 95 %) | Fisher |
| Micropolish | Buehler |
| Concentrated sulphuric acid (purity 98%) | Fisher |
| Nafion® solution 5 wt % in alcohol | Sigma Aldrich |
| Potassium hydroxide (analytical grade) | Fisher |
| Isopropyl alcohol (reagent grade) | Fisher |
| Lead nitrate (purity 99.99 %) | Sigma Aldrich |

| | |
|---|---|
| Copper sulphate pentahydrate (purity 99 %) | Sigma Aldrich |
| Copper Chloride (analytical grade) | Sigma Aldrich |
| Copper perchlorate (purity 98 %) | Sigma Aldrich |
| Sodium sulphate (purity 99.5 %) | Sigma Aldrich |
| Sodium chloride (ultrapure) | Sigma Aldrich |
| Sodium perchlorate (purity 99 %) | Sigma Aldrich |
| Potassium tetrachloroplatinate (purity 98 % ) | Sigma Aldrich |
| Potassium tetrachloropalladate (purity 98 % ) | Sigma Aldrich |
| 20 wt % Pt supported on carbon | Johnson Matthey Technology Centre |
| 20 wt % Pd supported on carbon | Johnson Matthey Technology Centre |

# 2. Preparation of gold electrocatalysts

The gold electrocatalysts were prepared using the 'Brust' method[1] (i.e thiol encapsulated) and were then loaded on to an activated carbon to prepare the carbon supported gold electrocatalysts. After that, appropriate heat treatment processes were carried out to obtain highly active catalysts containing different particle sizes.

## 2.1 Synthesis of nanoparticles

An aqueous solution of $HAuCl_4.3H_2O$ (60 ml, 30 mmol $dm^{-3}$) was mixed with a solution of tetraoctylammonium bromide (TOAB) in toluene (160 ml, 50 mmol $dm^{-3}$). The two-phase mixture was vigorously stirred and transferred to a separating funnel until all the tetrachloroaurate was transferred into the organic layer (The yellow aqueous solution quickly cleared and the toluene phase became orange-brown as the $AuCl_4^-$ was transferred in to it). Then dodecanethiol (0.2 ml) was added to the organic phase. A freshly prepared aqueous solution of $NaBH_4$ (50 ml, 0.4 mol $dm^{-3}$) was slowly added with vigorous stirring. After further stirring for 3 h, the organic phase was separated, evaporated to 10 ml in a rotary evaporator, and mixed

with 800 ml ethanol to remove excess thiol. The mixture was kept overnight at –18 °C and the dark brown precipitate was filtered off and washed with ethanol. The crude product was dissolved in 20 ml toluene and again precipitated with 800 ml ethanol. The precipitate was filtered off, washed with hexane and then evaporated in a vacuum evaporator. The dry product was brown in colour and had a waxy texture.

## 2.2 Loading on carbon

The nanoparticles were supported on carbon black (Vulcan XC – 72 R). This support was chosen because of its large mesoporous area and graphitic character giving good electronic conductivity[2]. The gold colloid dispersion in hexane was combined with a suspension of Vulcan carbon XC – 72 R in hexane to prepare ~20 wt % Au/C catalysts. After sonication for 30 min, the mixed solution was stirred for 48 h. The powders were separated by suction filtration and then washed thoroughly with hexane.

## 2.3 Heat treatment process

The carbon supported catalysts were heat treated to different temperatures to obtain different gold particle sizes.

**Table 2-2: Catalysts and their heat treatment conditions.**

| Catalyst | Gas purge of furnace | Ramp rate / °C | Final Temperature / °C |
|---|---|---|---|
| $Au_{3.2}$ | air | 2 | 300 |
| $Au_{5.4}$ | $O_2$ & 5 % $H_2$ / $N_2$ | 2 | 350 |
| $Au_{6.0,\ wide}$ | air | 2 | 400 |
| $Au_{6.0,\ narrow}$ | $N_2$ | 2 | 500 |

The temperature was then maintained for 6 hrs before air cooling. Slow heating ramp rate was used to prevent particle sintering[3].

# 3. Characterization of prepared catalysts

The prepared catalysts were characterized using TEM, XRD, XAS, UPD, oxygen reduction reaction, ethanol oxidation reaction and carbon monoxide oxidation reaction. The oxygen reduction reaction, ethanol oxidation reaction and carbon monoxide oxidation reaction will all be explained in detail later.

## 3.1 Transmission Electron Microscopy(TEM)

TEM is a powerful technique that is used to study the size, shape and arrangement of the nanoparticles supported on carbon. In this process a beam of electron will be passed through the thin film of sample then that electron will interact with the sample as a result an image is produced from the transmitted electrons. The first TEM was invented by Max Koll and Ernst Ruska[4] in 1931.

### 3.1.1 TEM measurements by JM

The samples were sent to the Johnson Matthey Technology Centre (JMTC) for TEM analysis and the images were collected by one of their technicians as described below.

The powder was crushed between glass slides and dusted onto a holey carbon film supported by a copper grid. The samples were examined in the Tecnai F20 TEM using the following instrumental conditions at 200 kV with Bright Field (BF) and High Angle Annular Dark Field (HAADF) methods. Particle Size Analysis (PSA) was performed on BF images. The mean and standard deviation of the particle size distribution were calculated from the log-normal distribution and are number-weighted.

A representative TEM image of one of the catalysts and its PSA are given in Figure 2-1 (A) & (B) respectively.

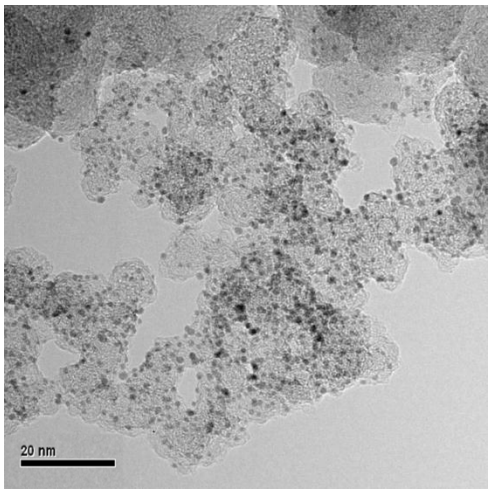


(A)

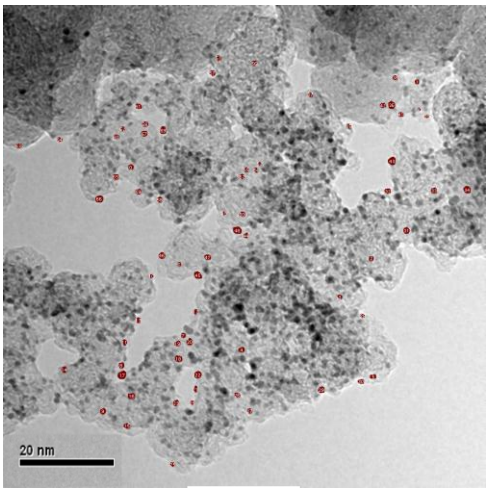


(B)

**Figure 2-1: TEM of prepared catalyst (A) and its PSA (B) at scale bar 20 nm.**

The Au particles are well dispersed on the carbon support. In some areas highly concentrated particles are observed where as in most of the areas the particles are evenly distributed. The particles are mostly spherical in shape.

The particle size analysis was performed on the BF image and its distribution is given in Figure 2-4.

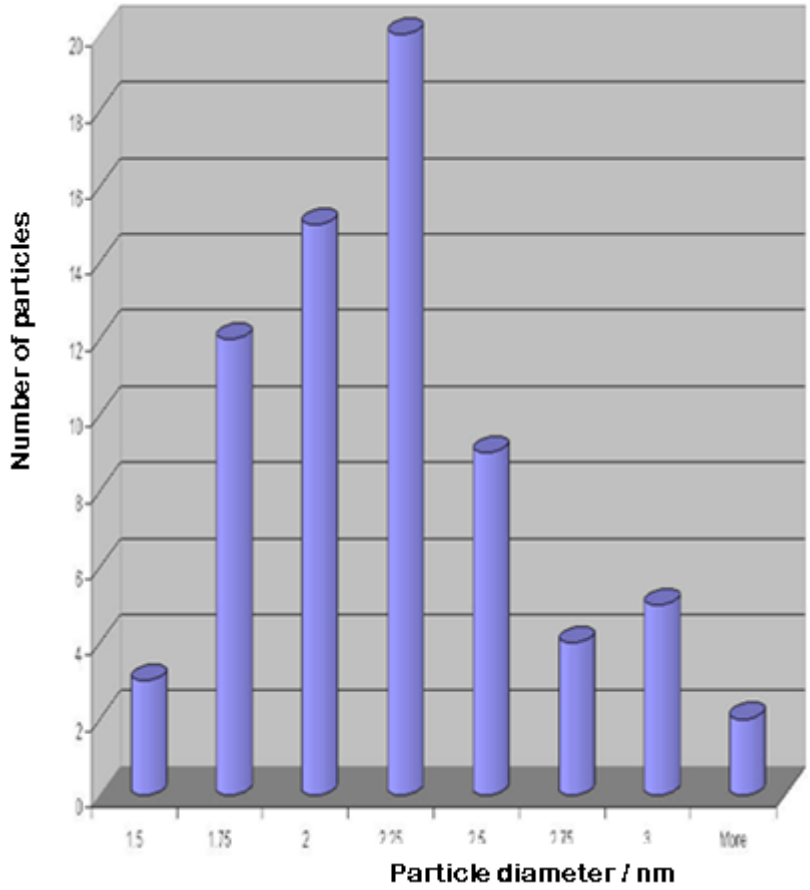


**Figure 2-2: Particle size distribution from TEM analysis (frequency y-axis, diameter x-axis)**

From the above Figure it can be clearly seen that the distribution of particle diameters is approximately Gaussian distribution and the majority of the particles centred on 2.25 nm.

## 3.2 X-ray Diffraction Analysis (XRD)

XRD is a powerful non-destructive and rapid analytical technique primarily used for phase identification of crystalline materials. It is used to determine the unit cell dimension and the crystallite size and provides measurement of sample purity. However it requires ~ 0.1 g of the catalyst, which must be ground into a powder.

When a crystal is bombarded with X-rays of a fixed wavelength (similar to spacing of the atomic-scale crystal lattice planes) and at certain incident angles, intense reflected X-rays are produced when the wavelengths of the scattered X-rays interfere constructively. In order for the waves to interfere constructively, the differences in the travel path must be equal to integer multiples of the wavelength. A diffracted beam of X-rays will leave the crystal at an angle equal to that of the incident beam when this constructive interference occurs[5].

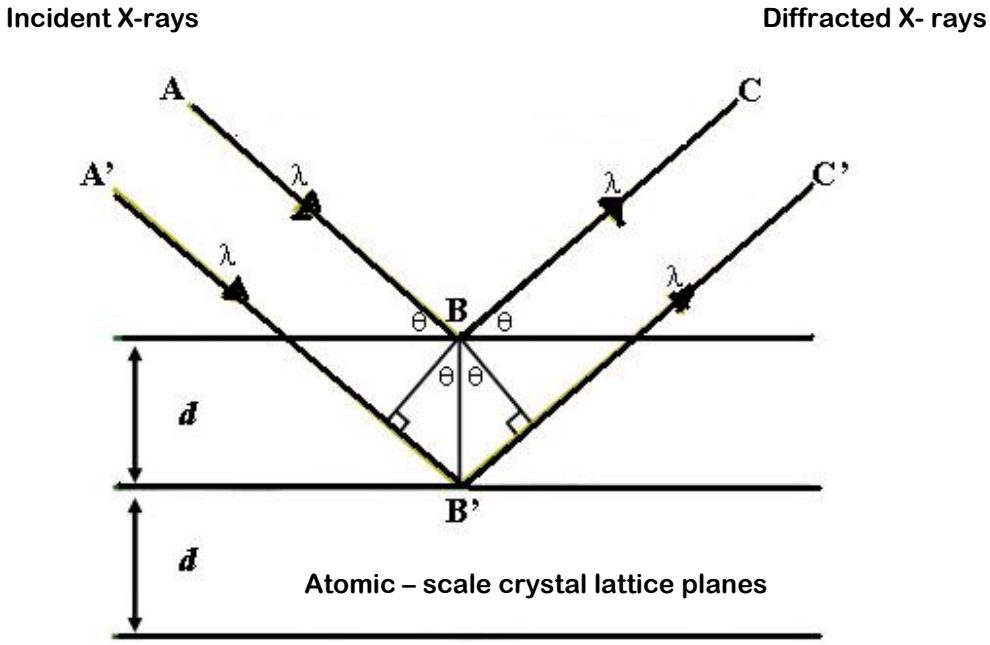


**Figure 2-3: Bragg's Law reflection. The diffracted x-rays exhibit constructive interference when the distance between paths ABC and A'B'C' differs by an integer number of wavelengths (λ).**

To illustrate this feature, consider a crystal with lattice planar distances d as shown in Figure 2-3. In instances where the path length difference between the X-ray paths ABC and A'B'C' is an integer multiple of the wavelength, constructive interference will occur for a combination of that specific wavelength, crystal lattice planar spacing and angle of incidence (θ). Each rational plane of atoms in a crystal will undergo refraction at a single, unique angle (for X-rays of a fixed wavelength).

The general relationship between the wavelength of the incident X-rays, angle of incidence and spacing between the crystal lattice planes of atoms is known as Bragg's Law,

$$n\lambda = 2d \sin\theta_{hkl} \quad \textbf{[2-1]}$$

Where n (an integer) is the "order" of reflection, λ is the wavelength of the incident X-rays, *d* is the interplanar spacing of the crystal and $\theta_{hkl}$ is the angle of incidence. By assuming that the Au catalysts are FCC, the interplanar spacing $d_{hkl}$ is given as,

$$d_{hkl} = \frac{a}{\sqrt{h^2 + k^2 + l^2}} \quad \textbf{[2-2]}$$

Where $a$ is the lattice parameter and *h,k,l* are the Millar indices of the Bragg plane.

Once the FCC peak position $\theta_{hkl}$ is identified, the lattice parameter $a$ can be calculated using Equation 2-3,

$$\sin^2\theta_{hkl} = \frac{\lambda^2}{4a^2}(h^2 + k^2 + l^2) \quad \textbf{[2-3]}$$

XRD can be used to determine crystallite size of the gold particles in the sample. The diffraction lines are broader when the particle size decreases. This broadening will be used to calculate the particle size by measuring the Full Width at Half Maximum (FWHM) values after a background subtraction. The average particle size, L, can then be calculated using the Scherrer Equation[6],

$$L = \frac{0.9\,\lambda}{B_{2\theta}\cos\theta_{\max}} \quad \textbf{[2-4]}$$

Where $\lambda$ is the wavelength and $B_{2\theta}$ is the measured broadening in radians.

## 3.2.1 XRD measurement by JM

The samples were sent to the Johnson Matthey Technology Centre for XRD analysis and all the data was collected by one of their technicians as briefly discussed below.

XRD measurements were performed on a Bruker AXS D8 advance diffractometer in parallel beam mode with a position sample holder, using Cu Kα1 radiation ($\lambda$ = 0.154 nm) with a Ni filter working at 40 kV and 40 mA. The diffracted beam was detected with a Vantec position sensitive detector, in a step scanning mode (10 s/step), for 2θ range of 1°- 140°.

Figure 2-4 shows a representative XRD pattern of one of the prepared catalysts.

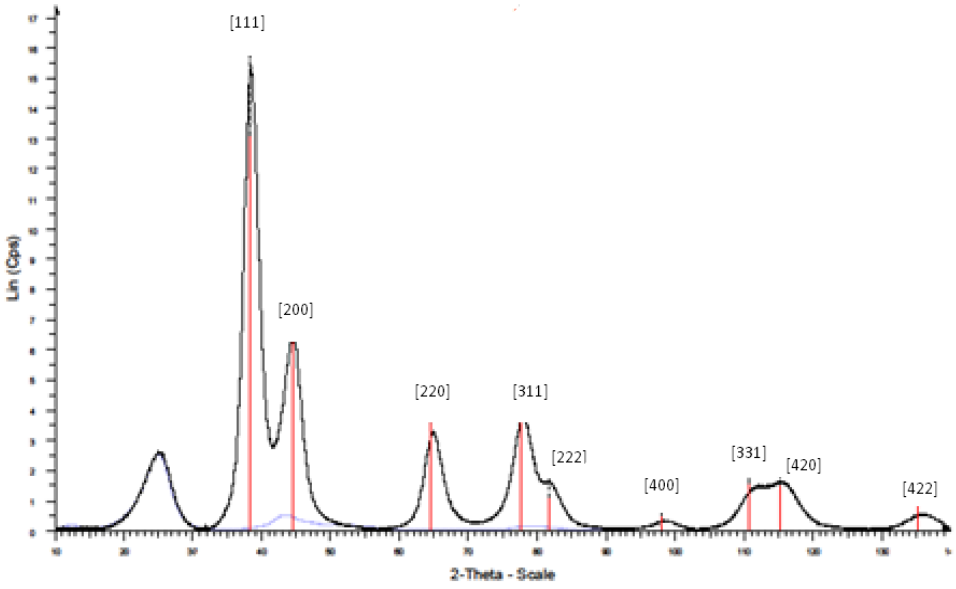


**Figure 2-4: Powder XRD pattern of prepared catalyst. Black line is the data, red vertical lines are FCC metallic gold reference, blue is the carbon support.**

The broad peak at ~25° is due to the graphitic region of carbon support. The red vertical lines correspond to the predicted positions of the bulk gold FCC lattice. The Millar indices of each and every peak can be calculated by using Equation 2-3.

# 3.3 X- Ray absorption spectroscopy (XAS)

XAS is a powerful technique used to determine the geometric and electronic features of a species[7,8]. It can be divided in to two subdivisions, X-ray Absorption Near Edge Structure (XANES) and Extended X-ray Absorption Fine Structure (EXAFS). XANES is usually used to find out the oxidation state of the metal and EXAFS are mainly used to investigate the particle size, coordination geometry etc. During the analysis, an X-ray beam having energy $h\upsilon$ is directed through the sample, if that X-ray energy is higher than the binding energy of the metal $E_b$ then it gives an absorption peak in the spectrum. The kinetic energy of emitted electron $E_k$ is given as,

$$E_k = h\upsilon + \mathrm{E_b} \qquad \textbf{[2-5]}$$

Where, $h$ is the Planck constant and $\upsilon$ is the frequency of radiation. A typical fine structure from Au foil at 300 K is shown in Figure 2-5.

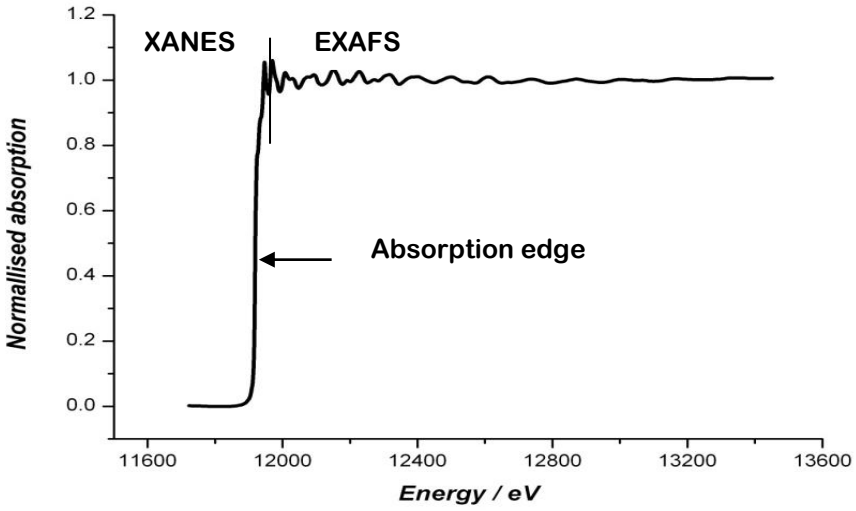


**Figure 2-5: XAS spectrum of an Au foil at 300 K.**

The absorption edge is proportional to the concentration of the sample. The XANES region arises generally due to the electronic transitions from the core level to higher unfilled or partially filled orbitals, e.g. $s \rightarrow p$, or $p \rightarrow d$. The ejected electron will interact with the surrounding atom scattered and produce EXAFS spectrum. The

absorption increases when a positive interference occurs and it decreases in the case of negative interferences[9,10].

The data fitted both in k-space and its corresponding Fourier transform of an Au foil are shown in Figure 2-6.

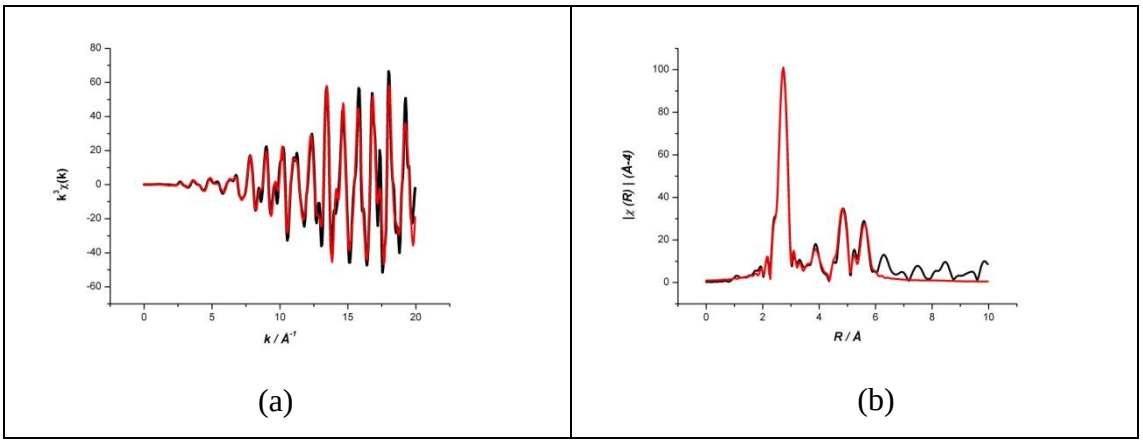


**Figure 2-6: (a) $k^3$ weighted Au $L_{III}$ edge experimental data (black) and fit (red) and (b) corresponding Fourier transform for the Au foil at 20 K.**

The amplitude of the EXAFS oscillations is proportional to the number of neighbours, whilst the phase depends on the distance as given by Equation 2-6.

$$\chi(k) = \sum_j A_j\,(k)\sin\left(2kr_j + \phi_j(k)\right) \qquad \textbf{[2-6]}$$

Where $\chi(k)$ is the EXAFS function, $j$ is the label of the coordination shells around the electron-emitting atom, $A_j(k)$ is the amplitude term, $r_j$ is the distance between the central atom and the atoms in the $j^{th}$ shell, and $\varphi(k)$ is the back scattering phase shift.

$A_j(k)$ defined as,

$$A_j(k) = N_j \frac{e^{-2r_j/\lambda(k)}}{kr_j^2} S_0^2(k) F_j(k) e^{-2k^2\sigma_j^2} \qquad \textbf{[2-7]}$$

Where, $N_j$ is the coordination number of atoms in the $j^{th}$ shell, $S_0$ is the amplitude reduction factor, $F_j$ is the backscattering amplitude from the $j^{th}$ atom, and is element specific, $\lambda$ is the inelastic mean free path of the electron and $\sigma^2$ is the mean squared displacement of atoms in the sample[8].

The data is often presented as a Fourier transform, which is akin to the radial distribution function. Further details are beyond the scope of this thesis as the analysis was conducted by a colleague, Mr. S.W.T Price.

### 3.3.1 XAS measurements

X–ray absorption spectroscopy (XAS) measurements were carried out at National Synchrotron Light Source (NSLS) at Brookhaven National Laboratories, USA. The station operates with the bending magnet source and Si (311) crystal monochromator optimized in the range of 8-35 keV. Ring energy was 2.8 GeV. Measurements were taken at the Au $_{LIII}$ edge. The monochromator was detuned 25 % at the Au $L_{III}$ edge to minimize higher harmonics. For the EXAFS measurements, the gold foil was mounted within a sample holder in the beam line. A reference was run at 300 K before the temperature was reduced to 20 K by a displex cooling unit and the reference run at low temperature The gold deposited on carbon nanoparticles (Au/C) were pressed into a rectangular pellet at a pressure of 2 tonnes in a pellet press and mounted in a sample holder.

The analysis was carried out by Mr. S. W. T Price. The main purpose of EXAFS analysis is to determine the shape of the catalyst particles.

## 3.4 Electrochemical characterizations

Electrochemical methods are used both to characterise the catalytic materials and to assess their electrocatalytic activity in various electrochemical (fuel cell) reactions. The electrode preparation, various electrochemical techniques used in this work and the cyclic voltammogram of polycrystalline gold disc are explained in detail below.

## 3.4.1 Ink preparation

5 mg of the prepared catalyst was mixed with 5 ml of a solvent mixture containing 9:1 water: IPA by volume. This mixture was chosen as it gave the smoothest layer on the electrode. Then a volume of Nafion® was added to the solvent according to Equation 2-8 and the solution was sonicated for 30 min. The purpose of adding Nafion® is to stick the ink on the electrode and to have a smooth surface of electrode.

$$V_{Nafion}\,(\mu l) = \frac{Mass\ of\ catalyst\ (mg) \times wt\ \%\ of\ Nafion^{®}\ \ w.r.t.\ solid \times 1000}{Wt\ \%\ of\ Nafion^{®} \times Density\ of\ Nafion^{®}} \qquad \textbf{[2-8]}$$

According to the above calculation 14 μl of the Nafion® was added in to the catalyst mixture before the sonication to obtain a 15 wt % Nafion® in the dried catalyst layer.

## 3.4.2 Electrode preparation

Prior to depositing the catalyst suspension, the glassy carbon (GC) disc electrode (5 mm diameter) was polished with Alumina (0.05 μm diameter) to obtain a mirror finish and sonicated in purified water (milli–Q system) to obtain a clean disc. The GC disc was then heated under an IR lamp for 10 min. The required volume of the ink, corresponding to a metal loading of 10 μg $cm^{-2}$ and the ink concentration 1 mg $ml^{-1}$ given by Equation 2-9 was deposited on to the surface of the disc. The suspension was then allowed to dry under the IR lamp for 1 min and then in air until complete evaporation of the solvent occurred.

$$V\,(\mu l) = \frac{Metal\ loading\ (\mu g\ cm^{-2}) \times 1000 \times electrode\ area}{Metal\ content\ (wt\ \%) \times ink\ concentration\ (mg_{\ catalyst} / ml_{\ solvent})} \qquad \textbf{[2-9]}$$

## 3.4.3 Cell and Instrumentation

All the experiments in this work were carried out using a Rotating Disc Electrode (RDE). The RDE system is a convective electrode where hydrodynamic Equation convective–diffusion results in steady state mass transport conditions. When the RDE rotates it pulls the solution towards the disc and then flings it out towards the sides. Thus the RDE keeps the concentration of species in the solution at their bulk value throughout except very close to the electrode surface. The rate of diffusion of the species depends on the rotation speed of the disc in a region called the Nernst diffusion layer, the thickness of which depends on the rotation rate. Schematic diagram of a typical RDE cell is shown in Figure 2-7.

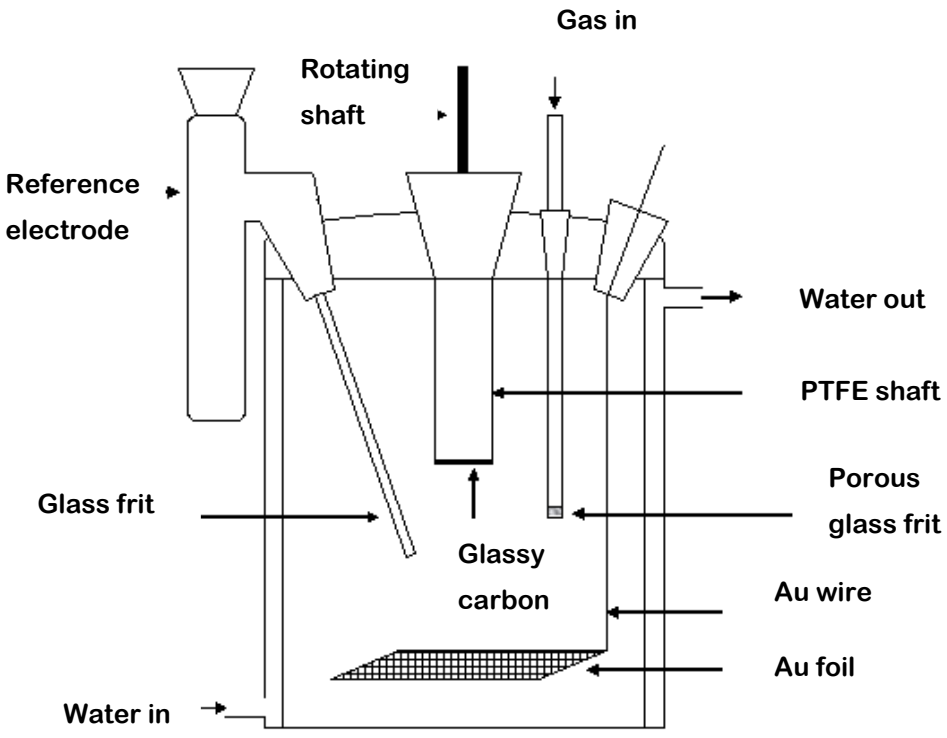


**Figure 2-7 : Electrochemical cell for RDE measurements[11].**

The potential was applied with an Autolab potentiostat/galvanostat PGSTAT 30 and the experiments were controlled with General Purpose Electrochemical System (GPES 4.9). The experiments were performed using a standard three electrode electrochemical cell. The electrolyte used for most of the experiments was

0.5 mol $dm^{-3}$ KOH. 1 mol $dm^{-3}$ $H_2SO_4$ was used in cyclic voltammetry for the determination of the real area of gold. The reference electrode used in basic electrolyte was Hg/HgO, $OH^-$ (MMO) electrode calibrated as -0.07 V vs. a saturated calomel electrode in 0.1 mol $dm^{-3}$ NaOH solution and in acidic electrolyte it was $Hg/Hg_2SO_4$, $H^+$ (MMS) electrode calibrated against Pt/ $H_2$ and the potential was 0.69 V. The counter electrode was a gold foil.

All the potentials are given with respect to the MMO and MMS reference electrodes where applicable. The geometrical diameter of Au and GC disc is 5 mm.

## 3.4.4 Cyclic voltammetry

Cyclic voltammetry is a type of potentiodynamic voltammetric measurement and is used to study the redox properties of electroactive species. The voltage applied to the working electrode is varied and the current is measured with respect to the voltage. Starting at a fixed value of potential, the potential is varied to a defined value at a given rate. At this potential the direction is reversed and the same potential window is scanned in the opposite direction. The species formed by the oxidation in the forward scan being reduced in the backward scan.

There are usually three electrodes in the system. They are the working electrode, reference electrode and the counter electrode. The potential is measured between the reference electrode and the working electrode; and the current is measured between the working electrode and the counter electrode.

### 3.4.4.1 Cyclic voltammetry measurements

The cell was filled with freshly prepared 1 mol $dm^{-3}$ $H_2SO_4$ and the electrodes were connected to the Autolab potentiostat. The electrochemical cell was purged with nitrogen gas and the electrode rotated at 1000 rpm for 15 minutes to remove all the dissolved oxygen. The nitrogen flow was then reduced and blown gently over the top

of the electrolyte. The electrode was cycled from 0 to 0.96 V vs. MMS. Scan rate 20 mV $s^{-1}$.

CV in base is similar to acid. The electrode was cycled from -0.3 V to 0.6 V vs. MMO. Scan rate 10 mV $s^{-1}$.

## 3.4.4.2 CV of gold in acid and surface area determination

The electrochemistry of gold in acidic media is frequently viewed in very simple terms as involving only double-layer charging/discharging and monolayer oxide formation/ removal phenomena (Figure 2-8).

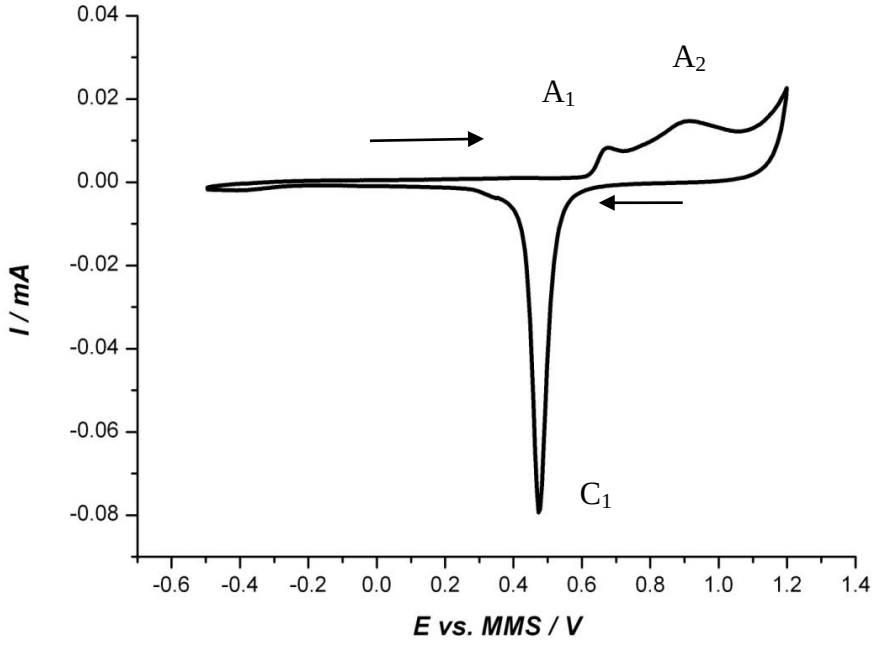


**Figure 2-8: CV of gold disc (5 mm diameter) electrode in 1 mol $dm^{-3}$ $H_2SO_4$, deoxygenated with $N_2$. Scan rate 20 mV $s^{-1}$. Arrows indicate sweep direction.**

### (a) Double layer region (-0.3 V to 0.3 V)

The current flowing in the double layer region is not from a chemical reaction but from the charging of the double layer by the electrical charges on the electrolyte migrating to the electrode surface.

## (b) Oxide region (0.3 V to 1.0 V)

$$Au + H_2O \rightarrow AuOH + H^+ + e \quad \textbf{[2-10]}$$

$$AuOH \rightarrow AuO + H^+ + e \quad \textbf{[2-11]}$$

The monolayer oxide formation process commences at around 0.65 V and oxygen evolution commences around 1 V in the positive going sweep with respect to the MMS reference electrode. The absence of sharp peak on the positive sweep and significant differences in the potential ranges (hysteresis) for oxide formation and removal clearly show that the process involved does not occur in a highly reversible manner. The origin of hysteresis in the monolayer oxide formation/removal process is usually attributed to gradual changes in the nature of oxide film. During the growth process dipole species ($Au^{\delta+}\ldots OH^{\delta-}$) are produced, which at appreciable coverage, repel one another. Such repulsion raises the energy required to generate additional dipoles hence an increase in potential is required to attain an increasing coverage. This is evidently the reason why the monolayer oxide formation response is an extended plateau rather than a sharp peak[12,13]. The process involved is outlined schematically in Figure 2-9. Rotation of some of the surface dipoles, a process also referred to as place-exchange, relieves much of the lateral repulsion or stress in the surface layer, resulting in a more stable surface deposit. The two peaks $A_1$ and $A_2$ in the anodic scan may be due to the different Au oxides formed. In the negative sweep the dipole coverage (and any residual stress) is progressively reduced. No electrostatic repulsion barrier is developed in this case and a relative sharp cathodic peak $C_1$, is observed[14].

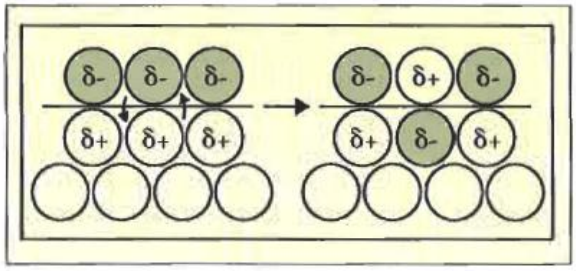


**Figure 2-9: Schematic representation of the post electrochemical, place-exchange reaction involved in a monolayer oxide formation[13].**

The real surface area of the Au cannot be obtained precisely, but it can be estimated from the oxygen adsorption measurements. The coverage can be obtained by desorbing the layer by applying a cathodic potential sweep and integrating to determine the charge passed. The position and the area (charge) of the cathodic peak are found to depend on the start potential of the cathodic sweep. A monolayer is formed up to a certain potential[15].

The dependence of the Au oxide stripping charge on the upper potential limit of the cyclic voltammogram obtained at 20 mV $s^{-1}$ is shown in Figure 2-10.

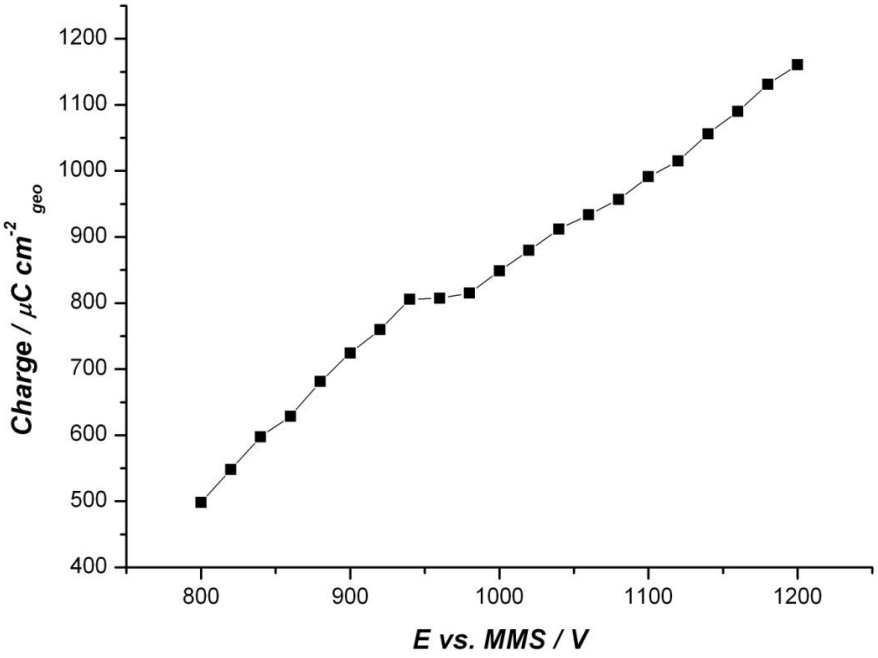


**Figure 2-10: Oxygen coverage on an Au electrode (5nm diameter) as a function of potential in 1 mol $dm^{-3}$ $H_2SO_4$ at the particular anodic potential limit. Scan rate 20 mV $s^{-1}$.**

There is a near linear increase in charge followed by a plateau from 940 mV to 980 mV. Then a second near linear increase with increasing potential limit is observed. This plateau is attributed to a monolayer of oxide and the charge can be used to determine the real surface area of the gold electrode. For this reason an upper limit of 0.96 V was used in acid CVs of gold to determine the real surface area of gold. The measurements are performed in 1 mol $dm^{-3}$ $H_2SO_4$. The real surface area of gold (Ar) was determined from the stable cyclic voltammograms by charge

integration under the oxide reduction peak and using a value of 400 μC $cm^{-2}$ for the reduction of an oxide monolayer[16].

The corresponding plot of oxygen coverage as a function of potential for a 20 wt % Au/C catalyst is shown in Figure 2-11.

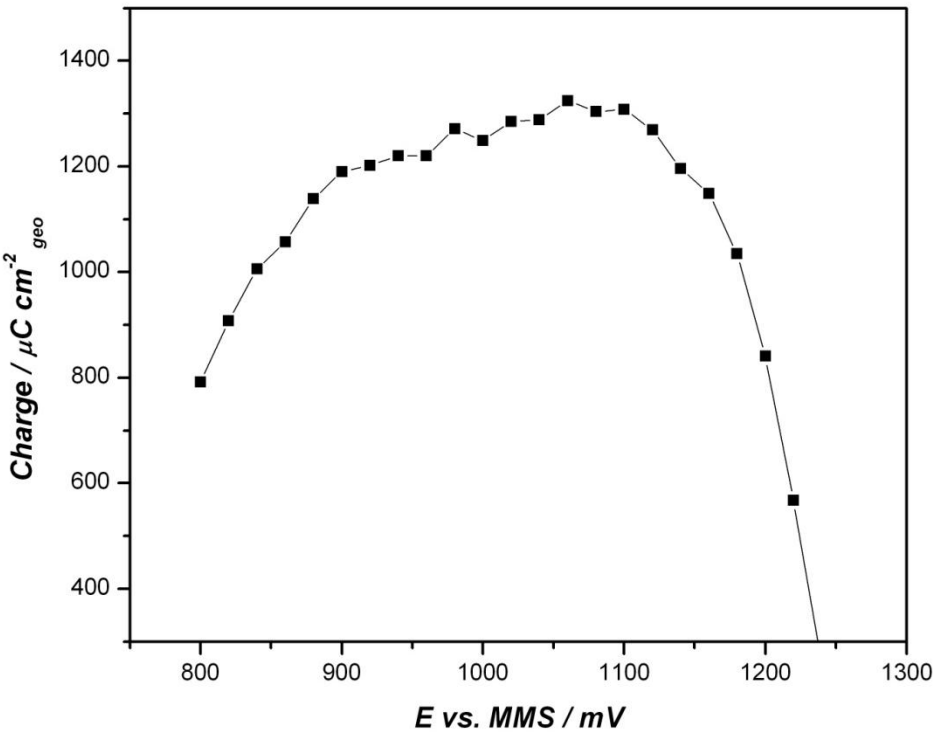


**Figure 2-11: Oxygen coverage on 20 wt % Au / C on GC electrode (5nm diameter) as a function of potential in 1 mol $dm^{-3}$ $H_2SO_4$ at the particular anodic potential limit. Scan rate 20 mV $s^{-1}$.**

The charge increases up to 940 mV where a plateau is reached until 980 mV. After this point the behaviour of the electrode differs from the bulk gold electrode, as the charge starts to decrease. This is because beyond 1000 mV dissolution of the Au nanoparticles occurs and, as the charge was determined using the oxide stripping peak, the measured charge decreases. Therefore a limit of 960 mV will be used in all acid CVs of the prepared catalyst to ensure complete monolayer formation and to ensure that the electrode surface is not damaged.

## 3.4.4.3 CV in base

The voltammetric features in alkaline solution are similar to those observed in acidic electrolytes. Figure 2-12 shows a typical CV of bulk gold in alkaline solution.

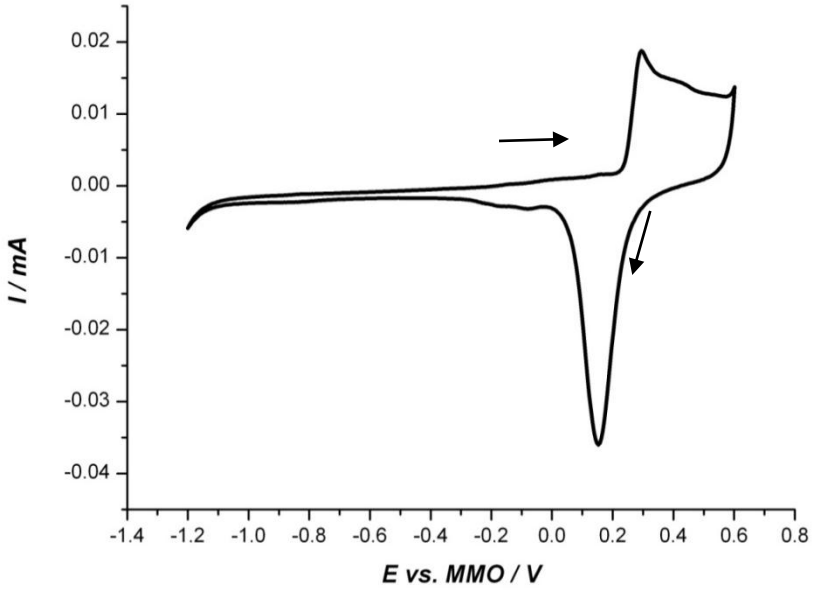


**Figure 2-12: CV of gold disc (5 mm diameter) electrode in 0.5 mol dm$^{-3}$ KOH, deoxygenated with $N_2$. Scan rate 10 mV s$^{-1}$. Arrows indicate sweep direction.**

In alkaline solutions, chemisorption of $OH^-$ on Au starts around 0.05 V, with increasing surface coverage resulting at more positive voltages. This adsorbed $OH^-$ plays a governing role in the surface electrochemistry of Au in alkaline media. Adsorption of $OH^-$ can be formally written as a partial charge transfer reaction,

$$Au + OH^- \rightarrow Au - OH_{ads}^{(1-x)} + xe^- \qquad \textbf{[2-12]}$$

$x$ varies in between 1 and 0. Adsorption of water on top of partially charged chemisorbed hydroxide species on Au can be formally written as,

$$Au - OH^{y-} + H_2O \rightarrow [Au - OH_{ads}^{y-} - H_2O] \qquad \textbf{[2-13]}$$

Where $y$ =1- $x$, anodic currents observed at E ≥ 0.15 V during the positive voltage scans result from the following oxidation reaction,

$$Au - OH^{y-} + OH^{-} \rightarrow AuO + H_2O + (1+y)e^{-} \quad \textbf{[2-14]}$$

In the negative scan, the AuO is reduced through the reverse step of Equation [2-14].

Tremiliosi – Filho *et al.*[17] have shown and thus the oxide reduction peak could have been used to determine the Au surface area as that in alkaline solution the surface charge for oxide monolayer reduction is practically equal to that in acidic solution. However, in this work the real surface area calculations were carried out in 1 mol $dm^{-3}$ $H_2SO_4$ scanned from 0 V to 0.96 V vs. MMS. Scan rate 20 mV $s^{-1}$ to maintain consistency.

# 4. References


(1) Brust, M. W., M.; Bethell,D.;Schiffrin.D.J.;Whyman.R.1994,801 *Journal of the Chemical Society, Chemical Communications* **1994**, 801

(2) Vengatesan, S.; Kim, H.-J.; Kim, S.-K.; Oh, I.-H.; Lee, S.-Y.; Cho, E.; Ha, H. Y.; Lim, T.-H. *Electrochimica Acta* **2008**, *54*, 856.

(3) Sirk, A. H. C.; Hill, J. M.; Kung, S. K. Y.; Birss, V. I. *The Journal of Physical Chemistry B* **2003**, *108*, 689.

(4) Ruska, E. *Angewandte Chemie International Edition in English* **1987**, *26*, 595.

(5) Ladd, M. F. C. *Physics Education* **1972**, *6*, 368.

(6) Patterson, A. L. *Physical Review* **1939**, *56*, 978.

(7) Penner-Hahn, J. E. *Coordination Chemistry Reviews* **1999**, *190-192*, 1101.

(8) Russell, A. E.; Rose, A. 2004; Vol. 104, p 4613.

(9) Akolekar, D. B.; Bhargava, S. K.; Foran, G. *Radiation Physics and Chemistry* **2006**, *75*, 1948.

(10) Koningsberger, D. C.; Mojet, B. L.; van Dorssen, G. E.; Ramaker, D. E. *Topics in Catalysis* **2000**, *10*, 143.

(11) Wells, P. P. PhD thesis, University of Southampton, 2007.

(12) Conway, B. E. *Progress in Surface Science* **1995**, *49*, 331.

(13) Burke, L. D.; Patrick, F. N. *Gold bulletin* **1997**, *30*, 43.

(14) Hamelin, A.; Martins, A. M. *Journal of Electroanalytical Chemistry* **1996**, *407*, 13.

(15) Burke, L. D.; Jean, M. M.; Patrick, F. N. *Journal of Solid State Electrochemistry* **2003**, *V7*, 529.

(16) Burke, L. D.; Anthony, P. O. M. *Journal of Solid State Electrochemistry* **2000**, *V4*, 285.

(17) Tremiliosi-Filho, G.; Dall'Antonia, L. H.; Jerkiewicz, G. *Journal of Electroanalytical Chemistry* **1997**, *422*, 149.

# Chapter Three: Characterisations of Catalysts

## 1. Introduction

This Chapter describes the elemental analysis, TEM, XRD, EXAFS and cyclic voltammetry including UPD characterisations of the four different Au/C catalysts. The results have been collected here so that they may be readily referred to in subsequent Chapters and to avoid repetition.

## 2. Results and Discussion

### 2.1 Elemental analysis

Metal assay of the prepared catalysts was carried out using Inductive Coupled Plasma Optical Emission Spectroscopy (ICP OES) by Medac Ltd. The results are given below in Table 3-1.

**Table 3-1: Elemental analysis of the prepared catalysts.**

| Catalyst | Percentage of gold ( wt % ) |
|---|---|
| $Au_{3.2}$ | 17.1 |
| $Au_{5.4}$ | 14.8 |
| $Au_{6.0,wide}$ | 20.4 |
| $Au_{6.0,narrow}$ | 25.6 |

All the catalysts were heat treated to above 300 °C. In general, thiol compounds should have been eliminated at this high temperature. Analysis of the S content by Medac confirmed that the residual S was < 1 wt % in all cases.

# 2.2 TEM

The TEM analysis was carried out at the Johnson Matthey Technology Centre (JMTC) by one of their technicians. Figures 3-1 A-D show representative TEM images of each Au/C catalysts together with the histograms from which their particle size distributions were determined.

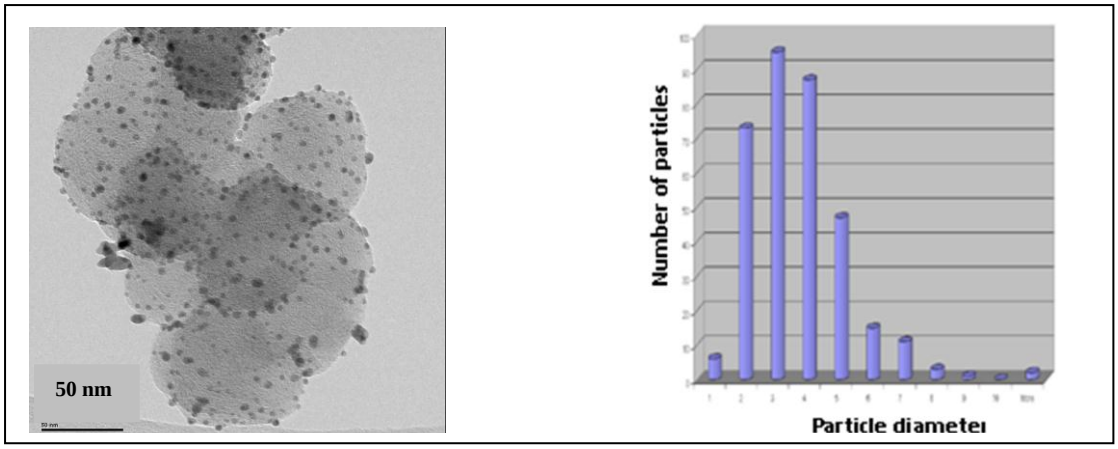


**Figure 3-1 A: TEM of catalyst $Au_{3.2}$ at scale bar 50 nm and particle size distribution from TEM analysis (frequency y- axis, diameter x-axis).**

Figure 3-1 A shows that the particles observed by TEM were well dispersed on the carbon support and were evenly distributed throughout the sample. The majority of the particles are spherical but some of them appear ellipsoidal due to aggregation. The histogram shows a Gaussian distribution of the particles with most particles having a diameter of 2 to 4 nm.

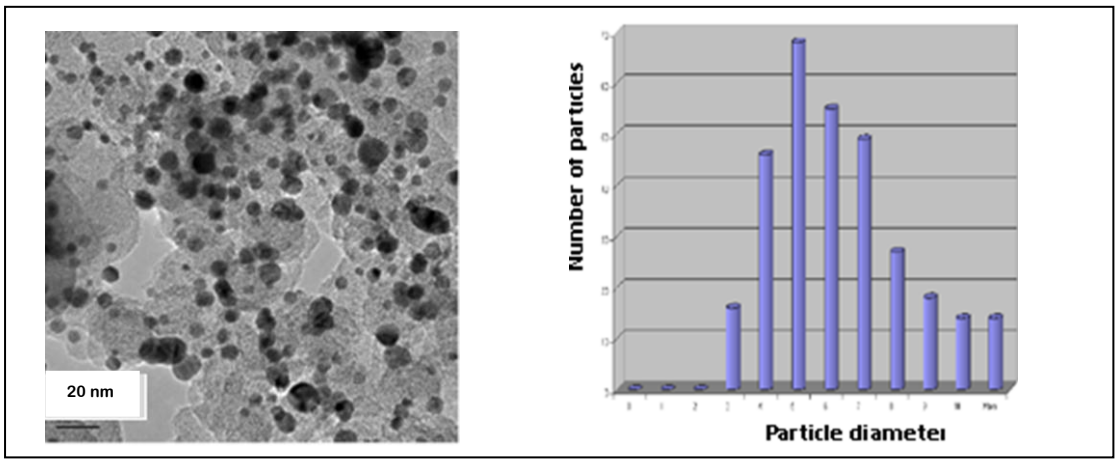


**Figure 3-1 B: TEM of catalyst $Au_{5.4}$ at scale bar 20 nm and particle size distribution from TEM analysis (frequency y- axis, diameter x-axis).**

Figure 3-1 B shows that the particles in the $Au_{5.4}$ catalyst were less well dispersed on the support. A high density of particles was observed, with most of the particles agglomerated together. The majority of the particles had diameters in the range 4-7 nm.

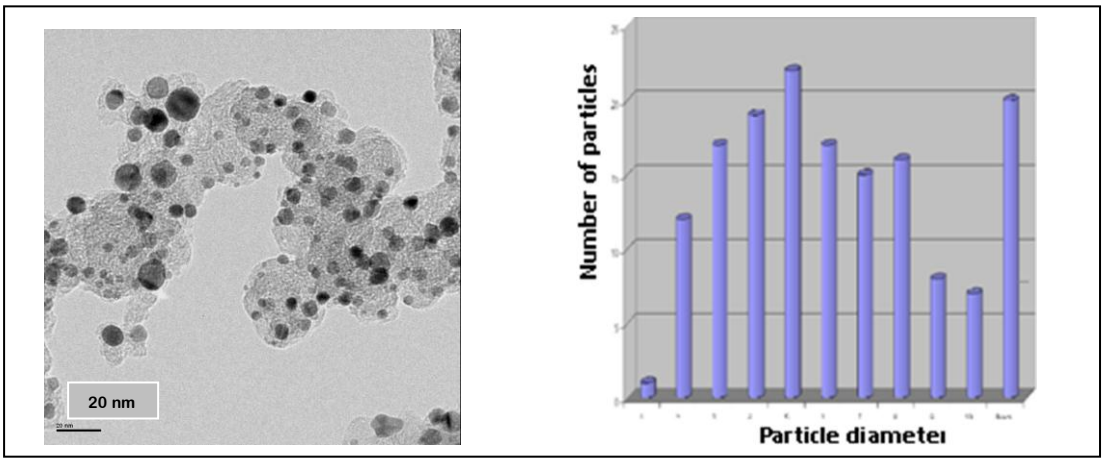


**Figure 3-1 C: TEM of catalyst $Au_{6.0,\ wide}$ at scale bar 20 nm and particle size distribution from TEM analysis (frequency y-axis, diameter x-axis).**

The TEM image for catalyst $Au_{6.0,\ wide}$ is shown in Figure 3-1 C. A low density of uniformly distributed nanoparticles was observed, whereas in other areas a higher particle density but with individual nanoparticles still visible was observed. The histogram shows that the distribution is not well represented by a Gaussian. A broad distribution of particle sizes ranging from 3 to 8 nm, and a large number of particles greater than 10 nm were observed.

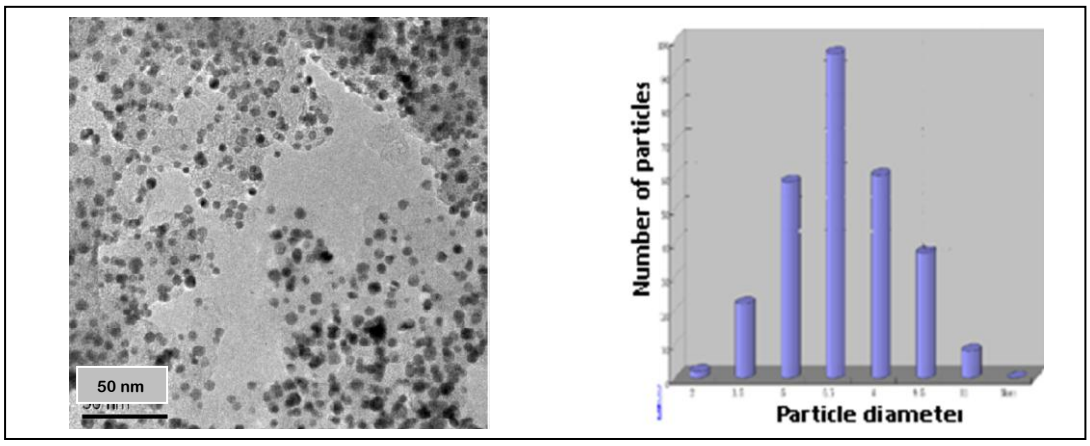


**Figure 3-1 D: TEM of catalyst $Au_{6.0,\ narrow}$ at scale bar 50 nm and particle size distribution from TEM analysis (frequency y-axis, diameter x-axis).**

In the TEM image for catalyst $Au_{6.0,\ narrow}$ shown in Figure 3-1 D, well dispersed particles on carbon support were observed. The particles are almost spherical in shape, with a Gaussian distribution shown on the histogram. The majority of the particles are centred at 6.5 nm.

Calculated particle sizes (number weighted) of each catalyst from TEM analysis are tabulated in Table 3-2.

**Table 3-2: TEM data for the prepared Au/C catalysts, where n is the number of particles observed.**

| Catalysts | n | Mean / nm | Standard deviation / nm |
|---|---|---|---|
| $Au_{3.2}$ | 340 | 3.2 | 1.6 |
| $Au_{5.4}$ | 307 | 5.4 | 1.4 |
| $Au_{6.0,wide}$ | 154 | 6.0 | 3.0 |
| $Au_{6.0,narrow}$ | 283 | 6.0 | 1.8 |

The mean diameters of $Au_{6.0,\ wide}$ and $Au_{6.0,\ narrow}$ are similar even though these catalysts were heated to different temperatures. However, the standard deviation of $Au_{6.0,\ wide}$ is almost double compared to that of $Au_{6.0,\ narrow}$. The reason may be due to the different heat treatment techniques involved in the preparation of the above catalysts.

## 2.3 XRD

The XRD analysis was carried out at JMTC by one of their technicians. Figure 3-2 shows the powder XRD patterns of the prepared Au/C catalysts. The peak assignment for each peak is also indicated in this Figure.

(A)

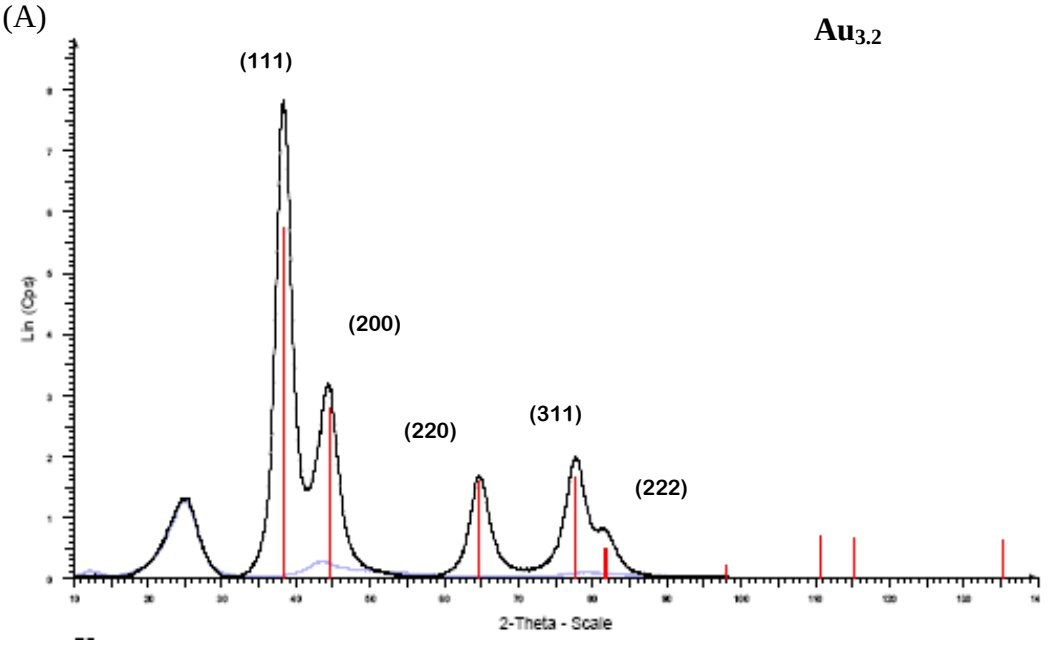


**Figure 3-2 (A) : Powder XRD pattern of (A) $Au_{3.2}$ Black line is the data, red vertical lines are FCC metallic gold reference, blue is the carbon support.**

(B)

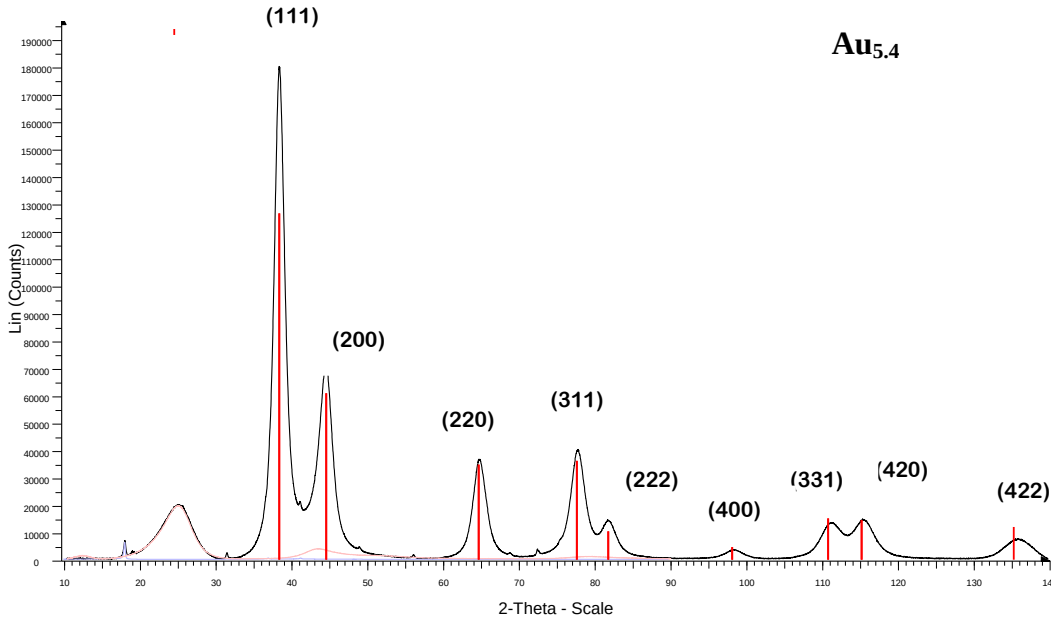


**Figure 3-2 (B) : Powder XRD pattern of (A) $Au_{5.4}$ Black line is the data, red vertical lines are FCC metallic gold reference, blue is the carbon support.**

(C) **$Au_{6.0,\ wide}$**

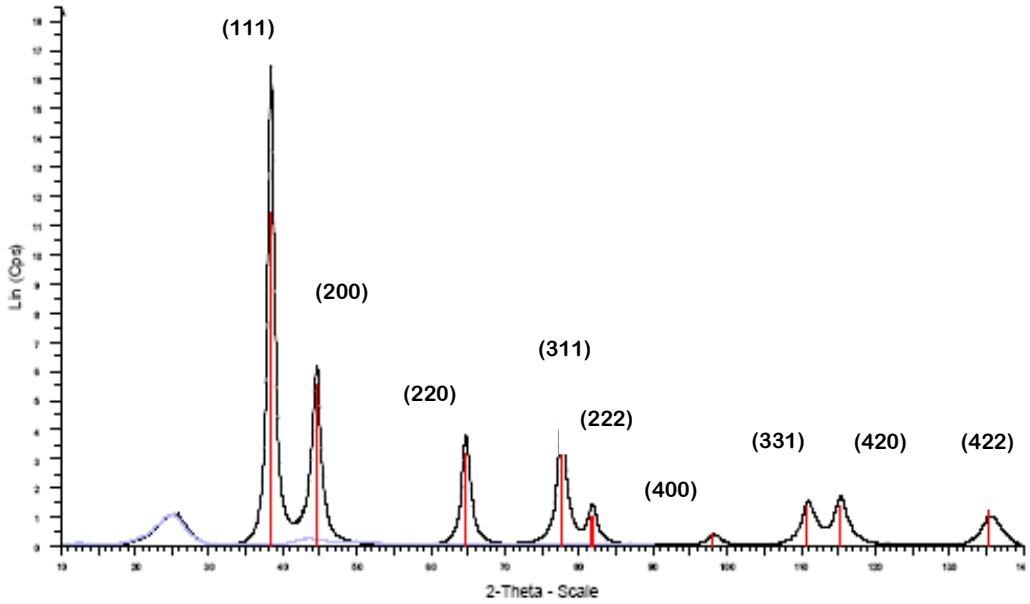


**Figure 3-2 (C): Powder XRD pattern of $Au_{6.0,\ wide}$ .Black line is the data, red vertical lines are FCC metallic gold reference, blue is the carbon support.**

The broad peak at ~25° is due to the graphitic carbon of the support. All the peaks become narrower and shifted slightly to the left as the particle size increases. Narrow peaks indicate higher crystallinity of the catalyst. The XRD of $Au_{6.0,\ narrow}$ could not be analysed due to the insufficient amount of sample.

Rietveld analysis was carried out at JMTC to calculate the cubic cell constants and the crystallite sizes of the Au particles. The average values are tabulated in Table 3-3.

**Table 3-3: Rietveld refinement data.**

| Catalyst | Cubic cell constant / Å | Au crystallite size / nm |
|---|---|---|
| $Au_{3.2}$ | 4.0727 | 3.27 |
| $Au_{5.4}$ | 4.0721 | 3.84 |
| $Au_{6.0,wide}$ | 4.0741 | 7.99 |
| Au reference | 4.0786 | N/A |

Table 3-3 shows that the nanoparticles exhibit the same FCC structure as the metallic gold reference, but with slightly smaller lattice parameters. The reason for this observation could be that the atoms on the surface of a nanoparticle can contract

towards the core to minimize the surface energy and is typical of supported nanoparticles[1].

# 2.4 XAS

XAS measurements were carried out at NSLS at Brookhaven National Laboratories, USA. The analysis was done by Mr. S. W. T Price. Since all the catalysts were prepared in the same method only one catalyst (catalyst $Au_{5.4}$) was selected for EXAFS analysis.

The data was fitted in k-space and is shown with its corresponding Fourier transform in Figure 3-3.

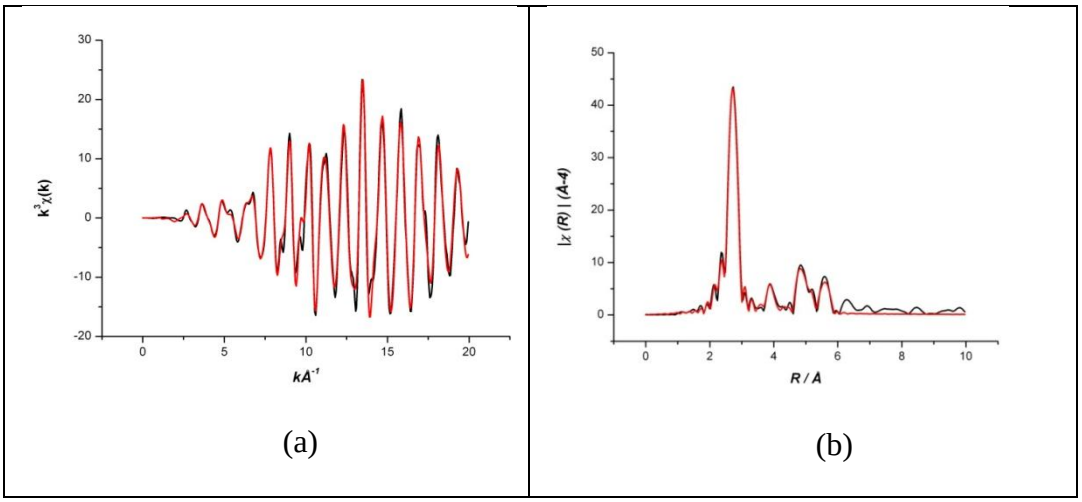


**Figure 3-3: (a) $k^3$ weighted Au $L_{III}$ edge experimental data (black) and fit (red) and (b) corresponding Fourier transform for the catalyst Au $_{5.4.}$**

Parameters determined from EXAFS fits using Artemis and tabulated in Table 3-4.

**Table 3-4: EXAFS parameter fitted using Artemis.**

| | 1st shell | | 2nd shell | | 3rd shell | | 4th shell | | Isotropic bond contraction ** | $E_0$ / eV | R factor |
|---|---|---|---|---|---|---|---|---|---|---|---|
| | CN | $\sigma^2$ / Å$^2$ | CN | $\sigma^2$ / Å$^2$ | CN | $\sigma^2$ / Å$^2$ | CN | $\sigma^2$ / Å$^2$ | | | |
| $Au_{5.4}$ 20 K | 11.1 ± 0 .56 | 35 ± 1 | 3.96 ± 1.55 | 42 ± 13 | 23.01 ± 4.55 | 57 ± 7 | 11.42 ± 2.11 | 59 ± 8 | -0.0070 ± 0.0005 | 4.65 ± 0.40 | 0.0199 |
| $Au_{5.4}$ 40 K | 11.23 ± 0.56 | 36 ± 2 | 4.05 ± 1.60 | 45 ± 13 | 23.44 ± 4.71 | 60 ± 8 | 11.79 ± 2.23 | 64 ± 9 | -0.0075 ± 0.0005 | 4.18 ± 0.41 | 0.0202 |
| $Au_{5.4}$ 60 K | 11.18 ± 0.56 | 39 ± 2 | 3.87 ± 1.58 | 48 ± 14 | 24 ± 5.06 | 67 ± 9 | 12 ± 2.34 | 70 ± 10 | -0.0076 ± 0.0005 | 4.67 ± 0.40 | 0.0207 |

The particle size of the catalyst was determined from the EXAFS data using the method of Jentys[2] with the value of 6.05 ± 0.82 nm being found using the average coordination numbers obtained.

**Table 3-5: Comparison of sizes obtained from different shells.**

| Catalyst | Average Size (1st shell) / nm |
|---|---|
| $Au_{5.4}$ 20 K | 5.97 ± 0.82 |
| $Au_{5.4}$ 40 K | 6.16 ± 0.82 |
| $Au_{5.4}$ 60 K | 6.03 ± 0.82 |
| EXAFS Averages | 6.05 ± 0.82 |

From EXAFS data, it is possible to determine the shape of the particles. Usually the ratio between the 3rd shell coordination number and the 1st shell coordination number ($N_3/N_1$) is used to determine the shape of the particle. The ratio $N_3/ N_1$ at each temperature is tabulated in Table 3-6.

**Table 3-6: Determination of the shape of the catalyst.**

| Catalyst | 1st Shell coordination number ($N_1$) | 3rd Shell coordination number ($N_3$) | $N_3/ N_1$ |
|---|---|---|---|
| $Au_{5.4}$ 20 K | 11.16 ± 0.56 | 23.01 ± 4.55 | 2.06 ± 0.54 |
| $Au_{5.4}$ 40 K | 11.23 ± 0.56 | 23.44 ± 4.71 | 2.09 ± 0.55 |
| $Au_{5.4}$ 60 K | 11.18 ± 0.56 | 24 ± 5.06 | 2.15 ± 0.59 |
| Foil | 12 | 24 | 2 |

Usually, the ratios $N_3/N_1$ above two are considered as spherical particles whereas the ratios below two are considered as distorted cubic or slab shaped clusters. In these cases at all three temperatures the ratio of $N_3/ N_1$ is above two; therefore the shape of the catalyst is spherical. As all the catalysts were prepared using the same methodology, it is concluded that all the prepared catalysts are indeed spherical in shape.

Since the nanoparticle was prepared using the thiol as an encapsulating agent the presence of Au–S was tested to make sure the heat treatment eliminated the S as expected. The fitting at the first shell coordination showed that there is no S present on the catalyst thus demonstrating that the catalyst is uncontaminated.

# 2.5 Cyclic Voltammogram (CV)

The prepared catalysts were electrochemically characterized by CV on a glassy carbon RDE as described in Chapter two section 3.4 and shown in Figure 3-4. The bulk gold is also incorporated in the Figure for the sake of comparing the efficiencies.

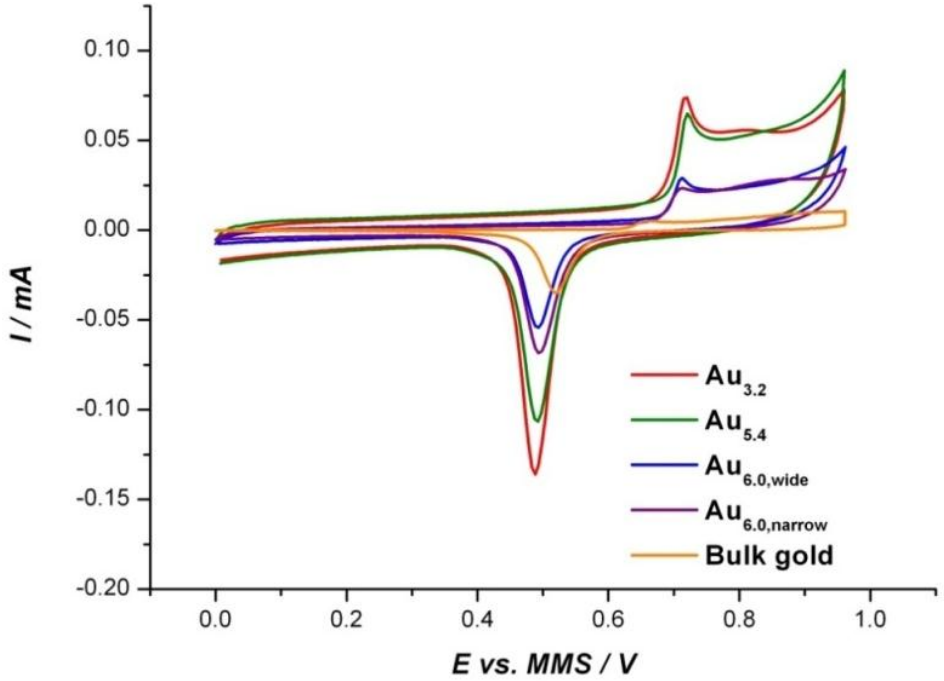


**Figure 3-4: CVs for the prepared catalysts on GC disc, and Gold disc (5 mm diameter) in $N_2$ saturated 1 mol $dm^{-3}$ $H_2SO_4$ at a scan rate 20 mV $s^{-1}$.**

The anodic peak at ~ 0.7 V corresponds to the formation of Au oxide species. In the reverse scan, Au oxide is reduced and the reduction peak is centred at ~0.45 V. A large increase in background current is observed for all of the carbon supported catalysts compared to the bulk gold. This is due to the double layer capacitance of carbon causing a higher current in the double layer region.

Table 3-7 summarizes the cathodic peak potentials and the Au real surface area of the bulk gold and the prepared catalysts.

**Table 3-7: Cyclic voltammetric parameters of the prepared catalysts and bulk gold.**

| Catalyst | Particle size / nm | Cathodic peak potential / V | Cathodic peak current / mA | The Au real area / $cm^2$ |
|---|---|---|---|---|
| $Au_{3.2}$ | 3.2 | 0.488 | 0.13 | 1.025 |
| $Au_{5.4}$ | 5.4 | 0.492 | 0.10 | 0.717 |
| $Au_{6.0,wide}$ | 6.0 | 0.493 | 0.07 | 0.402 |
| $Au_{6.0,narrow}$ | 6.0 | 0.493 | 0.07 | 0.58 |
| Bulk gold | N/A | 0.52 | 0.03 | 0.37 |

The Au real area is very much larger for the carbon supported catalysts in comparison with the bulk gold due to the high roughness of nanoparticles compared to the smooth polycrystalline gold. For the prepared catalysts with the smaller Au particle sizes, the onset of oxide formation is less positive compared to larger ones. This is due to the higher hydroxyl coverage on smaller ones. The cathodic peak current is larger than those for the catalysts with larger Au particle sizes due to the higher surface area of the smaller particles. The cathodic peak shifted towards the negative region with decreasing particle size. The shift of the cathodic scan reflects either a greater relative average of oxide or increased stability of the oxide[3].

## 2.6 UPD

The prepared catalysts were also characterised by recording the lead UPD voltammetric profile in a 0.1 mol $dm^{-3}$ NaOH + 1 mmol $dm^{-3}$ Pb (II) solution. An estimation of the size of the different facets present in the catalysts can be obtained by comparing the lead UPD profile of the nanoparticle with those obtained for the gold single crystal basal planes[4-6] .

The Pb UPD profile was studied using the following procedure with the electrode prepared using the method explained in Chapter two. Prior to any electrochemical study, the electrolyte was deoxygenated with $N_{2\,(g)}$ and the catalyst supported GC disc was cycled in a Pb (II) containing alkaline solution (0.1 mol $dm^{-3}$ NaOH in 1 mmol $dm^{-3}$ Pb $(NO_3)_2$) from -0.7 V to 0.8 V vs. MMO at a scan rate of 20 mV $s^{-1}$. At high potentials, a $PbO_2$ film is deposited. The well-known electrocatalytic properties of $PbO_2$ for the oxidation of organic species are helpful in removing the adsorbed organic species from the gold surface[6]. Following this, the electrode was cycled between - 0.7 V to 0.1 V vs. MMO. The cleaning being continued until the two consecutive scans overlapped.

Figure 3-5 shows the UPD pattern of the carbon supported catalysts, gold disc as well as the GC substrate.

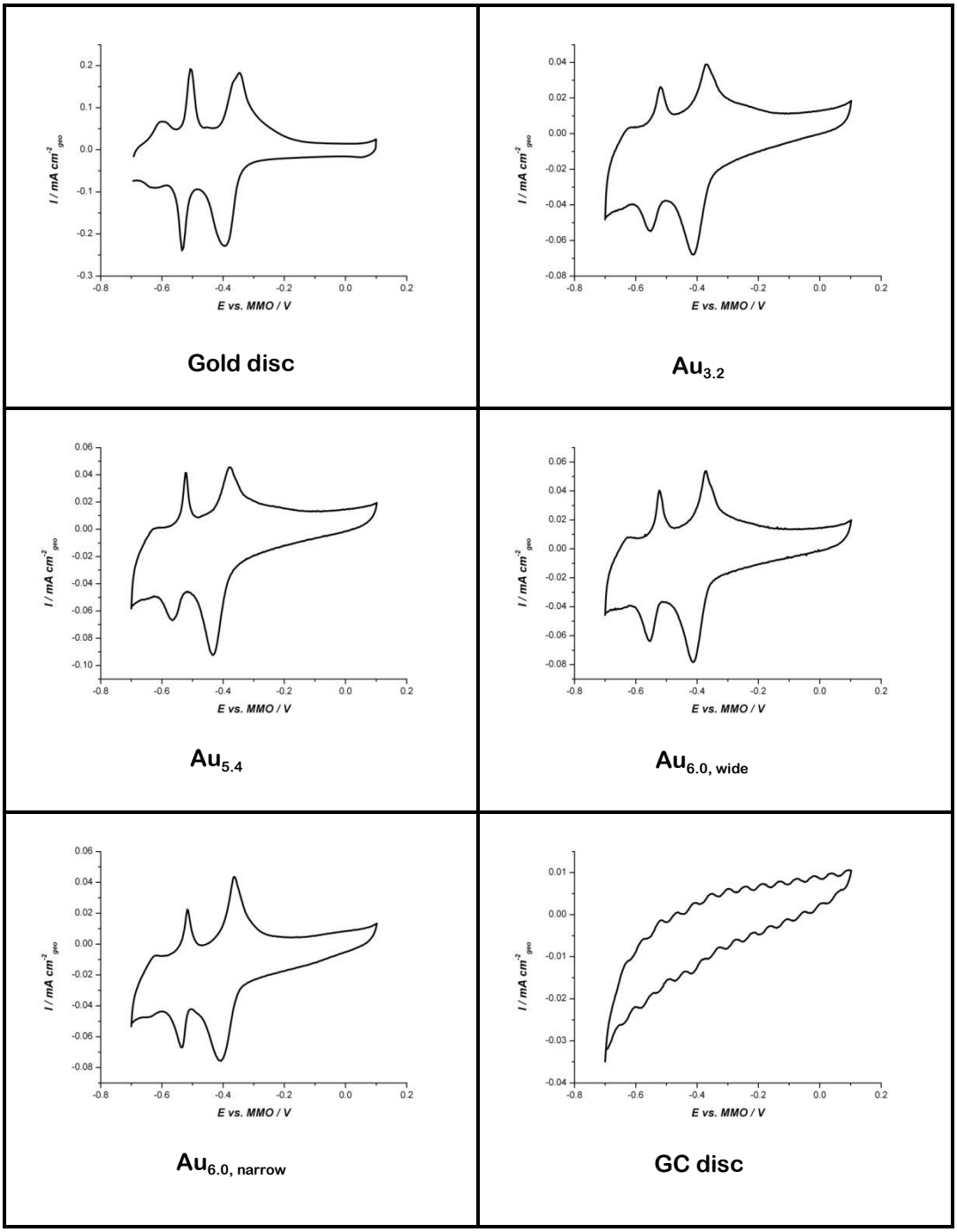


**Figure 3-5: Voltammetric profile of the bulk gold, prepared catalysts (Scan rate 20 mV $s^{-1}$) and GC disc(Scan rate 50 mV $s^{-1}$) in 0.1 mol $dm^{-3}$ NaOH + 1 mmol $dm^{-3}$ $Pb(NO_3)_2$.**

The voltammetric profiles illustrated in Figure 3-5 were compared with these of the different low index crystals of gold in 0.1 mol $dm^{-3}$ NaOH + 1 mmol $dm^{-3}$ $Pb(NO_3)_2$ and given in Figure 3-6.

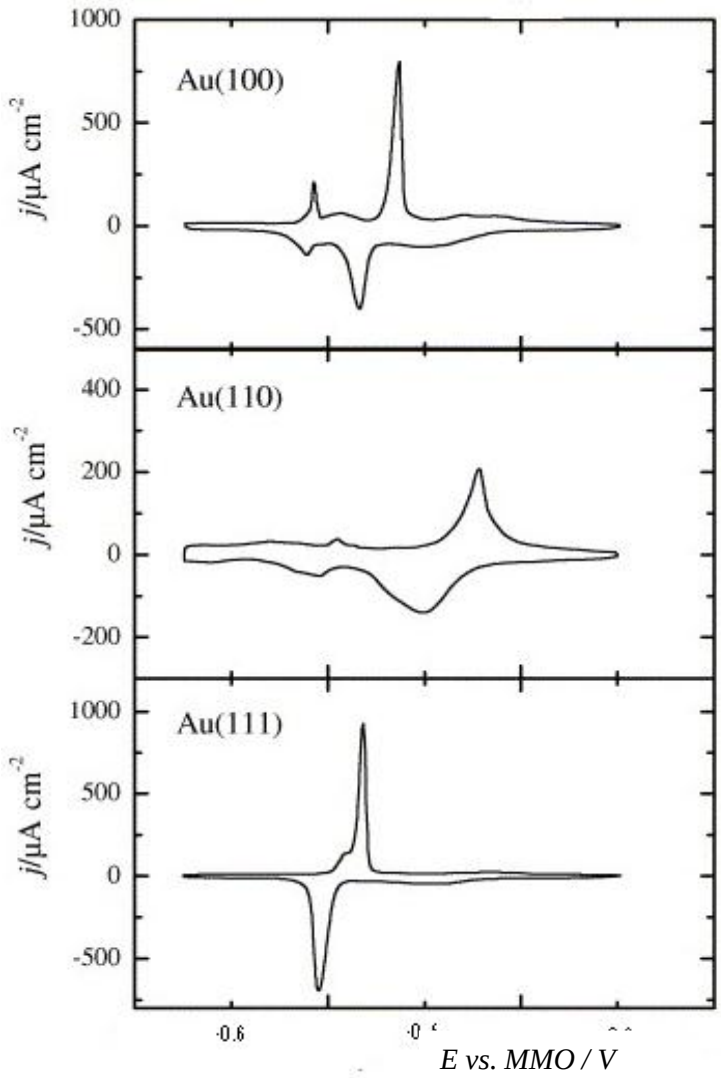


**Figure 3-6: Voltammetric profile of the Au (100), Au (110) and Au (111) electrodes[4] in 0.1 mol dm$^{-3}$ NaOH + 10$^{-3}$ mol dm$^{-3}$ Pb$(NO_3)_2$. Scan rate: 50 mV s$^{-1}$.**

As shown in Figure 3-6, in the negative sweep the peak at – 0.57 V is attributed to the single deposition of the Pb on Au (111) facets. In the reverse scan, the Pb UPD layer is dissolved resulting in a peak at -0.52 V. Similarly, the deposition peak at -0.44 V is attributed to the Au (110) facets[6]. In addition to the main peaks other humps are also observed in the voltammetric profile, which may be probably associated with the dissolution of the lead from steps and kinks in the polyoriented surface. The reduction and oxidation charges for both facets were approximately the same. Except the GC disc in all other cases the scan rate of this experiment was 20 mV s$^{-1}$. At a higher scan rate (50 mV s$^{-1}$) wavy peaks in the double layer region

were observed. It can be clearly seen in the graph that the Pb UPD on the carbon powder does not show any significant response in the voltammetric profile. Comparing Figures 3-5 and 3-6, a broader peak was observed for $Au_{3.2}$ compared to the other catalysts indicating lower crystallinity. Absence of Au (100) in the UPD profile suggests that the prepared catalysts do not have perfect octahedral structures. The ratio of Au (111) to Au (110) sites was calculated (Table 3-8).

**Table 3-8: Ratio of Au (111) to Au (110) sites.**

| Catalyst | Ratio of (111) / (110) facets |
|---|---|
| $Au_{3.2}$ | 0.25 |
| $Au_{5.4}$ | 0.24 |
| $Au_{6.0,wide}$ | 0.27 |
| $Au_{6.0,narrow}$ | 0.25 |

Table 3-8 shows that there is no significant difference in the ratio of the two different facets indicating that all the catalysts have similar particle shapes.

# 2.7 Comparison of Techniques

Data was extracted from the TEM report for comparison with XRD volume weighted data (Formfit method) by JMTC (assuming spherical particles) and the EXAFS 1$^{st}$ shell volume weighted. The results are shown in Table 3-9.

**Table 3-9: Au crystallite size comparison from TEM and XRD data.**

| Catalyst | Temperature / °C | TEM number weighted / nm | XRD volume weighted / nm | EXAFS volume weighted (1$^{st}$ shell) / nm |
|---|---|---|---|---|
| $Au_{3.2}$ | 300 | 3.2 | 3.24 | - |
| $Au_{5.4}$ | 350 | 5.4 | 5.1 | 6.1 |
| $Au_{6.0,wide}$ | 400 | 6.0 | 7.83 | - |

It can clearly be seen from the Table 3-9 that both the TEM and XRD data show an increase of size with treatment temperature. Further, there is an excellent agreement between the TEM and XRD measurements. However, the EXAFS measurement deviates slightly. This is because EXAFS gives an average over all atomic coordination within the sample. It includes all the particles smallest to largest and also the defect atoms in the crystal.

The EXAFS results show that the particles are spherical in shape. The spherical particles are visible in TEM images as well. In the UPD method the presence of (110) and (111) facets also indicates the spherical nature of the particle. For a spherical particle (e.g. $Au_{5.4}$) by considering the TEM volume weighted particle size, the theoretical surface area of the catalyst on 5 mm GC electrode (metal loading, 10 µg $cm^{-2}$) is 0.69 $cm^2$. This is very close to the experimental value obtained from the cyclic voltammetric experiment (0.717 $cm^2$). Therefore all these methods validate the spherical nature of the particles. In addition to that, the cleanness of the catalyst also proved by EXAFS by showing the absence of Au-S. This is also shown by elemental analysis results from the ICP measurements obtained from Medac, in that the S content is less than 1 wt %.

In this work, the real area of the Au catalyst was determined using the oxide stripping peak of Au in 1 mol $dm^{-3}$ $H_2SO_4$ even though Pb UPD gives an indication of the real area of Au. The reason is, the Pb is around 20 % larger in size compared to Au and it will not be able to form a complete monolayer on top of Au.

# 3. References

(1) Frenkel, A. I.; Hills, C. W.; Nuzzo, R. G. *The Journal of Physical Chemistry B* 2001, *105*, 12689.

(2) Jentys, A. *Physical Chemistry Chemical Physics* 1999, *1*, 4059.

(3) Burke, L. D.; Jean, M. M.; Patrick, F. N. *Journal of Solid State Electrochemistry* 2003, *V7*, 529.

(4) Hernandez, J.; Solla-Gullon, J.; Herrero, E. *Journal of Electroanalytical Chemistry* 2004, *574*, 185.

(5) Strbac, S.; Adzic, R. R. *Journal of Electroanalytical Chemistry* 1996, *403*, 169.

(6) Hernandez, J.; Solla-Gullon, J.; Herrero, E.; Aldaz, A.; Feliu, J. M. 2005; Vol. 109, p 12651.

# Chapter Four: Particle Size Effect

## 1. Oxygen Reduction Reaction (ORR)

### 1.1 Introduction

The electrochemical reduction of oxygen is a reaction of prime importance in many vital applications such as electrochemical energy conversion in fuel cells, metal air batteries and several industrial processes[1-4]. Most fuel cell designs utilise oxygen electro-reduction on the cathode to balance the electro-oxidation of fuel molecules on the anode. However, the efficiency of the process is often limited by the higher overpotentials observed for the oxygen reduction reaction.

Platinum based electrocatalysts are the most widely used materials for fuel cell cathodes due to their superior activity in oxygen reduction reactions (ORR)[5-7]. This unique activity of Pt is due to the metal–adsorbate electronic interactions between the oxygen bonding and antibonding orbitals and the metal *d*-orbitals, which creates a distinctive balance of bound molecular and atomic oxygen species[8]. However, due to its high cost and limited supply, Pt will ultimately not be practical for large scale fuel cell applications. Recently, several studies have been devoted to the search for suitable non Pt based electrocatalysts efficient enough to replace the more costly Pt[9-18].

Gold is considered as one of the most promising non-Pt fuel cell catalysts because it shows excellent activity towards oxygen reduction reactions[19-23]. In the past, bulk gold was considered as the most inert metal in the periodic table in accordance with chemisorption theory. This feature was attributed to the lack of interaction between the orbitals of adsorbates and the occupied *d*-orbitals of bulk gold[24]. However, nanosized gold is very active towards oxygen reduction predominantly in an alkaline media[25]. Therefore, gold based electrocatalysts are currently being investigated by researchers for ORR in both acidic and alkaline solutions[11,25-28].

The activity of gold towards the ORR has been shown to depend on the pH of the solution, structure (single crystal), as well as the surface morphology (thin film or nanoparticle).

The products of oxygen reduction depend on the pH of the solution.

In acidic solution,

$O_2 + 4H^+ + 4e^- \rightarrow 2H_2O$ **[4-1]**

if the reaction goes to completion or,

$O_2 + 2H^+ + 2e^- \rightarrow H_2O_2$ **[4-2]**

if only two electrons are transferred.

In alkaline solution,

$O_2 + 2H_2O + 4e^- \rightarrow 4OH^-$ **[4-3]**

if the reaction goes to completion or,

$O_2 + H_2O + 2e^- \rightarrow OH^- + HO_2^-$ **[4-4]**

if only two electrons are transferred.

The availability of pre-adsorbed hydroxyl anions in the case of ORR in alkaline solution makes this reaction more facile. Adzic and coworkers[30] reviewed the effect of pH on the ORR at Au (100) electrodes and found that the $2e^-$ reduction dominates for pH ≤ 3. A mixture of $2e^-$ and $4e^-$ reduction for 3< pH< 6, and the $4e^-$ reduction for pH ≥ 6.

Wei Tang *et al.*[8] proposed two mechanisms for oxygen reduction on gold.

## (1) Two step – four electron pathway reaction,

$O_2 + * \rightarrow O_{2,\,ads}$ **[4-5]**

$O_{2,\,ads} + e^- \rightarrow O_2{}^-{}_{ads}$ **[4-6]**

$O_2{}^-{}_{ads} + H_2O + e^- \rightarrow HO_2{}^-{}_{ads} + OH^-{}_{ads}$ **[4-7]**

$HO_2{}^-{}_{ads} + H_2O + 2e^- \rightarrow 3OH^-{}_{ads}$ **[4-8]**

$OH^-{}_{ads} \rightarrow OH^- + *$ **[4-9]**

## (2) Two electron pathway reaction,

$O_2 + * \rightarrow O_{2\,ads}$ **[4-10]**

$O_{2\,ads} + e^- \rightarrow O_2{}^-{}_{ads}$ **[4-11]**

$O_2{}^-{}_{ads} + H_2O + e^- \rightarrow HO_2{}^-{}_{ads} + OH^-{}_{ads}$ **[4-12]**

$OH^-{}_{ads} \rightarrow OH^- + *$ **[4-13]**

$HO_2{}^-{}_{ads} \rightarrow HO_2{}^- + *$ **[4-14]**

$HO_2{}^- \rightarrow O_2 + 2OH^-$ **[4-15]**

Where $_{ads}$ and * designate the adsorbed state and the activated state respectively. However in acidic solution the protonation of $HO_2{}^-$ is faster than in alkaline solution. Therefore the following reaction occurs and $H_2O_2$ leaves from the surface.

$HO_{2\,ads}{}^- + H^+ \rightarrow H_2O_2$ **[4-16]**

And in acidic solution the ORR follows a 2 $e^-$ pathway.

In addition to the pH of the solution, the crystallographic termination of the Au surface also plays an important role in the ORR. It has been shown that the combination of Au (100) structure and the availability of hydroxyl anions in the solution make the ORR more efficient.

Jongwon *et al.*[31] studied the ORR on Au and Pt crystallographic structures using Surface – Enhanced Raman Scattering (SERS) and Density Functional Theory (DFT) both in acidic and alkaline solutions. According to their studies, the overpotential for oxygen reduction on Pt surface in 0.1 mol $dm^{-3}$ $HClO_4$ is ~0.48 V, while that on Au (100) in 0.1 mol $dm^{-3}$ NaOH is ~0.34 V. Therefore the Au (100) surface in a basic medium has a lower overpotential for the electro-reduction of oxygen than the Pt surface in an acidic media. This higher activity of Au (100) is due to the HO–Au bond formed during ORR which facilitates the 4 $e^-$ reaction pathway.

They also compared the oxygen reduction activity on bare Au (111) and Au (100) surfaces and found that oxygen is adsorbed on the Au (111) surface on a bridged site (Figure 4-1). The O-O bond length after the oxygen adsorption is calculated to be 1.29 Å. The O-O bond length of free oxygen is 1.23 Å. On the other hand, on Au (100) the O-O bond length after the oxygen adsorption is much larger (1.37 Å) than that on Au (111). Hence the oxygen reduction is easier in Au (100) compared to Au (111).

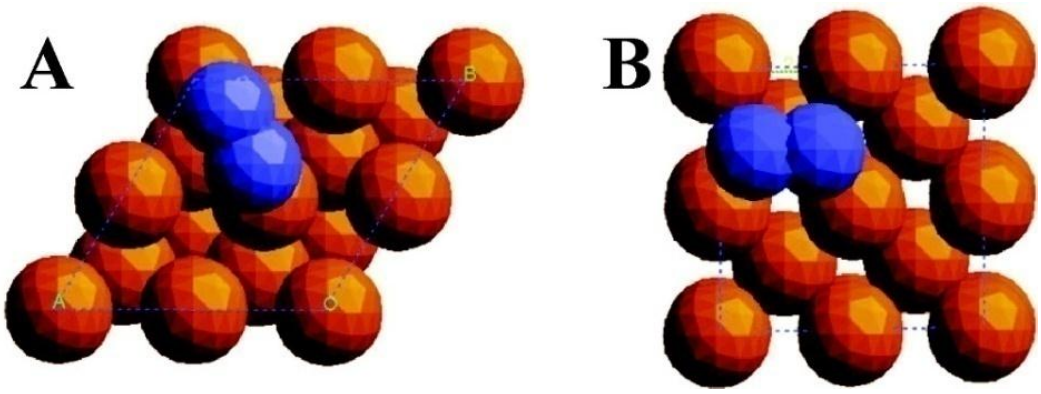


**Figure 4-1: Illustration of the oxygen adsorption on (A) Au (111) and (B) Au (100) surfaces. Au and O atoms are orange and blue, respectively[31].**

Adzic and coworkers[30] also explained the influence of $OH^-$ species and the crystal planes using molecular orbital calculations. Due to the high dissociation energy of $O_2$ (494 JK $mol^{-1}$) the activation energy for the dissociative adsorption of $O_2$ on Au is very high. However, on Au (100) facets, ORR still occurs when the surface is covered by adsorbed $OH^-$ species. The explanation is given below.

The surface of the Au (111) has three-fold symmetry of the surface atoms. According to surface calculations[30] the adsorbed species should have radii smaller than 0.216 Å and all able to fit into the cavity between the three gold atoms. However due to the larger radii of $OH^-$, (0.74 Å) only physisorption is expected. In other words, there is no overlapping of the 6*s* energy levels of Au and the $sp^3$ orbitals of $OH^-$ and there is no charge transfer. However, Au (100) has four fold symmetry and adsorbed species with a radius smaller than 0.59 Å can fit into this. Even though the radius of $OH^-$ is somewhat larger compared with the interstitial cavity, there will

still be a strong interaction (chemisorption) due to an overlap of the 6*s* energy levels of Au and the $sp^3$ orbitals of $OH^-$. Once the $OH^-$ is adsorbed on to the surface it acts as a precursor for the dissociative adsorption of oxygen during ORR. There will be an overlap between the s orbital of the H atom from $OH^-$ and the $\pi^*$ Molecular Orbital (MO) of molecular oxygen. Due to this interaction, a weakening of O-O bond can occur (Figure 4-2) hence the oxygen reduces directly via the 4 $e^-$ pathway.

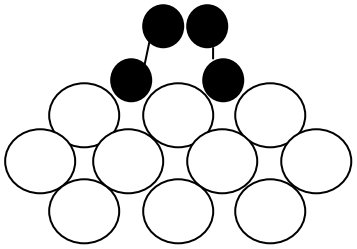

**Figure 4-2: Model of breaking of the O-O bond in the vicinity of specifically adsorbed $OH^-$ at the surface.**

In Au (111) and in acidic solutions, 2 $e^-$ from the 6*s* energy level of Au will be transferred to the $\pi^*$ MO of $O_2$ thus reducing the $O_2$ to $HO_2^-$. However, the $\sigma^*$ MO of $O_2$ is higher in energy than the 6s energy level of Au and the further reduction of $HO_2^-$ is not possible. Therefore, the reaction will stop with the 2 $e^-$ reduction[30].

The partially discharged $OH^-$ also acts as a precursor for the chemisorption of $HO_2^-$, resulting in further transfer of 2$e^-$ from the 6*s* energy level of Au to the $\sigma^*$ MO of $HO_2^-$ hence the $HO_2^-$ reduces to $H_2O$ in a 4 $e^-$ series pathway.

To achieve the maximum utilization of the metal in a working fuel cell, the metal is often dispersed as nanoparticles on a support. El- Deab and Ohsaka[11] analysed the ORR in acidic solution. They observed a significant positive shift of the reduction peak potentials and a concurrent increase of the peak current on Au nanoparticles electrodeposited on polycrystalline gold compared to on bulk gold alone. Sarapuu *et al.*[28] studied the electrochemical reduction of oxygen on a thin film Au electrode in acidic media and found that the specific activity for oxygen reduction was independent of the Au film thickness. Yagi *et al.*[32] reported that a significant

positive shift for the oxygen reduction peak and the higher current density were observed for smaller Au nanoparticles (<2 nm) deposited on boron doped diamond electrodes. However Guerin *et al.*[33] demonstrated that the catalytic activity of gold on titania support in an acidic environment reaches a maximum for a particle size of 2.5 to 3 nm. The size dependence was attributed to the strong electronic interactions between the gold and the oxide substrate. Therefore, in addition to the size of the particle the type of support also plays an important role in the electrochemical reduction of oxygen.

Carbon is more widely used as a substrate for the deposition of nanoparticles for use in electrocatalysis compared to other substrates. It has a large mesoporous area and graphitic character giving good electronic conductivity. In addition to that, carbon is cost effective compared to other substrates.

A number of reports are available for oxygen reduction on Au/C catalysts. El-Deab *et al.*[34] studied the electrodeposition of gold nanoparticles onto two different carbon substrates, Glassy Carbon (GC) and a well-oriented carbon substrate, typically Highly Oriented Pyrolytic Graphite (HOPG), and found that the gold nanoparticles on GC electrode showed higher activity for ORR. Nadezda *et al.*[26] showed that the oxygen reduction behaviour of gold nanoparticles on Multi-Walled Carbon Nanotube (GNP/ MWCNT) electrodes was greater than that of a bulk gold electrode. Zhong *et al.*[35] prepared Au and Au/Pt nanoparticles supported on carbon and studied the oxygen reduction in acid and alkaline medium. They pointed out that both the $2e^-$ and 4 $e^-$ reduction of oxygen takes place on Au/C catalysts. Erikson and coworkers[36] have studied the effect of the thickness of the Au/C catalyst layer on the kinetics of oxygen reduction in acid and alkaline solution. They found that the mechanism of oxygen reduction is not affected by the carbon support. Bron *et al.*[37] studied the oxygen reduction in acid solution on Au/C catalysts and concluded that the specific activity does not depend on the size of Au or the type of carbon support.

The aim of this work is to explore the particle size effect of Au/C catalysts towards the oxygen reduction reaction in basic medium (0.5 mol $dm^{-3}$ KOH). The alkaline

medium was chosen because of higher oxygen reduction activity of gold in basic media compared to acidic media. Four Au/C catalysts were analysed for oxygen reduction in 0.5 mol $dm^{-3}$ KOH and the results are compared with those obtained with bulk gold.

## 1.2 Experimental procedure

The catalyst powder was loaded on to the GC RDE electrode as explained in Chapter two section 3.4.2 (metal loading 10 μg $cm^{-2}$). The electrochemical cell used in this experiment was a three electrode two compartment cell. The active electrochemical areas were determined from the acid CVs as described in Chapter two section 3.4.4.2.

The electrode was transferred to a solution of 0.5 mol $dm^{-3}$ KOH. The electrolyte was purged with $N_{2\,(g)}$ whilst rotating the electrode at 1000 rpm for 15 min. The electrode rotation was then stopped and trapped bubbles, if any on the electrode surface were removed. CVs were acquired from -0.3 V to 0.6 V vs. MMO reference electrode (calibrated as -0.07 V vs. saturated calomel electrode) with a scan rate of 10 mV $s^{-1}$ whilst flowing $N_{2\,(g)}$ over the top of the electrolyte to ensure no air gets in to the electrolyte.

Before carrying out oxygen reduction measurements, the electrolyte was purged with $O_{2(g)}$ for 20 min whilst rotating the electrode at 1000 rpm. Prior to acquiring any CVs, any trapped bubbles on the electrode surface were removed. The electrode was then cleaned by running 2 CVs at 400 rpm within the potential range of 0.1 V to -0.7 V vs. MMO at a scan rate of 10 mV $s^{-1}$ , whilst flowing $O_{2(g)}$ over the top of the electrolyte to ensure complete $O_2$ saturation during the measurement. The electrode rotation was then set at 900, 1600, and 2500 rpm and 2 CVs were recorded for each rotation rate, using the previously stated conditions and the second scan was considered.

# 1.3 Results and Discussion

In this section the oxygen reduction of bulk gold and the different particle sizes of Au/C catalysts will be analysed and discussed to investigate the particle size effect for the ORR.

## 1.3.1 CVs in Alkaline media

Oxide formation and reduction during the potentiodynamic polarization was studied on both polycrystalline gold as well as the prepared catalysts. Figure 4-3 shows the CV characteristics of the bulk gold and the prepared catalysts in alkaline media.

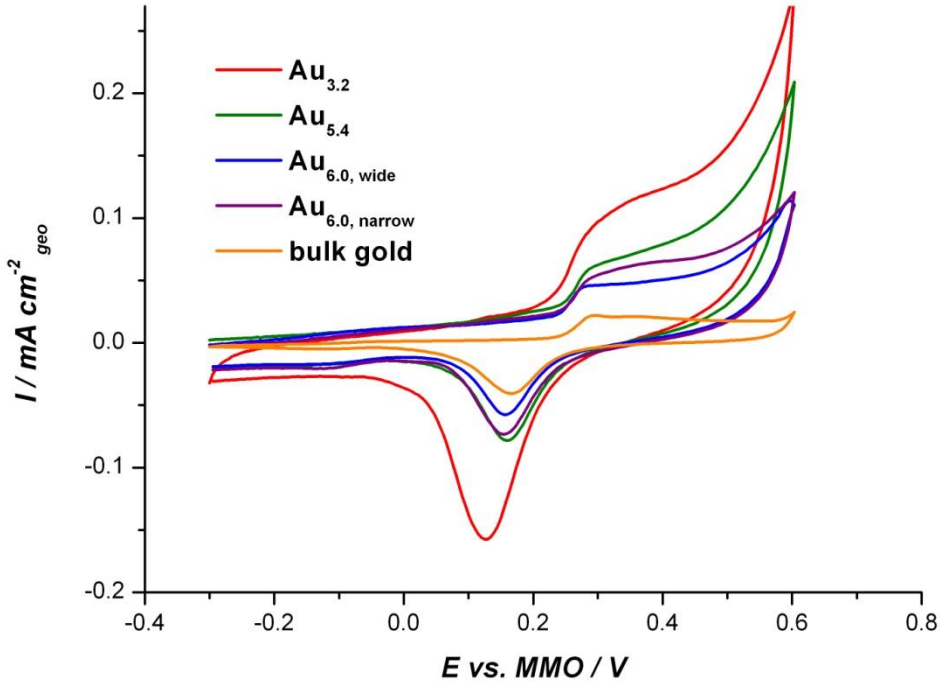


**Figure 4-3: Cyclic voltammograms for the prepared catalysts on GC disc and bulk gold in $N_2$ saturated 0.5 mol $dm^{-3}$ KOH at a scan rate 10 mV $s^{-1}$.**

Similar to the results obtained in acidic solution (explained in Chapter three section 2.5), stable voltammograms were also obtained in alkaline solution. The anodic peak

at ~0.3 V corresponds to the formation of Au oxide and the cathodic peak corresponds to its reduction at ~0.15 V. Although the CVs of the prepared catalysts are similar to that of bulk gold, larger active areas and a negative shift in the oxide reduction peak were observed for the prepared catalysts. In the anodic scan the onset of oxide formation is less positive for smaller particles compared to larger ones and the oxide reduction peak shifted negatively for the small particle catalysts compared to larger ones indicating a stronger interaction of small particles with the $OH^-$. However, the deviation is small from the behaviour of bulk gold for other catalysts.

## 1.3.2 Oxygen reduction on bulk gold

RDE polarization curves of $O_2$ reduction on the bulk gold electrode (5mm diameter) in $O_2$ saturated 0.5 mol $dm^{-3}$ KOH are shown in Figure 4-4.

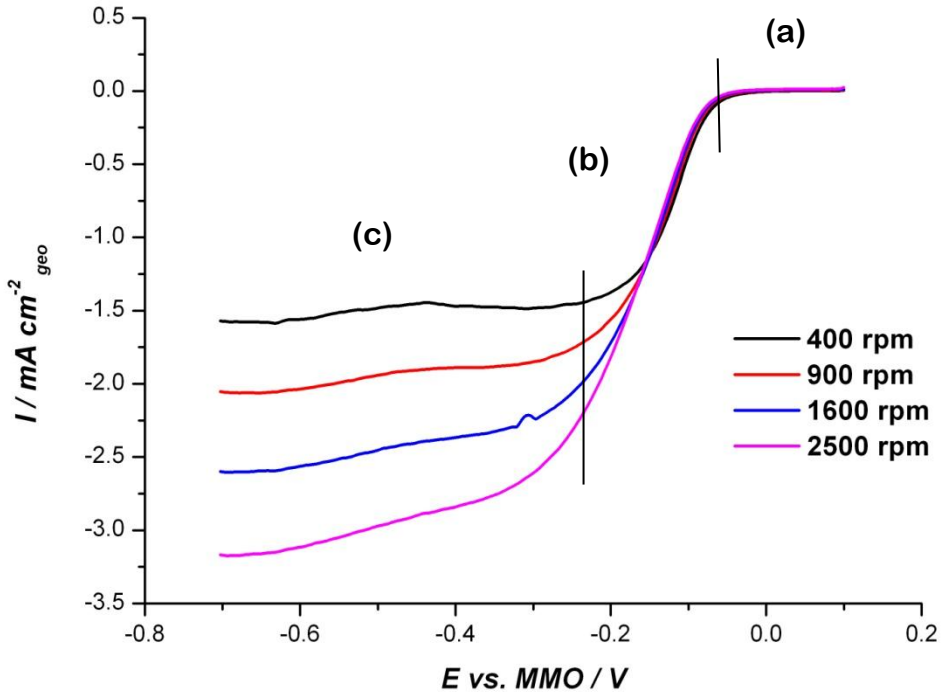


**Figure 4-4: $O_2$ reduction polarisation curves on gold disc (5 mm diameter) in $O_2$ saturated 0.5 mol $dm^{-3}$ KOH. Scan rate 10 mV $s^{-1}$ (a) activation control region; (b) mixed control region; (c) diffusion control region. Only the negative going scan is shown.**

The cathodic potential was limited to -0.7 V to avoid overlap with $H_2$ evolution. A single sigmoidal wave was observed for all rotation speeds. Three well defined regions were observed.

## (a) Activation control region (0.1 V to -0.1 V)

The activation control region is immediately negative to the equilibrium potential. In this region the surface is covered with chemisorbed $OH^-$ anions. These chemisorbed $OH^-$ anions act as precursors for the dissociative adsorption of $O_2$. The electron transfer reaction is the Rate Determining Step (RDS). The current density is totally independent of the mass transport and changing the rate of rotation of the disc has no effect on the experimental current density.

## (b) Mixed control region (-0.1 V to -0.25 V)

As the overpotential is increased, the rate of electron transfer will increase exponentially and the rate of reduction of $O_2$ will approach the rate of its transport to the surface. The electron transfer process becomes fast enough that the surface concentration begins to decrease significantly from the bulk value so that mass transport becomes an essential part of the reaction. The current density will continue to increase as the potential is taken to further negative values.

## (c) Diffusion control region (-0.25 V to -0.7 V)

The potential is further increased; the electron transfer step eventually becomes rapid compared to mass transport. The surface concentration of $O_2$ drops to zero and the current density will become fully mass transport controlled. As a consequence it becomes independent of potential but strongly dependent on mass transport, i.e. the rate of rotation of the disc electrode.

The data were analysed using the Levich Equation[28].

$$I_d = 0.201nFAD_{O_2}^{2/3}\nu^{-1/6}C^b_{O_2}\omega^{1/2} \quad \textbf{[4-17]}$$

Where $n$ is the number of electrons consumed per $O_2$ molecule, $I$ is the measured current $I_d$ is the diffusion limited current, $F$ is the Faraday constant (96 484 C $mol^{-1}$), $A$ is the geometrical area of electrode, $\omega$ is the rotation rate in rpm , $C^b_{O2}$ is the concentration of $O_2$ in the bulk ($0.8 \times 10^{-6}$ mol $cm^{-3}$), $D_{O2}$ is the diffusion coefficient of oxygen ($1.8\times10^{-5}$ $cm^2$ $s^{-1}$) and the $\nu$ is the kinematic viscosity of the solution (0.01 $cm^2$ $s^{-1}$)[38,39].

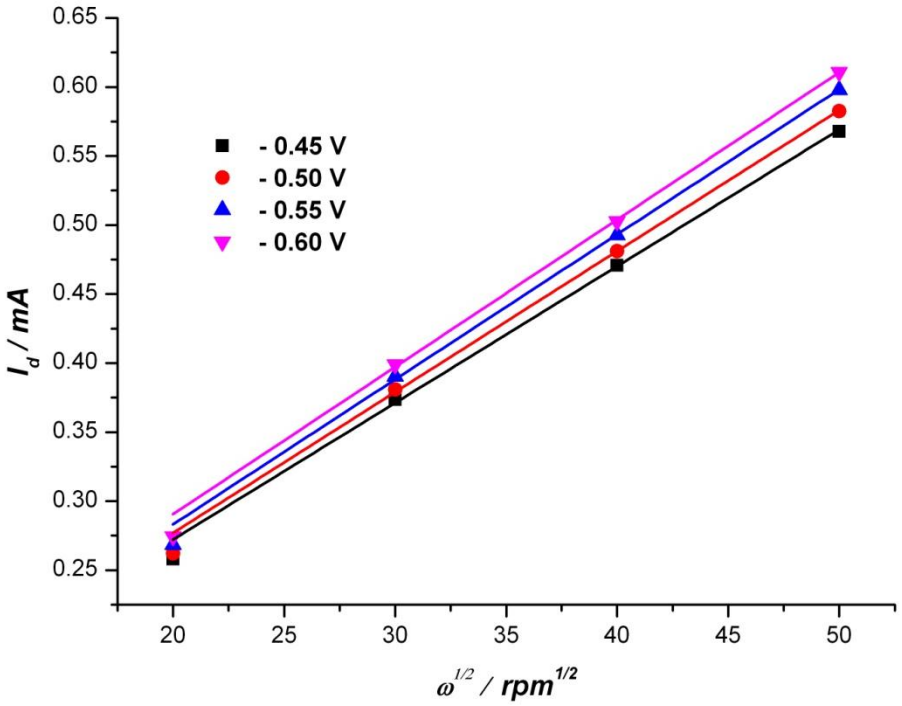


**Figure 4-5: Levich plots for oxygen reduction on the bulk gold electrode in $O_2$ saturated 0.5 mol $dm^{-3}$ KOH at different limiting potentials.**

Figure 4-5 shows the Levich plots obtained from the RDE data represented in Figure 4-4. The points at 400 rpm clearly do not fall on the line. The reason may be that at the lower rotation speed there is not much $O_2$ flow towards the electrode and hence they do not obey the Levich relationship. In addition to that, it is also clearly seen from the graph that the intercepts are potential dependent. The Levich parameters obtained from this plot are tabulated in Table 4-1.

**Table 4-1: Levich parameters determined from bulk gold at different limiting potentials**

| Limiting potential / V | Gradient / $10^{-5}$ A $rpm^{-1/2}$ | Number of electrons involved (*n*) |
|---|---|---|
| -0.45 | 1.00 ± 0.04 | 2.3 |
| -0.50 | 1.02 ± 0.04 | 2.4 |
| -0.55 | 1.05 ± 0.04 | 2.5 |
| -0.60 | 1.06 ± 0.04 | 2.5 |

The number of electrons was determined from the gradient. The gradients of these lines progressively decreased as the potential shifted to a more negative value, indicating that the *n* value increased at more negative potentials. In other words, at more negative potentials further reduction of $HO_2^-$ occurs.

A value of $4 \geq n \geq 2$ indicates a mixture of the $2e^-$ and $4e^-$ reduction. Shao and Adzic[29] stated that on bulk gold 2 step $4e^-$ reduction occurs and they explained using the SERS that in the diffusion controlled region the coverage of $HO_2^-$ decreases due to the weaker interaction of the Au surface and the $HO_2^-$, even though more $HO_2^-$ anions are produced. Further studies by Strabac *et al.*[40] on different crystalline facets of bulk gold in alkaline media using the rotating ring-disc method shows a 4 e- reduction on Au (100) facets compared to other ones. The UPD measurements from this work show that the bulk gold has Au (111) and Au (110) facets and there is an insignificant amount of Au (100) facet detected by the above techniques. Therefore this may be the reason that the values are less than 4.

A Tafel plot can be constructed and the specific activity (SA) at a given potential calculated using the Equation below,

$$SA = \frac{I_K}{A_r} \qquad \textbf{[4-18]}$$

Where, $I_K$ is the kinetic current at a given potential and $A_r$ is the real surface area of the gold. The $A_r$ was determined using a value of 400 μC $cm^{-2}$ for the reduction of the surface oxide monolayer.

The relationship between the total current, kinetic current and the diffusion limiting current for the oxygen reduction is given by,

$$SA = \frac{I_d I}{(I_d - I)A_r} \qquad \textbf{[4-19]}$$

Figure 4-6 represents the potential dependence of the specific activity.

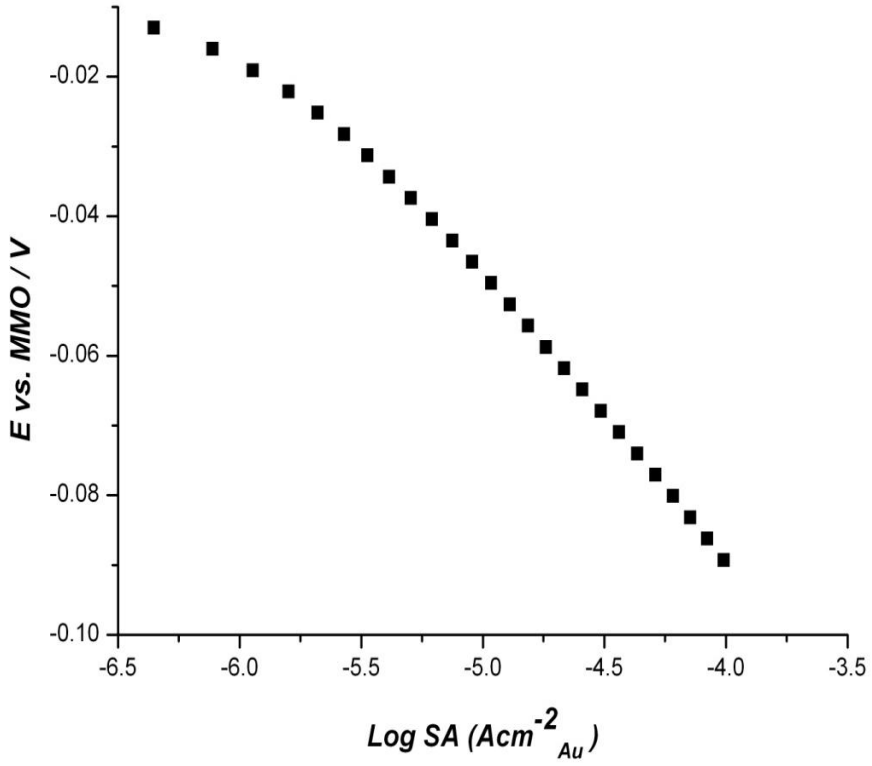


**Figure 4-6: Tafel plot corresponding to the data obtained at 900 rpm in Figure 4-4.**

The SA value thus obtained for bulk gold at -0.05 V (a potential in the activation control region) was 0.02 mA $cm^{-2}_{Au}$. Sarapuu *et al.*[41] reported the SA of bulk gold in 0.1 mol $dm^{-3}$ KOH at -0.15 V vs. SCE (-0.08 V vs. MMO) as 0.19 mA $cm^{-2}_{Au}$. At that potential the calculated SA value of our disc is 0.1 mA $cm^{-2}$. This value is around 2 times higher than the value calculated here. The reason may be due to the lower concentration of KOH used by Sarapuu *et al.*

## 1.3.3 Oxygen reduction on Au/C catalysts

Figure 4-7 shows representative current–potential curves for the ORR at the Au/C catalysts on the RDE in $O_2$-saturated 0.5 mol $dm^{-3}$ KOH at several rotation rates.

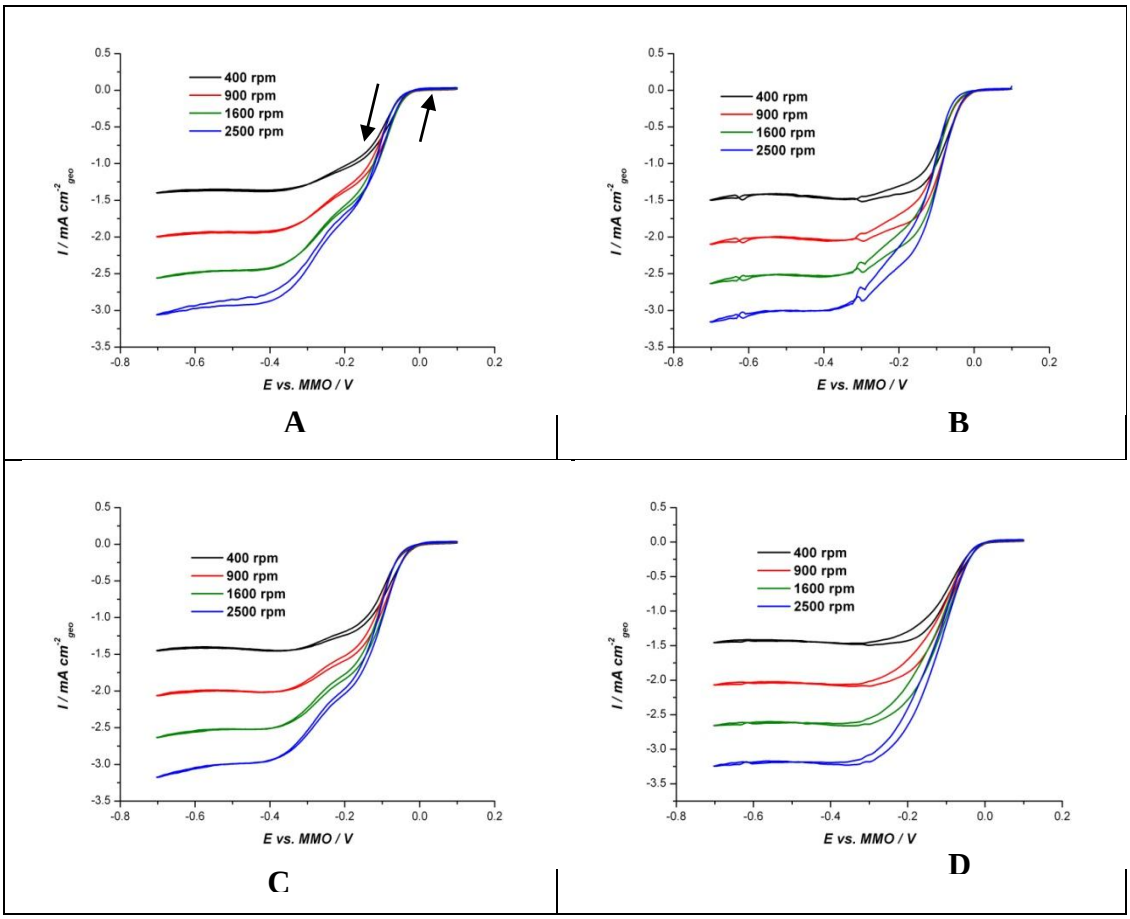


**Figure 4-7: Oxygen reduction rotating disc voltammograms of the prepared Au/C catalysts (A) $Au_{3.2}$, (B) $Au_{5.4}$, (C) $Au_{6.0,wide}$ and (D) $Au_{6.0,narrow}$ on GC electrode (5 mm diameter) in $O_2$ saturated 0.5 mol $dm^{-3}$ KOH. Scan rate of 10 mV $s^{-1}$.**

Except for the $Au_{6.0,\ narrow}$ all the above catalysts show two sigmoidal $O_2$ reduction curves, and for all the catalysts a well-defined plateau was observed in the diffusion controlled region.

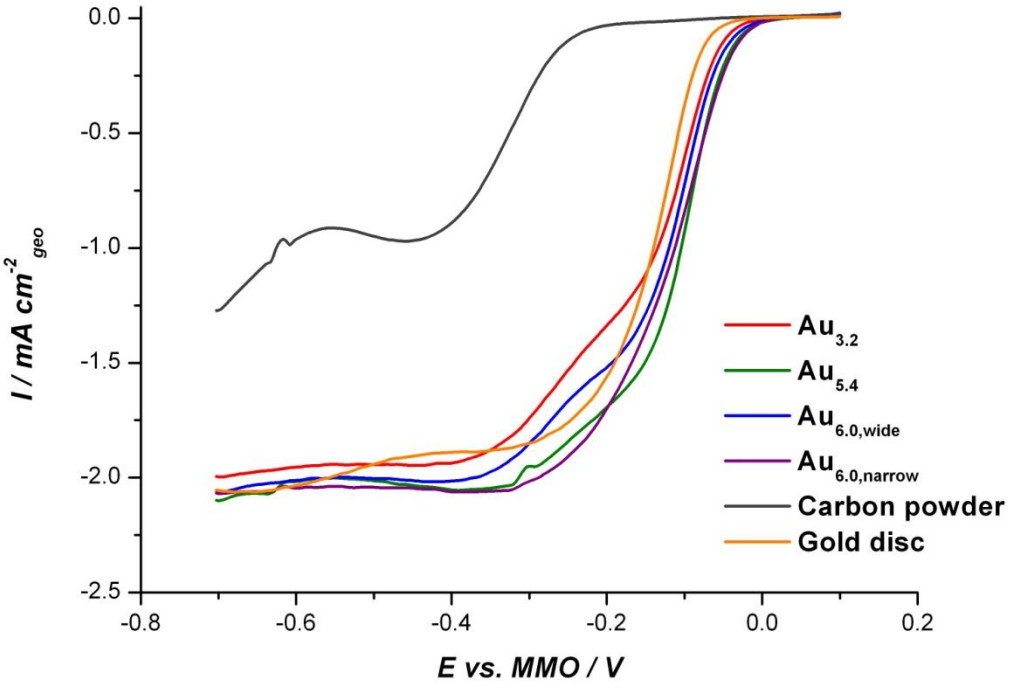


**Figure 4-8: ORR on GC disc, gold disc and prepared catalysts in oxygen saturated 0.5 mol $dm^{-3}$ KOH at 900 rpm. Scan rate 10 mV $s^{-1}$. Only the negative going scans were selected. (Geometric area 0.196 $cm^2$).**

From the Figure 4-8 it can be seen that the limiting current density based on the geometric area for oxygen reduction is independent of the nature of the Au.

Since the carbon support of the electrode also exhibits electrocatalytic activity for oxygen reduction in basic media, the ORR at a carbon powder modified RDE was also compared with all the catalysts prepared. The onset potential of oxygen reduction on the carbon powder is around -0.2 V. At this potential, all the prepared catalysts have reached their mass transport control region. Therefore, the influence of the carbon support on the recorded activity in the presence of these catalysts can be considered negligible.

The activity in the kinetic controlled region cannot be compared by using the previous Figure due to the different amount of Au on the GC disc. Therefore to compare the size dependent activity, the current was divided by the real area of Au to give current density and is shown in Figure 4-9.

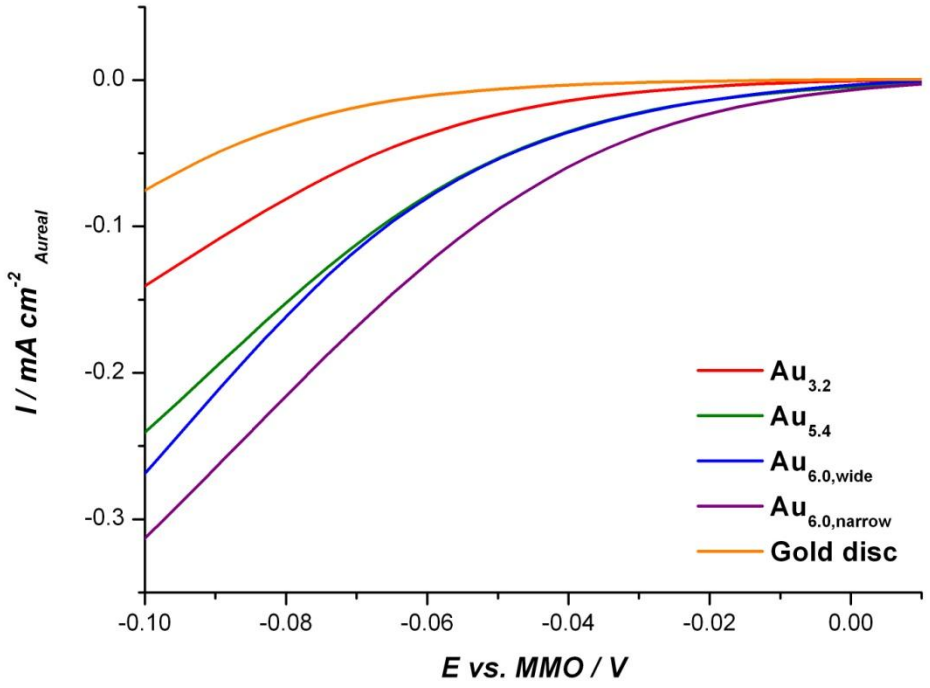


**Figure 4-9: ORR on prepared catalysts in oxygen saturated 0.5 mol $dm^{-3}$ KOH at 900 rpm. Scan rate 10 mV $s^{-1}$. Only the negative going scans around the activation controlled region were selected. The current was normalized by the Au real area.**

The onset potential for the oxygen reduction is shifted towards a more negative potential region with decreasing particle size, but all the carbon supported catalysts were more active than the bulk Au.

Figure 4-10 shows the Levich plots obtained for the bulk gold and the prepared catalysts from the RDE data presented in Figure 4-7.

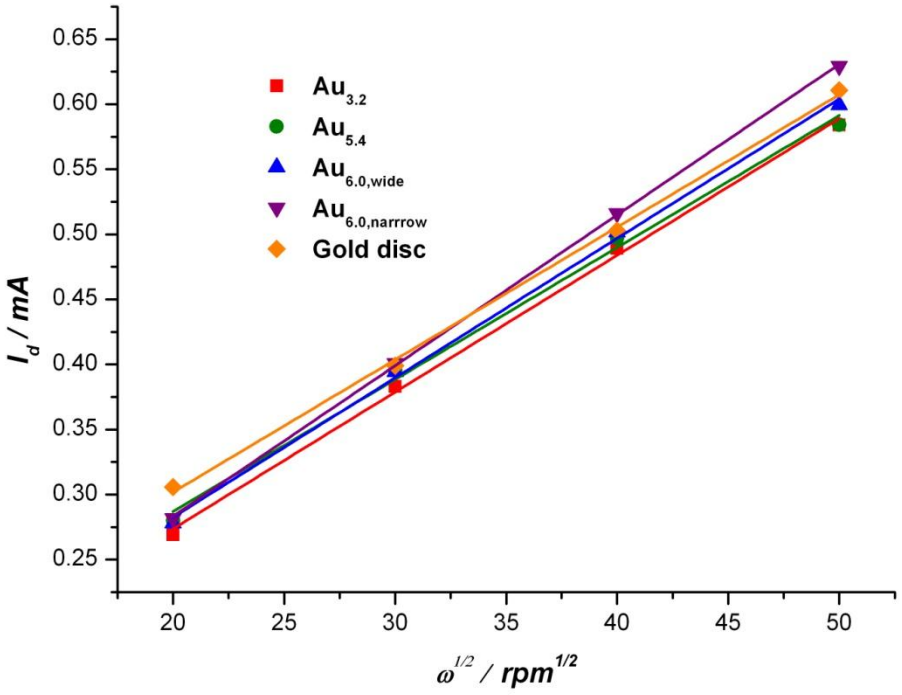


**Figure 4-10: Levich plots for oxygen reduction on bulk gold and prepared catalysts in $O_2$ saturated 0.5 mol $dm^{-3}$ KOH at -0.6 V limiting potential.**

All the catalysts obey the Levich Equation. The plot parameters for all the prepared catalysts and the bulk gold are tabulated in Table 4-2. The number of electrons transferred for all the prepared catalysts and bulk gold are almost similar indicating that the mechanism is unchanged.

**Table 4-2: Levich plot parameters determined from the catalysts in oxygen saturated 0.5 mol $dm^{-3}$ KOH (the currents at -0.6 V were used).**

| Catalyst | Gradient / $10^{-5}$ A $rpm^{-½}$ | Number of electrons (*n*) |
|---|---|---|
| $Au_{3.2}$ | 1.05 ± 0.03 | 2.5 |
| $Au_{5.4}$ | 1.01 ± 0.05 | 2.4 |
| $Au_{6.0,\ wide}$ | 1.07 ± 0.03 | 2.5 |
| $Au_{6.0,\ narrow}$ | 1.16 ± 0.02 | 2.6 |
| Bulk gold | 1.06 ± 0.04 | 2.5 |

It is apparent from the results presented in Table 4-2, that there is no significant difference in the number of electrons between the prepared catalysts as well as the bulk gold. That the *n* values are less than four shows that the reduction of oxygen is

not a complete four electron reduction reaction. This is attributed to the absence of Au (100) facets in the prepared catalysts.

Figure 4-11 shows the Tafel plots corresponding to the specific activity of each of the prepared catalysts and the bulk gold.

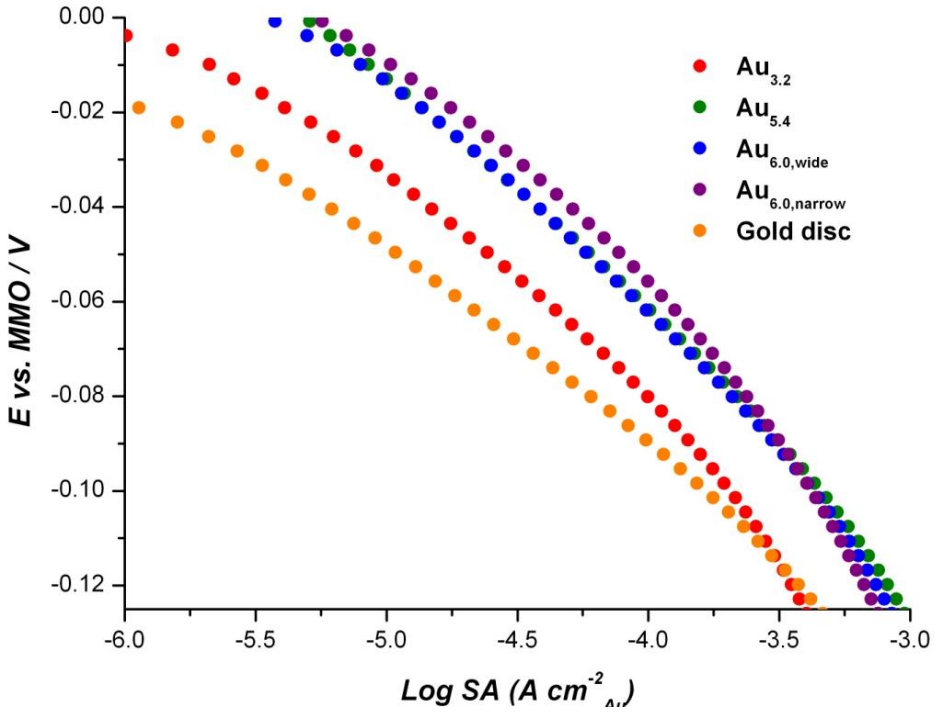


**Figure 4-11: Tafel plot for gold disc and the prepared catalysts in oxygen saturated 0.5 mol dm$^{-3}$ KOH at 900 rpm.**

From the Tafel plot, the SA values of the prepared catalysts and the bulk gold were determined at -0.05 V vs. MMO and tabulated in Table 4-3.

**Table 4-3: Kinetic parameters of oxygen reduction on Au/C catalysts in 0.5 mol dm$^{-3}$ KOH at rotation speed 900 rpm.**

| Catalyst | SA at -0.05 V / mA cm$^{-2}$ $_{Au}$ |
|---|---|
| $Au_{3.2}$ | 0.03 |
| $Au_{5.4}$ | 0.07 |
| $Au_{6.0,wide}$ | 0.07 |
| $Au_{6.0,narrow}$ | 0.09 |
| Bulk gold | 0.02 |

According to Table 4-3, the specific activity of the bulk gold is very much smaller than that of all the prepared catalysts. In addition to that, the specific activity increases with the size of Au. There is a dramatic change in SA value between the $Au_{3.2}$ and $Au_{5.4}$. The values are similar for $Au_{5.4}$ and $Au_{6.0,\ wide}$. However, $Au_{6.0,\ narrow}$ has higher SA value compared to $Au_{6.0,\ wide}$.

There are various reports in the literature on SA value of the Au catalysts[21,24,36,42]. Most of the work in the literature is based on the Au film thickness, however there are some reports describing the SA values of different sizes of Au catalysts [8,24]. The activity of the Au/C catalyst used in this work is much higher than that of the nanoparticle (3 and 7 nm) prepared by reverse micelle encapsulation by Tang *et al.*[8] In that study, a SA value of 3.5 mA $cm^{-2}$ was obtained at -0.6 V vs. Ag / AgCl for a 3 nm particle. However, the $Au_{3.2}$ catalyst reached that SA value at a much more positive potential (-0.36 V vs. Ag / AgCl). This indicates the superior electrocatalytic properties of the Au/C catalysts used in this work.

Greeley *et al.*[43] explained that defects on smaller catalytic particles are less active for the oxygen reduction than a well-defined low index crystal planes. When the Au size becomes smaller the concentration of defects increases resulting in a decrease in the average particle activity.

There are a couple of reports on oxygen reduction on Au surfaces in alkaline media related to the size effect of Au. Sarapuu *et al.*[42] studied oxygen reduction on nanostructured gold electrodes with a thickness of 0.25–20 nm in both acidic and alkaline media using the RDE technique. They predicted that the higher activity on larger particles may be linked to the relative enrichment of Au (100) facets compared to smaller ones. However the above conclusion is in contradiction with the results obtained by Tang *et al.*[8] who studied the oxygen reduction on two different sizes (3 & 7 nm) of Au/C catalysts using RDE. They observed a higher kinetic current density for a 3 nm particle compared to a 7 nm one. However our largest particle size is 6 nm. Therefore, there may be some activity reduction beyond 6 nm.

The size effect on the oxygen reduction activity is still unclear; however, it may be explained by using the CV features of the carbon supported Au catalysts. The effect of hydroxyl coverage on gold influences the rate of oxygen reduction. As explained in Figure 4-3, the smaller particles bind oxygen too strongly (irreversible adsorption) compared to larger ones, as a result the oxygen reduction activity is limited by the removal of the adsorbed O and OH species. Even though the hydroxyl ion enhances the oxygen reduction kinetics, when these anions are adsorbed on to the Au surface very strongly, they block the active sites required for the adsorption of oxygen and the splitting of the O-O bond. Therefore, this increase in oxophilicity for smaller particles leads to a decrease in specific activity for the ORR.

# 2. CO Oxidation Reaction

## 2.1 Introduction

The study of catalytic oxidation of CO has been widely investigated in industrial applications such as fuel cells, purification of air in gas products and conversion of CO in automobile exhaust systems[44,45]. Most of the reported studies on the CO oxidation reaction have focused on Pt group metals[46-48]. Haruta *et al.*[49] have shown extraordinarily high catalytic activity towards the gas phase CO oxidation at gold catalysts supported on metal oxides. Following this discovery, gold has been increasingly studied by researchers[50-52]. Due to the lack of empty *d*-orbital there is little or no adsorption of CO on the gold surface. Spectroscopic studies also proved that there was only a weak interaction of CO with polycrystalline gold surfaces[53,54]. However, nanosized gold is capable of oxidizing solution phase CO[50,51].

Several authors have reported that the gold nanoparticles with a diameter of less than 10 nm show extraordinary catalytic activity towards CO oxidation[55-58]. Hayden *et al.*[51] used electrochemical studies to compare CO oxidation on Au nanoparticles (mean diameter < 6.5 nm) supported on carbon with those supported on titania, and

compared these to oxidation at polycrystalline Au. They concluded that the activity was strongly particle size dependent and that larger particles are more active with a steep decrease in activity being observed below 3 nm. However, this observation is in contradiction to that of Dongsheng Geng and coworkers[50], who also observed a size dependent activity of Au nanoparticle towards the CO oxidation in alkaline medium and found higher activity for smaller particles. They assumed the higher activity on smaller particles was due to their higher concentration of low-coordinated surface metal atoms. However the particle sizes analysed were larger (2-41 nm) compared to those reported by Hayden *et al*.

The support on which the gold nanoparticles are dispersed is also another important factor in determining the activity of CO oxidation. It has been shown that even for similar particle sizes the activity of gold nanoparticles differs with different substrates[57]. Metal oxide supports have been shown to promote the catalysis of CO oxidation[57,59]. Particularly, gold nanoparticles supported on titania exhibited higher activity compared to other metal oxides. A number of explanations were put forward by Hayden *et al*. to demonstrate the superior activity of the Au/ $TiO_2$ towards the CO oxidation[51].

1. The titania support stabilizes the low–coordinated Au atoms and hence increases the CO coverage. As a result the CO oxidation increases.
2. The titania induces electronic modifications of the gold, which enhances the catalytic activity of CO oxidation.
3. An increase in spill- over of oxygen from the support at the particle-support interface is observed when titania is used as a support.

However, activity measurements on various Au catalysts with different oxide supports by Markus *et al*.[60] confirmed that the Au catalysts supported on reducible transition metal oxides such as $Fe_2O_3$ exhibit considerably enhanced activity for CO oxidation, which is attributed to their ability to provide reactive oxygen.

A number of studies have shown that irreversible adsorption of CO takes place on gold electrodes in alkaline solutions[61,62]. In acid solution, CO does not remain chemisorbed on the gold surface in the absence of CO in solution phase[63,64]. In 1985,

Kita and coworkers[62] investigated CO electro-oxidation on gold in alkaline media and showed that it takes place at an overpotential ~0.5 V lower than on Pt. Thus, the higher catalytic activity in alkaline media seems to be related to the apparently stronger CO chemisorption. Paramaconi and coworkers[52] also agreed with the higher activity in alkaline solution and proposed a mechanism using a DFT calculation. They claimed that CO oxidation on gold takes place through a self-promotion mechanism in which the presence of CO on the gold surface enhances the adsorption of its own oxidant through a local gold-mediated donation-back donation mechanism driven by a change in the local electrostatics. In other words $OH^-$ and CO mutually enhances each other's adsorption when bonded to nearest neighbour (*nn*) binding sites on the gold surface.

$$CO + * \leftrightarrow CO_{ads} \quad \textbf{[4-20]}$$

$$CO_{ads} + OH^- + *nn \leftrightarrow CO_{ads} + OH^-_{ads,nn} \quad \textbf{[4-21]}$$

$$CO_{ads} + OH^-_{ads,nn} \rightarrow COOH_{ads} + * + e^- \qquad rds \quad \textbf{[4-22]}$$

$$COOH_{ads} \leftrightarrow COO^-_{ads} + H^+ \quad \textbf{[4-23]}$$

$$COO^-_{ads} \rightarrow CO_2 + * + e^- \quad \textbf{[4-24]}$$

The $CO_2$ produced quickly forms carbonate in alkaline media. In acidic media, reaction [4-22] would be replaced by:

$$CO_{ads} + H_2O + *_{nn} \leftrightarrow CO_{ads} + OH^-_{ads,nn} + H^+ \quad \textbf{[4-25]}$$

Accordingly, the enrichment of the adsorption of oxidative species by CO adsorption will significantly depend on the CO adsorption energy itself. A stronger interaction of CO species with the gold surface will permit a higher stabilization of co-adsorbed oxidative species. In turn, the consequential increase of the coverage of oxidative species will lead to further strengthening of CO adsorption. Therefore, the enhanced

catalytic activity of gold electrodes in alkaline solutions may be explained by the larger adsorption energy of CO species under these conditions[52].

In addition to the factors described above, the oxidation of CO also depends on the crystal face when gold single crystals are used. Studies by Berislav *et al.*[65] using a combination of electrochemical and infrared reflection absorption spectroscopy measurements for CO electro-oxidation on gold single crystal surfaces proved that the oxidation is highly sensitive to the structure. According to their observation, the activity decreases in the order Au (110) ≥ Au (100) > Au (111). Gallagher and coworkers[66] have performed in situ surface X-ray scattering and cyclic voltammetry measurements to determine the effect of surface atomic structure on CO oxidation in alkaline medium. They also found the CO oxidation to be structure sensitive with the activity decreasing in the same order. They suggested that this activity is attributed to the availability of low coordination adsorption sites which depends on the atomic geometry of the particular Au (*hkl*) low index surface.

The aim of this work is to investigate the particle size effect of Au/C catalysts towards the CO oxidation reaction in alkaline medium. Four Au/C catalysts were analysed for CO oxidation in 0.5 mol $dm^{-3}$ KOH and the results are compared with those obtained using bulk gold.

# 2.2 Experimental

The electrode was prepared using the same method explained in Chapter two section 3.4.2 (metal loading 10 μg $cm^{-2}$). This was transferred to a solution of 0.5 mol $dm^{-3}$ KOH and was purged with $N_{2(g)}$ whilst rotating the electrode at 1000 rpm for 15 min. The electrode rotation was then stopped and trapped bubbles, if any on the electrode surface were removed. CVs were acquired from -0.3 V to 0.6 V vs. MMO reference electrode (calibrated as -0.07 V vs. saturated calomel electrode) with a scan rate of 20 mV $s^{-1}$ whilst flowing $N_{2\,(g)}$ over the top of the electrolyte to ensure no air gets in to the electrolyte.

Before carrying out CO oxidation measurements, the electrolyte was purged with $CO_{(g)}$ for 20 min whilst rotating the electrode at 1000 rpm. Prior to acquiring any CVs, any trapped bubbles on the electrode surface were removed. The electrode was then cleaned by running 2 CVs at 400 rpm within the potential range of -1.2 V to 0.6 V vs. MMO at a scan rate of 20 mV $s^{-1}$, whilst flowing $CO_{(g)}$ over the top of the electrolyte to ensure complete CO saturation during the measurement. The electrode rotation was then set at 900, 1600, and 2500 rpm and 2 CVs were recorded for each rotation rate, using the previously stated conditions and the second scan was considered.

# 2.3 Results and Discussion

## 2.3.1 CO oxidation on bulk gold

The RDE voltammetry curves of CO oxidation on bulk gold electrode (5mm diameter) in CO saturated 0.5 mol $dm^{-3}$ KOH are shown in Figure 4-12.

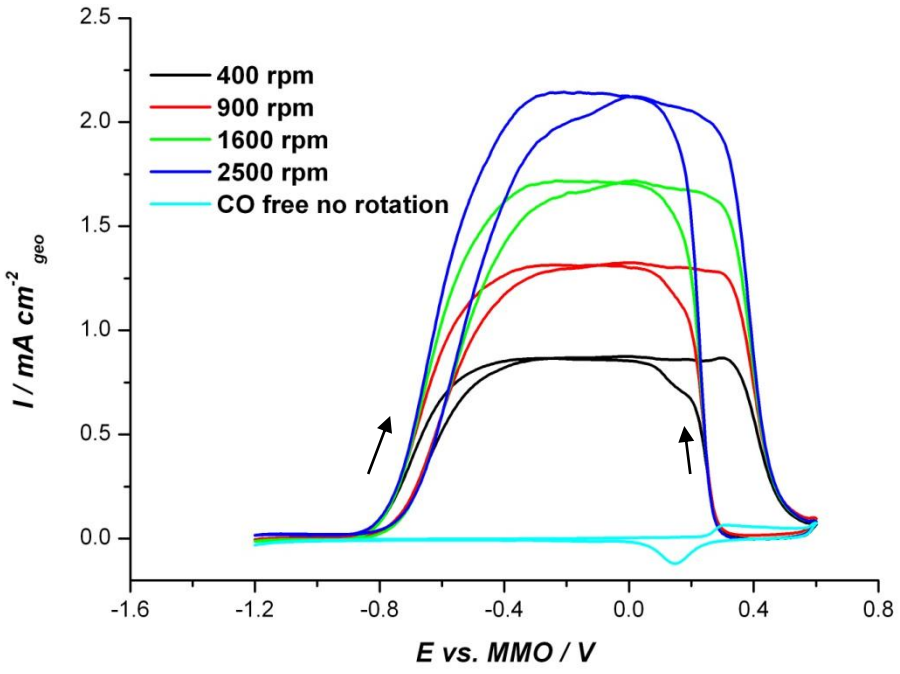


**Figure 4-12: CO oxidation curves on gold disc (5 mm diameter) in CO saturated 0.5 mol $dm^{-3}$ KOH. Scan rate 20 mV $s^{-1}$. The arrows indicate the directions.**

The oxidation currents of dissolved CO on the gold electrode in 0.5 mol $dm^{-3}$ KOH exhibit pure diffusion control behaviour as shown in Figure 4-12. The CO oxidation starts at ~ -0.9 V vs. MMO and reaches a maximum current at ~ -0.3 V. In the potential range between -0.3 V and 0.3 V the process is diffusion controlled. During the positive scan the formation of gold oxide at ~ 0.3 V inhibits CO oxidation. In the reverse scan, at ~0.45 V the AuO is reduced to Au, and below ~ 0.45 V, the CO oxidation current returns. There is a hysteresis between the forward scan and the backward scan.

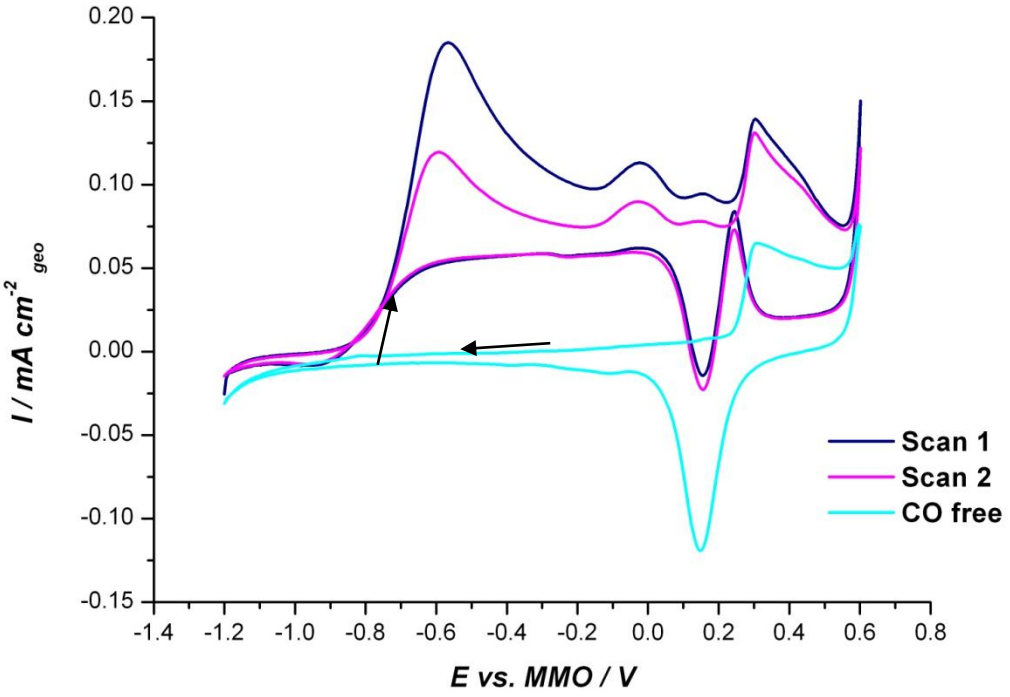


**Figure 4-13: CO oxidation curves on gold disc (5 mm diameter) in CO saturated 0.5 mol $dm^{-3}$ KOH no rotation. Scan rate 20 mV $s^{-1}$. The arrows indicate the directions.**

Figure 4-13 shows a CV for a stationary polycrystalline Au disc in CO saturated and CO free 0.5 mol $dm^{-3}$ KOH solution. The response at the stationary electrode appears to be significantly different from that at the rotated electrodes because, in the absence of forced convection, the ratio of the current for CO oxidation to AuO formation is very much reduced[51], and a peak is prominent at ~ -0.7 V. In addition, two more peaks are also observed at ~ -0.1 V and 0.1 V respectively. They may be due to OH adsorbed at different sites on Au. The current at ~0.4 V is mainly attributed to oxidation of gold. Oxygen evolution is observed beyond 0.6 V.

Reactivation of CO oxidation is again seen on the reverse scan at ~ 0.3 V. At this potential the oxide reduction has only just started. This is strong evidence that a high rate of CO oxidation can be achieved with only a small number of active sites on the gold surface.

## 2.3.2 CO oxidation on Au/C catalysts

Figure 4-14 shows current–potential curves for the CO oxidation at the Au/C catalysts on the RDE in CO-saturated 0.5 mol $dm^{-3}$ KOH at several rotation rates.

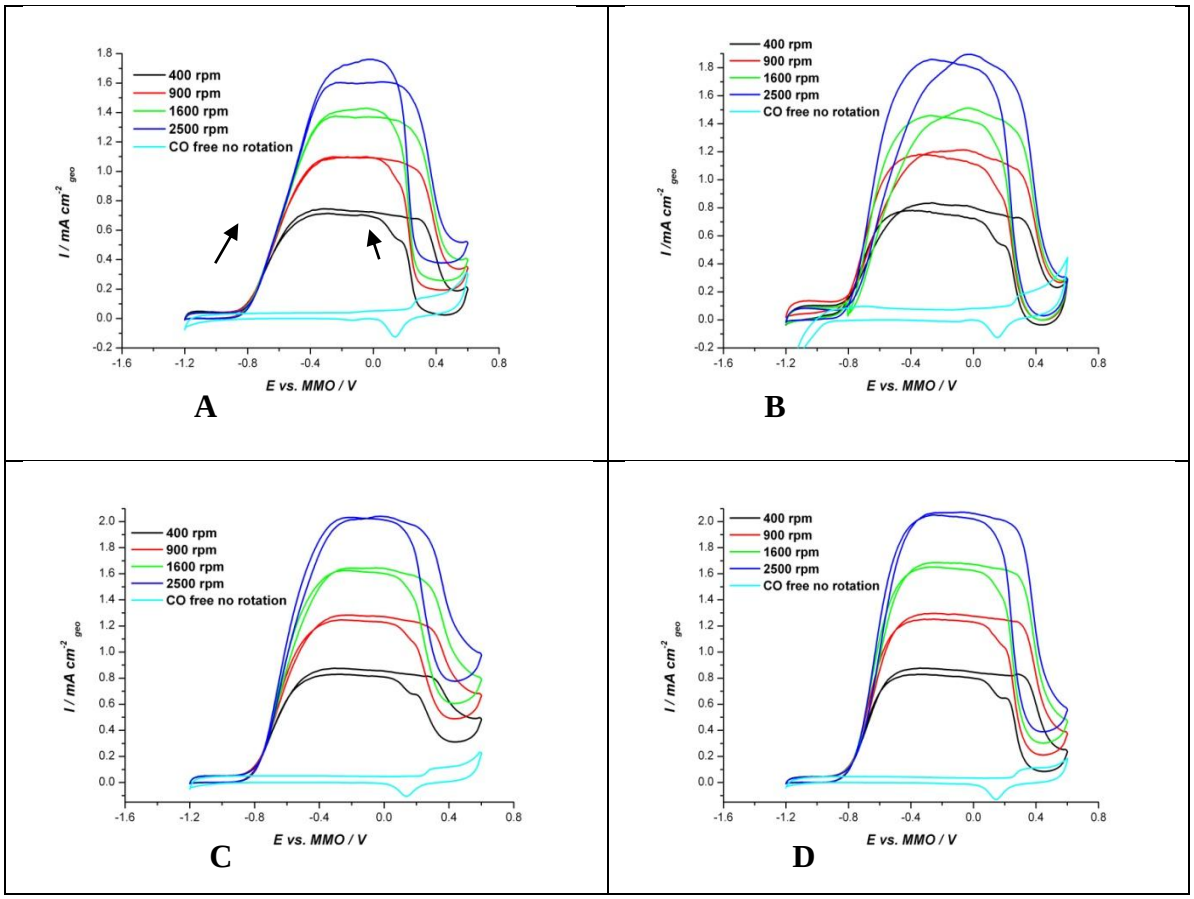


**Figure 4-14 : CO oxidation rotating disc voltammogram of the prepared Au/C catalysts (A) $Au_{3.2}$, (B) $Au_{5.4}$, (C) $Au_{6.0,wide}$ and (D) $Au_{6.0,narrow}$ on GC electrode (5 mm diameter) in CO saturated 0.5 mol $dm^{-3}$ KOH. Scan rate 20 mV $s^{-1}$. Arrows indicate the direction.**

The CV features observed in Figure 4-14 are similar to those observed for the bulk gold. However, except for $Au_{5.4}$, the anodic scan does not terminating at zero current and this deviation increases with increasing rotation rate.

The CO oxidation curves of all the prepared catalysts, bulk gold and the carbon support were compared at 900 rpm and shown in Figure 4-15.

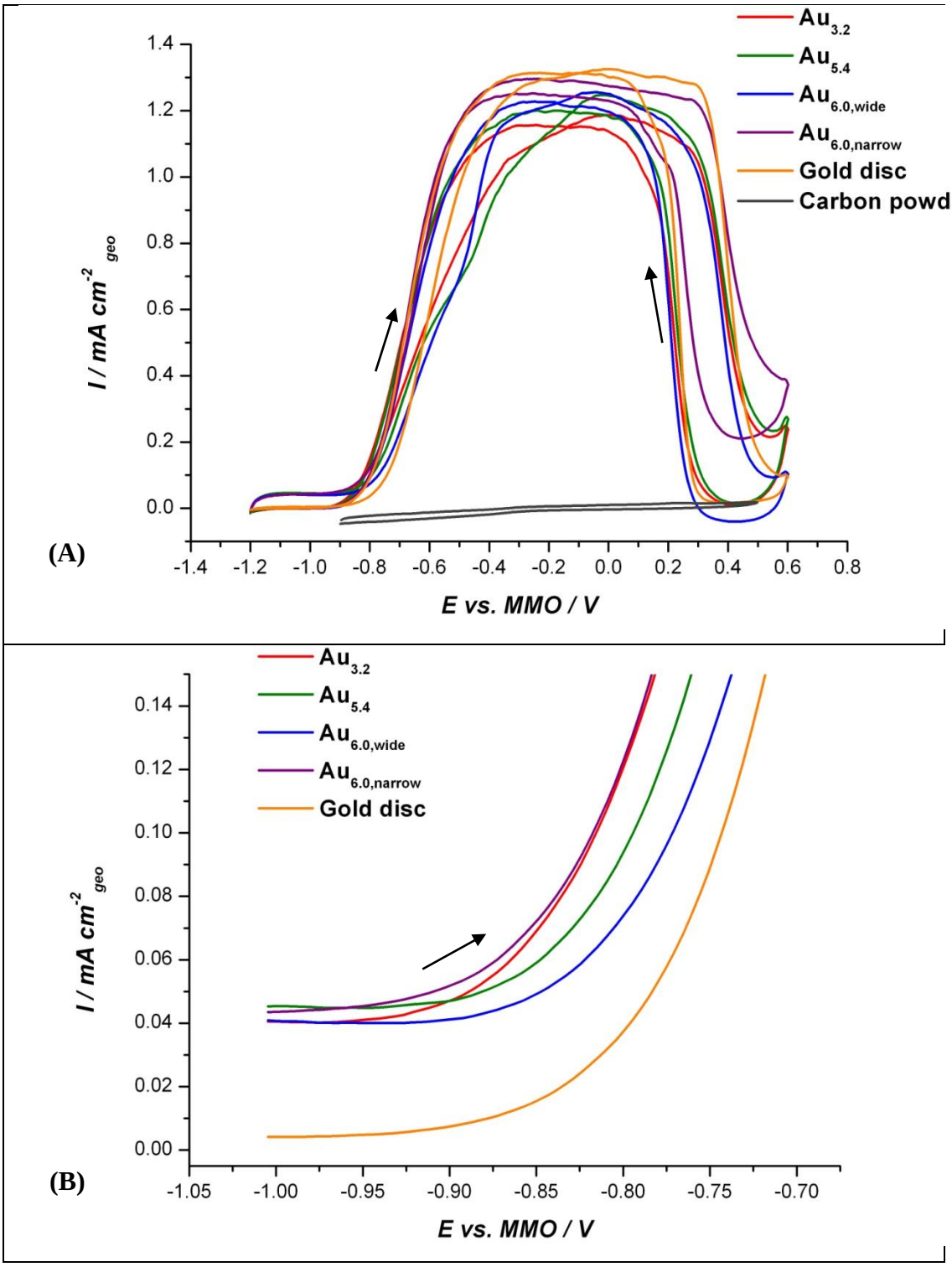


**Figure 4-15 :(A) CO oxidation on gold disc and prepared catalysts in CO saturated 0.5 mol $dm^{-3}$ KOH at rotation rate 900 rpm. Scan rate 20 mV $s^{-1}$ (Geometric area 0.196 $cm^{-2}$). Arrows indicate the direction. (B) Shows the magnification near the onset potential.**

There is no significant amount of current observed for the GC disc indicating the inactivity of carbon powder towards CO oxidation. As expected, there is very little difference observed in the diffusion controlled currents (at -0.3 V) as a function of the catalyst as shown in Figure 4-15. This is expected as such current depends on the geometric area of the disc. The small variations observed may reflect differences in the coverage of the disc by the carbon supported catalyst, which effectively results in small variations in the geometric area. There are, however, small, but significant differences in the behaviour of the catalysts observed in the kinetically limited part of the RDE voltammogram. These are highlighted in the shown Figure 4-15 (B), which shows the forward sweep between -0.1 V and -0.7 V. Further, the size dependent activity in the kinetically controlled region is described using Figure 4-16. In this Figure, the data has been corrected to remove the contribution from the capacitance, which is much greater for the carbon supported high surface area catalysts.

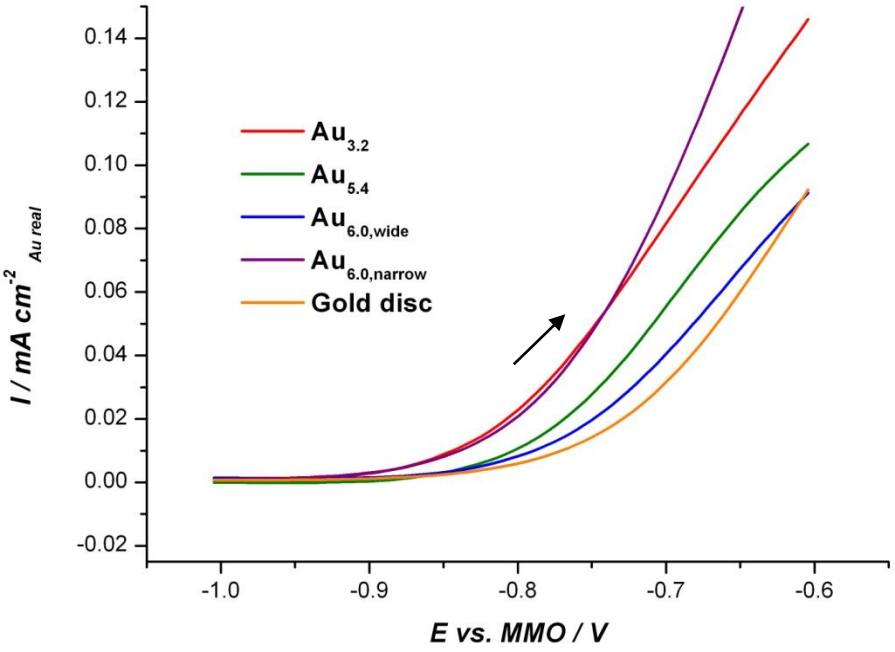


**Figure 4-16: CO oxidation curves on prepared catalysts in CO saturated 0.5 mol dm$^{-3}$ KOH at 900 rpm. Scan rate 20 mV s$^{-1}$. The current was normalized by the Au real area only region around the onset potential is shown.**

It can be clearly seen from Figure 4-16 that, there is a significant deviation observed in the kinetically controlled region between the different sizes of the prepared

catalysts as well as the bulk gold. To further study the size dependent activity of the catalysts, the mass transport corrected Tafel plots were constructed and shown in Figure 4-17. Again the data has been corrected for capacitance.

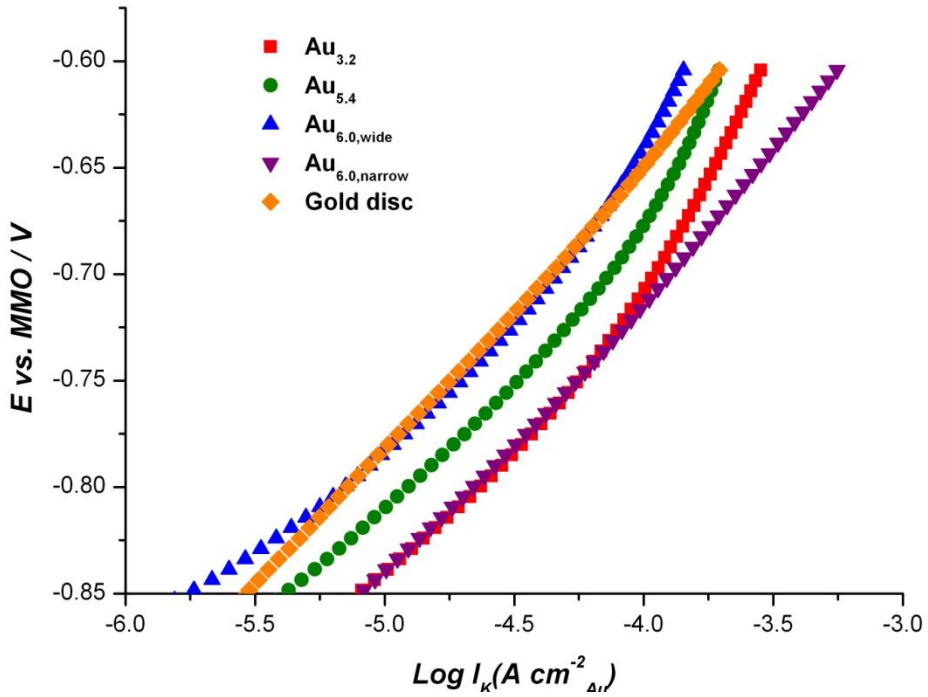


**Figure 4-17: Tafel plot for gold disc and the prepared catalysts in CO saturated 0.5 mol dm$^{-3}$ KOH at 900 rpm.**

From the Figures 4-16 and 4-17, the onset potential of oxidation (in this case the potential corresponds to the current density 3 µAcm$^{-2}_{\text{Au real}}$ is considered as onset potential) and the kinetic current density at -0.8 V are tabulated in Table 4-4.

**Table 4-4: Activity comparison of the prepared catalysts and the bulk gold.**

| Catalyst | Onset potential for CO oxidation / V | Kinetic current density at -0.8 V / µA cm$^{-2}_{\text{Au}}$ |
|---|---|---|
| $Au_{3.2}$ | -0.90 | 21 |
| $Au_{5.4}$ | -0.85 | 11 |
| $Au_{6.0,wide}$ | -0.85 | 6 |
| $Au_{6.0,narrow}$ | -0.90 | 20 |
| Gold disc | -0.90 | 6 |

There is a particle size dependent activity observed between the prepared catalysts. Even though it is not clear with respect to the onset potential, there is a significant difference amongst the kinetic current densities. The activity increases with decreasing size of the particle. The size dependency of the activity is mainly attributed to the relative strength of hydroxyl adsorption. As stated in the mechanism of CO oxidation, the adsorption of hydroxyl ions on gold surface enhances the adsorption of CO. As seen in Figure 4-3, higher hydroxyl coverage was observed at smaller particles. Therefore these adsorbed hydroxyl ions facilitate the CO adsorption on Au surface and increase the rate of CO oxidation on smaller particles. (However, the $Au_{6.0,\ narrow}$ shows extraordinary activity compared to the other catalysts. This high activity may be related to its particle size distribution).

To confirm this, the stationary CVs of each catalyst (first scan was selected) were plotted in one graph, the current was normalized by the real surface area of Au and represented as current density. Figure 4-18 shows the representative CV features of the prepared Au/C catalysts and the bulk gold in CO saturated 0.5 mol $dm^{-3}$ KOH solution.

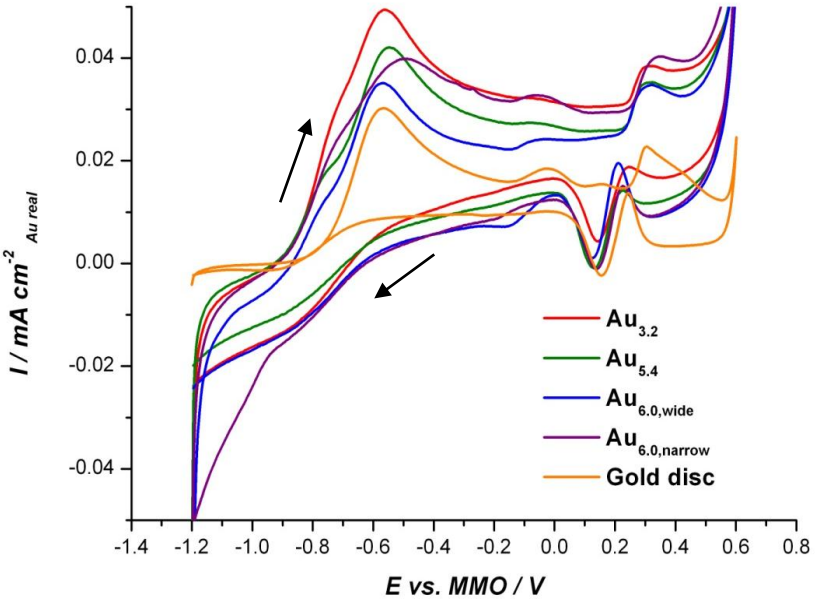


**Figure 4-18: Stationary voltammogram for the CO oxidation on prepared catalysts on GC disc (5 mm diameter) and the bulk gold in CO saturated 0.5 mol $dm^{-3}$ KOH. Scan rate 20 mV $s^{-1}$.**

CV features of the prepared Au/C catalysts are similar to the bulk gold. The current in the double layer region of the prepared catalysts is much larger compared to the bulk gold due to the double layer capacitance of the carbon support. Table 4-5 revealed the activity parameters of the prepared catalysts and the bulk gold.

**Table 4-5: Activity comparison of the prepared catalysts and the bulk gold.**

| Catalyst | Onset potential for CO oxidation / V |
|---|---|
| $Au_{3.2}$ | -0.87 |
| $Au_{5.4}$ | -0.87 |
| $Au_{6.0,wide}$ | -0.83 |
| $Au_{6.0,narrow}$ | -0.87 |
| Gold disc | -0.77 |

The onset potential for the oxidation is almost same for all the prepared catalysts. However, in this work the size dependent activity is seen with respect to the kinetic current density. The results on this research are comparable with those reported by many other researchers. Shaikhutdinov and coworkers[67] studied the CO adsorption on gold particle using temperature–programmed desorption and concluded that small particles adsorb CO more strongly and hence show the highest activity towards CO oxidation reaction. As explained in the introduction, Dongsheng Geng *et al.*[50] also confirmed the superior activity of smaller particles. They thought that at smaller particles Au (I) oxides are more favourable than Au (III) oxide and that the Au (I) oxides are responsible for the higher activity of smaller particles. Overbury and coworkers [68] studied the CO oxidation on different sizes of Au by using a flow reactor and showed the increase in activity with decrease in particle size of Au. They concluded that the higher activity of smaller particles was mainly linked to the higher density of low coordinated sites which enhances the CO adsorption. Most researchers found the optimum activity when the size is ~ 3 nm[55,58,69]. The small size of Au probably promotes the stronger adsorption of CO and leads to better activation. The work carried out in this research also confirms the superior activity of smaller particles.

# 3. Ethanol Oxidation Reaction

## 3.1 Introduction

There are numerous reports regarding the electro-oxidation of short chain alcohols (methanol, ethanol) mainly used in direct alcohol fuel cells[45,70-72]. The high solubility in aqueous electrolytes, low cost, easy handling, transport and storage make such alcohols more efficient in the electrochemical systems[73,74]. However, methanol has some disadvantages; that it is very toxic and inflammable with a low boiling point[75]. Interestingly ethanol has received much more attention due to its low toxicity and it can be produced in large quantities through the fermentation of biomass[76-78].

Even though the oxidation of ethanol on gold is not as good as Pt, it can be a very effective catalyst, particularly in the alkaline media[79]. In alkaline medium the only product detected is acetate[80].

$$CH_3CH_2OH + 5OH^- \rightarrow CH_3COO^- + 4\,H_2O + 4\,e^- \quad \textbf{[4-26]}$$

The reactivity of ethanol on gold in alkaline medium is associated with the fact that practically no poisoning species (CO like species) can be formed and adsorbed on to the surface. Nevertheless, the polished gold electrode with a smooth surface is a poor catalyst for ethanol oxidation. In most cases it is known that rough activated noble metals exhibit some unexpected properties in comparison with smooth surfaces[74].

The enhanced activity in alkaline solution is mainly attributed to the hydroxyl coverage on Au that initiates the adsorption of ethanol[80]. This was proved by Tremiliosi-Filho *et al*[81] who showed a tentative mechanism for the electro-oxidation of ethanol on polycrystalline gold electrode in alkaline medium .

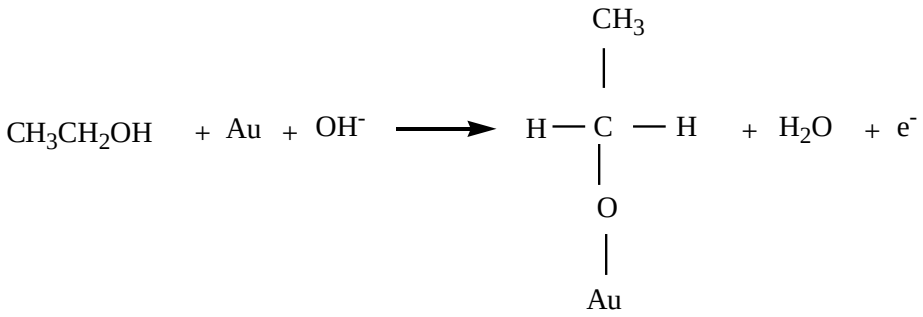

**[4-27]**

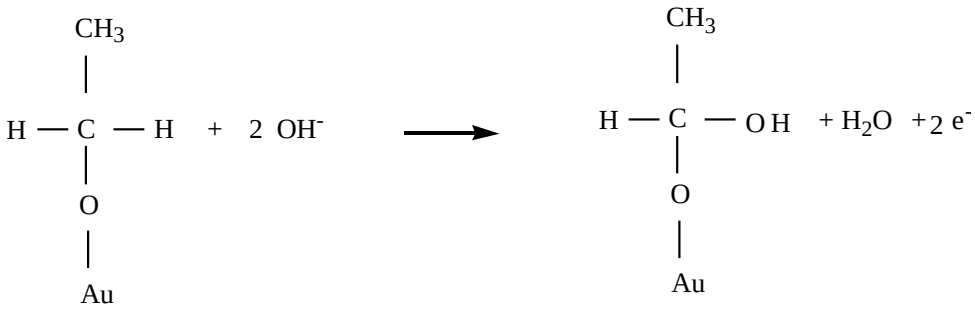

**[4-28]**

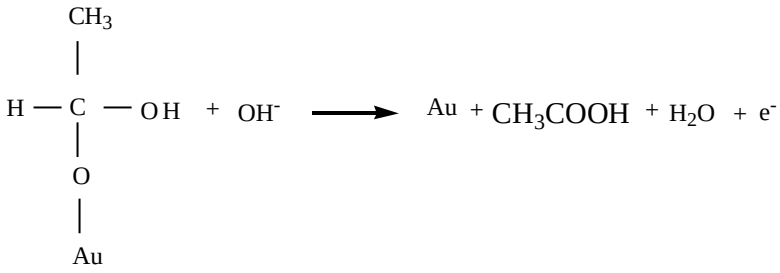

**[4-29]**

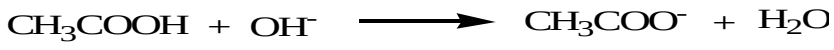

**[4-30]**

Overall the reaction is,

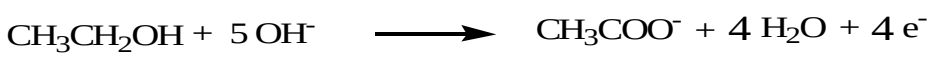

**[4-31]**

According to this mechanism, the adsorption of ethanol occurs via an ethoxy intermediate, with an interaction between the ethoxy intermediates and the non-adsorbed hydroxyl ions in the subsequent steps, with acetate as the final product. Therefore it is very clear that the hydroxyl ions facilitate the reaction mechanism.

As adsorbed hydroxyl ions are involved in the mechanism, the effect of pH influences the rate of the ethanol oxidation reaction. Lai and collaborators[82] have explained the pH effect on the ethanol oxidation on gold by employing phosphate buffers. At pH < 6 the ethanol oxidation CV overlapped with the blank CV (no ethanol present). This means that there are no significant features of ethanol oxidation at lower pH values. At pH > 6 the oxidation current exponentially increases with the pH. In addition to that, they observed a negative shift in the onset of ethanol oxidation with increasing pH. Conversely, the pH effect could not be validated using the above experiment because of the stronger adsorption of phosphate anions on the gold electrode that block the active sites for ethanol oxidation. However they observed a superior activity of a gold electrode in 0.1 mol $dm^{-3}$ NaOH solution compared to 0.1 mol $dm^{-3}$ $HClO_4$ solution.

The effect of pH on the oxidation is also discussed by Hernandez *et al*.[83] who studied the methanol oxidation on gold surface using CV and RDE experiments. They compared three different combinations of electrolyte systems for the oxidation of ethanol, 0.01 mol $dm^{-3}$ NaOH + 0.1 mol $dm^{-3}$ MeOH, 1 mol $dm^{-3}$ NaOH + 0.1 mol $dm^{-3}$ MeOH and 1 mol $dm^{-3}$ NaOH + 1 mol $dm^{-3}$ MeOH. There was no current observed at lower pH values (0.01 mol $dm^{-3}$ NaOH) and increase in the peak current and a negative shift for the onset of methanol oxidation at higher pH values indicating the important dependence of the oxidation on the pH. However it has been reported by many researchers, that when the gold surface is covered by an oxide layer the activity for the oxidation of ethanol sharply decreases[79,80]. This will be further explained later in this Chapter.

Hernandez *et al*. also correlated the oxidation activity with the water adsorption on the gold surface and showed the effect of crystal facets towards the methanol oxidation. In general, the methanol molecules should compete with the water molecules for the adsorption sites. It has been shown that water adsorption increases in the order Au (210) < Au (110) < Au (100) < Au (111). i.e. the interaction with water increases with increasing coordination number of the surface atoms. Therefore, a gold surface with very low coordinated atoms is less affected by water

molecules; hence shows higher activity in methanol oxidation reactions. Hence the activity increases in the order Au (210) > Au (110) > Au (100) > Au (111).

Apart from this, the particle size plays a major role in governing the activity of ethanol oxidation. It has been revealed that both small and larger particles are not efficient for the ethanol oxidation and usually the most optimum particle size would be 5-6 nm[77].

The purpose of this work is to investigate the particle size effect of Au/C catalysts towards the ethanol oxidation reaction in basic medium (0.05 mol $dm^{-3}$ KOH + 0.2 mol $dm^{-3}$ EtOH). Four Au/C catalysts were analysed for ethanol oxidation and the results are compared with bulk gold.

# 3.2 Experimental procedure

The electrode was prepared using the same method explained in Chapter two sections 3.4.2 (metal loading 10 μg $cm^{-2}$). The electrode was transferred to a solution of 0.05 mol $dm^{-3}$ KOH and purged with $N_{2\,(g)}$ whilst rotating the electrode at 1000 rpm for 15 min. The electrode rotation was stopped and trapped bubbles, if any on the electrode surface were removed. CVs were acquired from -0.3 V to 0.6 V vs. MMO reference electrode (calibrated as -0.07 V vs. saturated calomel electrode) with a scan rate of 10 mV $s^{-1}$ whilst flowing $N_{2\,(g)}$ at the top of the electrolyte to ensure no air gets in to the electrolyte.

Then the electrode was rinsed with distilled water and transferred to a solution of 0.05 mol $dm^{-3}$ KOH + 0.2 mol $dm^{-3}$ EtOH. The solution was then purged with $N_{2(g)}$ whilst rotating the electrode at 1000 rpm for 15 min. The electrode rotation was then stopped and trapped bubbles, if any on the electrode surface were removed. CVs were acquired from -0.3 V to 0.6 V vs. MMO reference electrode with a scan rate of 10 mV $s^{-1}$ whilst flowing $N_{2\,(g)}$ at the top of the electrolyte to ensure no air gets in to the electrolyte.

# 3.3 Results and Discussion

## 3.3.1 Ethanol oxidation on bulk gold

The stationary CV curves for ethanol oxidation on a bulk gold electrode (5mm diameter) in $N_2$ saturated 0.2 mol $dm^{-3}$ EtOH + 0.05 mol $dm^{-3}$ KOH are shown in Figure 4-19.

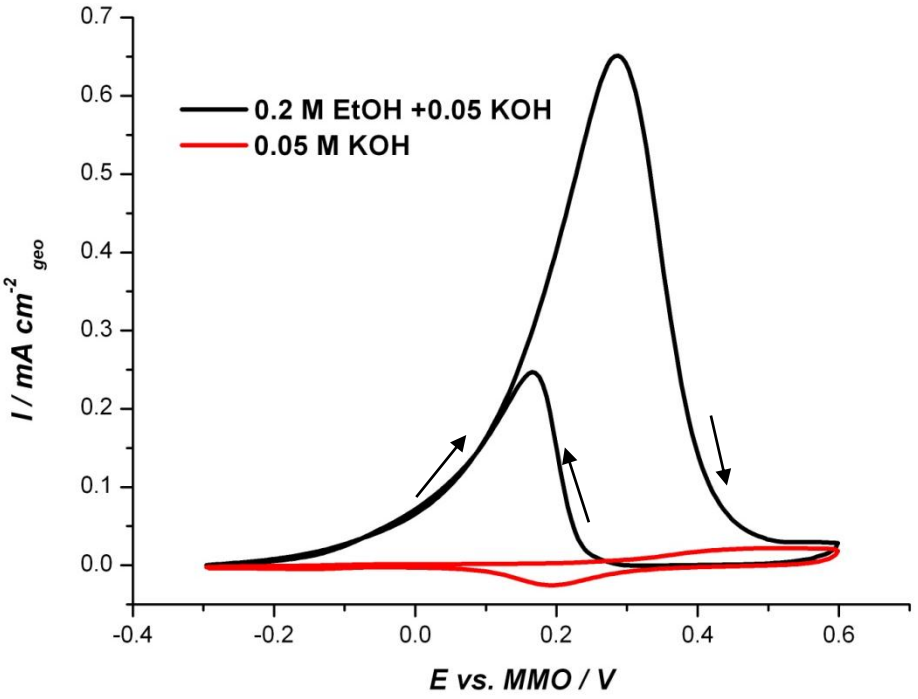


**Figure 4-19: CVs for bulk gold in $N_2$ saturated 0.2 mol $dm^{-3}$ EtOH + 0.05 mol $dm^{-3}$ KOH (black line) and in ethanol free solution (red line) at a scan rate 10 mV $s^{-1}$.**

The onset of ethanol oxidation begins at ~0.2 V vs. MMO (potential corresponds to 2.5 µA) which is well before the onset of surface oxidation. The current reaches a maximum at ~ 0.3 V. The product in Equation [4-27] can be considered as a precursor complex for the ethanoate producing reactions [4-28] and [4-29]. The anodic current peaks observed during the positive voltage scan in Figure 4-19 correspond to the sum of an anodic current of hydroxyl adsorption on Au, AuO formation and the ethanol oxidation reactions with most predominant contributions

from the ethanol oxidation reaction. As the Au sites are oxidised at $E \geq 0.25$ V, the ethanol oxidation reaction slows down and eventually stops. At this stage the Au surface is completely covered by an oxide layer and the ethanol oxidation is inhibited. When the potential is above 0.5 V the oxidation current almost coincides with the base current in the supporting electrolyte system. This is due to the complete inhibition of ethanol oxidation on oxide covered Au. On the return negative scan, the AuO sites are reduced back to Au, reactivating Au active sites. The secondary anodic current peak observed during the negative voltage scan in Figure 4-19 is due to the reactivation of ethanol oxidation following successive reduction of the AuO. Thus, reduction of AuO affects the reactivation of the ethanol oxidation during the negative voltage scan. The secondary anodic current is a net current of anodic current for ethanol oxidation and a cathodic current for reduction of AuO[71].

Furthermore, there is a clear difference between the currents in the positive and negative scans. The negative scan currents are considerably smaller than the positive scan. Various explanations can be put forward to justify these phenomena. Firstly, the positive scan current is the summation of surface oxidation and the ethanol oxidation (both current values are positive). However, the negative scan current is the net current from the positive current of ethanol oxidation and the negative current of oxide reduction. Secondly, in the negative scan there may be some adsorbed poison formed on the Au surface that blocks the active sites for ethanol oxidation. lastly, there may be some irreversible adsorption of hydroxyl ions in the negative scan that prevents further oxidation of ethanol[83].

Ethanol molecules consumed during the oxidation of ethanol and the effect on the oxidation current as a function of number of scans are plotted in Figure 4-20.

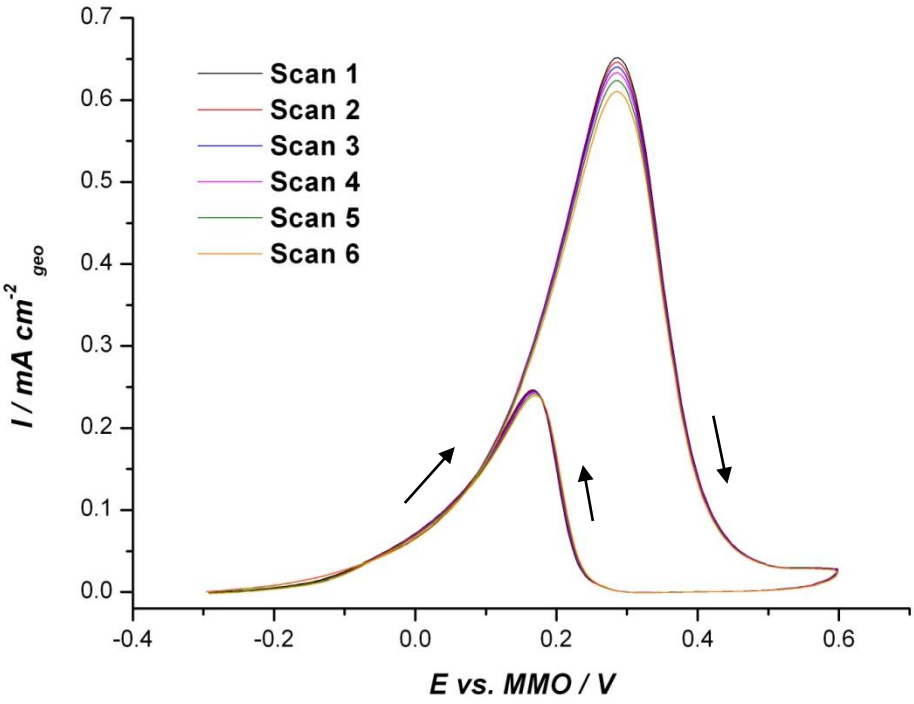


**Figure 4-20: Cyclic voltammograms for bulk gold disc (5mm diameter) in $N_2$ saturated 0.2 mol $dm^{-3}$ EtOH + 0.05 mol $dm^{-3}$ KOH at a scan rate 10 mV $s^{-1}$.**

It is very clear from the above Figure that the oxidation current decreases with the number of scans. This may be due to the consumption of ethanol during the reaction. Therefore the first scan (showing the higher current) was considered in the study of ethanol oxidation.

## 3.3.2 Ethanol oxidation on Au/C catalysts

Figure 4-21 shows representative current–potential curves (stationary CVs) for the ethanol oxidation at the Au/C catalysts on the RDE in $N_2$-saturated 0.2 mol $dm^{-3}$ EtOH + 0.05 mol $dm^{-3}$ KOH.

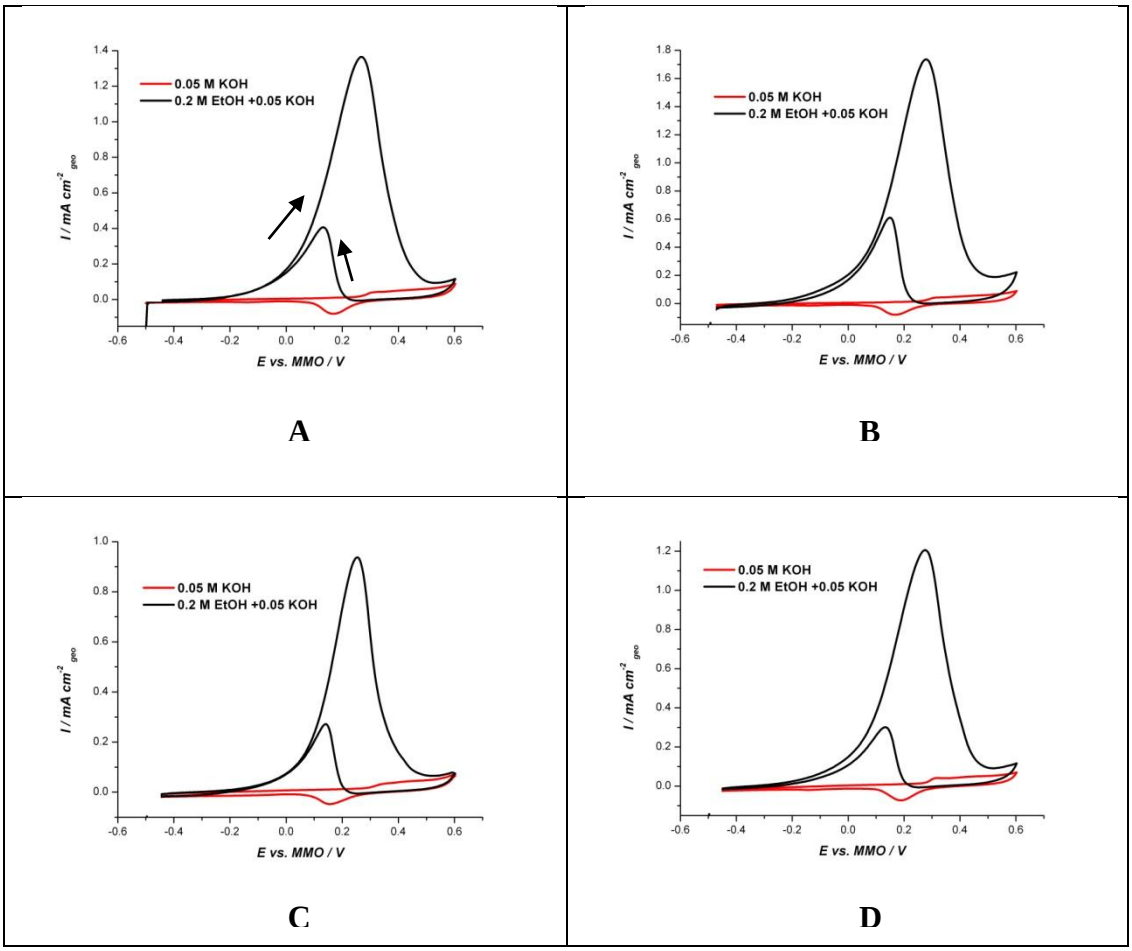


**Figure 4-21: Cyclic voltammograms for (A) $Au_{3.2}$, (B) $Au_{5.4}$, (C) $Au_{6.0,wide}$ and (D) $Au_{6.0,narrow}$ on GC electrode (5 mm diameter) in $N_2$ saturated 0.2 mol $dm^{-3}$ EtOH + 0.05 mol $dm^{-3}$ KOH (black line) and in ethanol free solution (red line) at a scan rate 10 mV $s^{-1}$.**

The voltammetric profiles of the prepared Au/C catalysts are similar to the one observed for bulk gold. This indicates that there are similar mechanisms occurring at both bulk gold and the prepared catalysts.

All the prepared Au/C catalysts are plotted in one Figure (Figure 4-22) with the CV of Vulcan carbon powder to see any effect from the oxidation of ethanol in carbon powder.

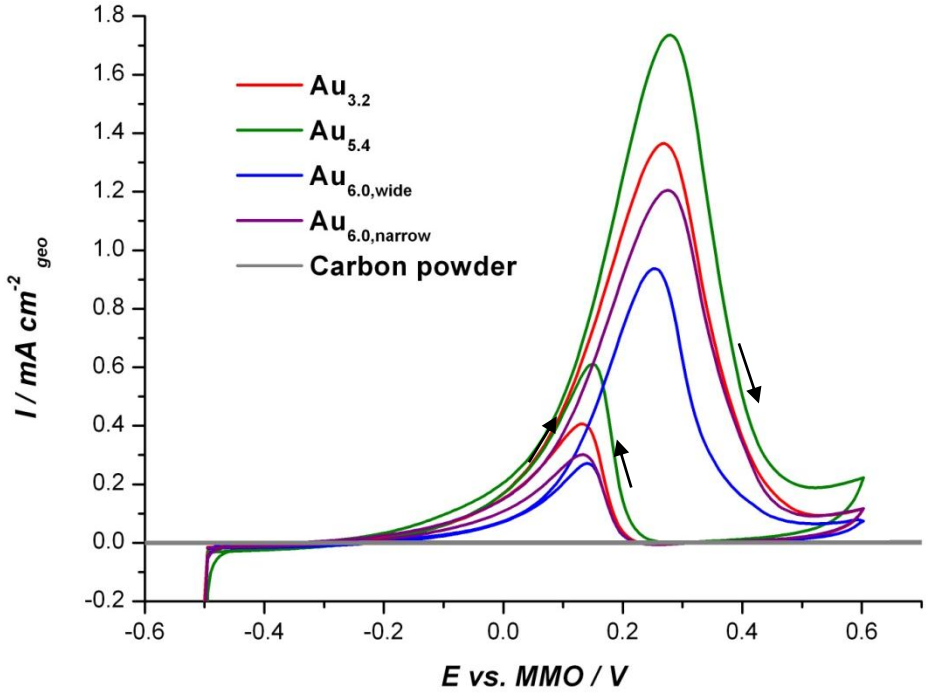


**Figure 4-22: Ethanol oxidation on prepared Au/C catalysts and carbon powder in $N_2$ saturated 0.2 mol $dm^{-3}$ EtOH + 0.05 mol $dm^{-3}$ KOH solution. Scan rate 10 mV $s^{-1}$.**

According to the above Figure, there is no significant current observed for carbon powder indicating the inactivity of the carbon support towards the ethanol oxidation.

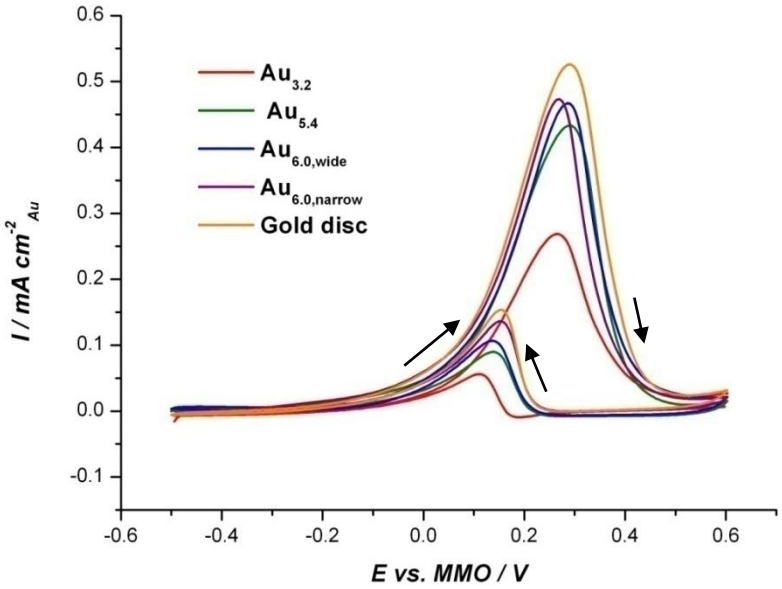


**Figure 4-23: Ethanol oxidation on prepared Au/C catalysts and bulk gold in $N_2$ saturated 0.2 mol $dm^{-3}$ EtOH + 0.05 mol $dm^{-3}$ KOH solution. Scan rate 10 mV $s^{-1}$. The current was normalized by the Au real area.**

The shape of the ethanol oxidation CVs in Figure 4-23 are similar for all the prepared catalysts and bulk gold suggesting that the same reaction mechanism occurs over differently sized Au/C catalysts and bulk gold. There are clear differences observed between the catalysts as summarized in Table 4-6.

**Table 4-6: CV parameters for the prepared Au catalysts and the bulk gold.**

| Catalysts | Anodic onset potential (at current density 3 μA $cm^{-2}$)/ V | Anodic peak current density / mA $cm^{-2}$ | Cathodic onset potential (at current density 7 μA $cm^{-2}$/ V | Cathodic peak current density / mA $cm^{-2}$ |
|---|---|---|---|---|
| $Au_{3.2}$ | -0.17 | 0.27 | 0.16 | 0.06 |
| $Au_{5.4}$ | -0.43 | 0.43 | 0.20 | 0.09 |
| $Au_{6.0,wide}$ | -0.50 | 0.46 | 0.20 | 0.11 |
| $Au_{6.0,narrow}$ | -0.45 | 0.47 | 0.23 | 0.13 |
| Bulk gold | -0.47 | 0.53 | 0.25 | 0.15 |

Interestingly, bulk gold shows higher activity compared to the prepared Au/C catalysts. The early onset potential and the higher specific activity of bulk gold make it more efficient in ethanol oxidation reaction.

Once again, size effect may be explained by the hydroxyl adsorption on the Au surface. Although the adsorption of hydroxyl ions on the Au surface enhances the ethanol oxidation reaction, when these adsorption is stronger (irreversible adsorption) the active sites of Au are completely blocked by the hydroxyl species resulting in difficulties in the adsorption of ethanol. As explained in Figure 4-3, the smaller particles adsorb hydroxyl ions more strongly compared to larger ones and this retards the ethanol oxidation reaction. This work also explained that in addition to the size of the Au, the size distribution also plays a role in the ethanol oxidation.

There are a few reports that explain the size effect of Au towards the ethanol oxidation on gold. Ke-Qiang Sun *et al.*[84] studied the ethanol oxidation over differently sized Au particles and showed that the optimum activity was obtained

when the size is ~5 nm. Moreover, they noticed a decrease in activity of Au particles which are either smaller or larger than 5 nm. The above statement was agreed with Yejun Guan and coworkers[77], who investigated the effect of particle size on the dehydrogenation of ethanol using a single pulse micro reactor system. They also observed that a catalytic particle about 6 nm shows much higher activity than smaller or larger particles. They claimed that the superior catalytic activity is mainly attributed to the existence of surface steps with an appropriate geometry for the removal of *β*–H from the adsorbed ethanoate and such stepped sites are expected to be present with maximum density for intermediate particle size. The largest size of Au in this work is 6 nm. Therefore there may be some reduction in activity beyond 6 nm.

# 4. Conclusion

In this Chapter different sizes of chemically prepared Au/C catalysts were compared with bulk gold towards the ORR, carbon monoxide oxidation reaction and ethanol oxidation reaction in alkaline medium. Furthermore, the particle size effect of Au/C catalysts on the activity of those reactions has been investigated.

As explained in the literature, the rates of the above chemical reactions have been shown to depend predominantly on the size and shape (crystallographic facets) of the catalysts, pH of the solution as well as the support on which the nanoparticles are immobilized. However, according to the UPD measurements, the ratio of Au (111) / Au (110) is almost constant in all the prepared catalysts; indicating that there is no significant change in the shape of the prepared Au/C catalysts. The same electrolyte (0.5 mol $dm^{-3}$ KOH in the case of ORR and CO oxidation reaction and 0.05 mol $dm^{-3}$ KOH in ethanol oxidation reaction) was used for all the prepared catalysts therefore the effect of pH was not studied. The same support (Vulcan carbon XC-72 R) was used to support all the Au nanoparticles. Therefore the only difference that influenced the chemical reactions was the size of the Au catalysts.

In some reactions (ORR and ethanol oxidation reactions) the larger particles favour whereas in others (CO oxidation reaction) smaller particles show higher activity. The reaction kinetics of the ORR, CO oxidation and ethanol oxidation reaction is dependent on the surface coverage of oxygenated species. Adsorbed OH is an adduct species and facilitates the reaction but can also act as a surface site blocking species and inhibits the reaction. The surface coverage by $OH^-$ ion is increased by decreasing the particle size (Figure 4-3). If adsorbed $OH^-$ species is a promoter of a reaction (CO oxidation reaction) then an increase in oxophilicity with a decrease in particle size results in increased reaction kinetics. On the other hand, for the ORR and the ethanol oxidation reaction, the increase in oxophilicity with smaller particles leads to a decrease in reaction kinetics. This is due to the fact that, OH ions can effectively block the active sites required for the adsorption of the reactant molecules. The onset potential of CO oxidation reaction is ~ -0.8 V vs. MMO whereas those of the ethanol oxidation and the ORR are -0.1 V and 0 V respectively. Therefore in the case of CO oxidation at the far negative onset potential there will be a weaker adsorption of OH ions and these adsorbed $OH^-$ ions can facilitate the oxidation reaction; however, in the case of ethanol oxidation and the ORR at this comparatively positive onset potential the irreversible adsorption of OH anions on smaller particles leads to impede the reaction.

# 5. References

(1) Pylypenko, S.; Olson, T. S.; Carroll, N. J.; Petsev, D. N.; Atanassov, P. *The Journal of Physical Chemistry C* 2010, *114*, 4200.

(2) Gupta, G.; Slanac, D. A.; Kumar, P.; Wiggins-Camacho, J. D.; Wang, X.; Swinnea, S.; More, K. L.; Dai, S.; Stevenson, K. J.; Johnston, K. P. *Chemistry of Materials* 2009, *21*, 4515.

(3) Laoire, C. O.; Mukerjee, S.; Abraham, K. M.; Plichta, E. J.; Hendrickson, M. A. *The Journal of Physical Chemistry C* 2009, *113*, 20127.

(4) Zhang, S. S.; Foster, D.; Read, J. *Journal of Power Sources* 2010, *195*, 1235.

(5) Markovic, N.; Gasteiger, H.; Ross, P. N. *Journal of The Electrochemical Society* 1997, *144*, 1591.

(6) Zhang, S.; Shao, Y.; Yin, G.; Lin, Y. *Journal of Materials Chemistry* 2009, *19*, 7995.

(7) Jiang, L.; Hsu, A.; Chu, D.; Chen, R. *Journal of The Electrochemical Society* 2009, *156*, B370.

(8) Tang, W.; Lin, H.; Kleiman-Shwarsctein, A.; Stucky, G. D.; McFarland, E. W. *The Journal of Physical Chemistry C* 2008, *112*, 10515.

(9) Su, B.; Hatay, I.; Trojánek, A. n.; Samec, Z. k.; Khoury, T.; Gros, C. P.; Barbe, J.-M.; Daina, A.; Carrupt, P.-A.; Girault, H. H. *Journal of the American Chemical Society* 2010, *132*, 2655.

(10) El-Deab, M. S.; Sotomura, T.; Ohsaka, T. *Electrochimica Acta* 2006, *52*, 1792.

(11) El-Deab, M. S.; Ohsaka, T. *Electrochimica Acta* 2002, *47*, 4255.

(12) El-Deab, M. S.; Sotomura, T.; Ohsaka, T. *Electrochemistry Communications* 2005, *7*, 29.

(13) Guo, J.; Hsu, A.; Chu, D.; Chen, R. *The Journal of Physical Chemistry C* 2010, *114*, 4324.

(14) Kazeman, I.; Hasanzadeh, M.; Jafarian, M.; Shadjou, N.; Khalilzadeh, B. *Chinese Journal of Chemistry* 2010, *28*, 504.

(15) Wang, J.-H.; Liu, M.; Lin, M. C. *Solid State Ionics* 2006, *177*, 939.

(16) Lefevre, M.; Proietti, E.; Jaouen, F.; Dodelet, J.-P. *Science* 2009, *324*, 71.

(17) Shao, M.-H.; Sasaki, K.; Adzic, R. R. *Journal of the American Chemical Society* 2006, *128*, 3526.

(18) Lee, J.-W.; Popov, B. *Journal of Solid State Electrochemistry* 2007, *11*, 1355.

(19) Hernández, J.; Solla-Gullón, J.; Herrero, E. *Journal of Electroanalytical Chemistry* 2004, *574*, 185.

(20) Zhang, Y.; Asahina, S.; Yoshihara, S.; Shirakashi, T. *Electrochimica Acta* 2003, *48*, 741.

(21) El-Deab, M. S.; Okajima, T.; Ohsaka, T. *Journal of The Electrochemical Society* 2003, *150*, A851.

(22) Mirkhalaf, F.; Tammeveski, K.; Schiffrin, D. J. *Physical Chemistry Chemical Physics* 2009, *11*, 3463.

(23) Prieto, A.; Hernández, J.; Herrero, E.; Feliu, J. *Journal of Solid State Electrochemistry* 2003, *7*, 599.

(24) Inasaki, T.; Kobayashi, S. *Electrochimica Acta* 2009, *54*, 4893.

(25) Kim, J.; Gewirth, A. A. 2006; Vol. 110, p 2565.

(26) Alexeyeva, N.; Laaksonen, T.; Kontturi, K.; Mirkhalaf, F.; Schiffrin, D. J.; Tammeveski, K. *Electrochemistry Communications* 2006, *8*, 1475.

(27) Paliteiro, C.; Martins, N. *Electrochimica Acta* 1998, *44*, 1359.

(28) Sarapuu, A.; Tammeveski, K.; Tenno, T. T.; Sammelselg, V.; Kontturi, K.; Schiffrin, D. J. *Electrochemistry Communications* 2001, *3*, 446.

(29) Shao, M. H.; Adzic, R. R. *The Journal of Physical Chemistry B* 2005, *109*, 16563.

(30) Strbac, S.; Adzic, R. R. *Electrochimica Acta* 1996, *41*, 2903.

(31) Kim, J.; Gewirth, A. A. *The Journal of Physical Chemistry B* 2006, *110*, 2565.

(32) Yagi, I.; Ishida, T.; Uosaki, K. *Electrochemistry Communications* 2004, *6*, 773.

(33) Guerin, S.; Hayden, B. E.; Pletcher, D.; Rendall, M. E.; Suchsland, J. P. *Journal of Combinatorial Chemistry* 2006, *8*, 791.

(34) El-Deab, M. S.; Sotomura, T.; Ohsaka, T. *Electrochemistry Communications* 2005, *7*, 29.

(35) Luo, J.; Njoki, P. N.; Lin, Y.; Wang, L.; Zhong, C. J. *Electrochemistry Communications* 2006, *8*, 581.

(36) Erikson, H.; Jürmann, G.; Sarapuu, A.; Potter, R. J.; Tammeveski, K. *Electrochimica Acta* 2009, *54*, 7483.

(37) Bron, M. Journal of Electroanalytical Chemistry 2008, *624*, 64.

(38) Gubbins, K. E.; Walker, J. R. D. *Journal of The Electrochemical Society* 1965, *112*, 469.

(39) Tsushima, M.; Tokuda, K.; Ohsaka, T. 1994; Vol. 66, p 4551.

(40) Strbac, S.; Anastasijevic, N. A.; Adzic, R. R. *Journal of Electroanalytical Chemistry* 1992, *323*, 179.

(41) Sarapuu, A.; Nurmik, M.; Mandar, H.; Rosental, A.; Laaksonen, T.; Kontturi, K.; Schiffrin, D. J.; Tammeveski, K. *Journal of Electroanalytical Chemistry, In Press, Corrected Proof*.

(42) Sarapuu, A.; Nurmik, M.; Mandar, H.; Rosental, A.; Laaksonen, T.; Kontturi, K.; Schiffrin, D. J.; Tammeveski, K. *Journal of Electroanalytical Chemistry* 2008, *612*, 78.

(43) Greeley.J; J., R.; Hellman.A; Norskov, J. K. *Z.Phys.Chem* 2007, *221*, 1209.

(44) Jarvi, T. D.; Sriramulu, S.; Stuve, E. M. *The Journal of Physical Chemistry B* 1997, *101*, 3649.

(45) Wasmus, S.; Küver, A. Journal of Electroanalytical Chemistry 1999, *461*, 14.

(46) Wu, X.-G.; Kapral, R. Physica A: Statistical Mechanics and its Applications 1992, *188*, 284.

(47) Hong, S.; Richardson, H. H. Journal of Vacuum Science & Technology A: Vacuum, Surfaces, and Films 1993, *11*, 1951.

(48) Angelucci, C. A.; Herrero, E.; Feliu, J. M. *The Journal of Physical Chemistry C* 2010, *114*, 14154.

(49) Haruta, M. K., T.;Sano,H.;Yamada,N *Chemistry letters* 1987, *2*, 405.

(50) Geng, D.; Lu, G. *Journal of Nanoparticle Research* 2007, *9*, 1145.

(51) Hayden, B. E.; Pletcher, D.; Rendall, M. E.; Suchsland, J. P. *The Journal of Physical Chemistry C* 2007, *111*, 17044.

(52) Rodriguez, P.; Garcia-Araez, N.; Koper, M. T. M. *Physical Chemistry Chemical Physics* 2010, *12*, 9373.

(53) Kunimatsu, K.; Aramata, A.; Nakajima, N.; Kita, H. *Journal of Electroanalytical Chemistry* 1986, *207*, 293.

(54) Cuesta, A.; López, N.; Gutiérrez, C. *Electrochimica Acta* 2003, *48*, 2949.

(55) Haruta, M.; Tsubota, S.; Kobayashi, T.; Kageyama, H.; Genet, M. J.; Delmon, B. *Journal of Catalysis* 1993, *144*, 175.

(56) Bond, G. C.; Thompson, D. T. *Catalysis Reviews: Science and Engineering* 1999, *41*, 319

(57) Comotti, M.; Li, W.-C.; Spliethoff, B.; Schüth, F. *Journal of the American Chemical Society* 2005, *128*, 917.

(58) Valden, M.; Lai, X.; Goodman, D. W. *Science* 1998, *281*, 1647.

(59) Cuenya, B. R.; Baeck, S.-H.; Jaramillo, T. F.; McFarland, E. W. *Journal of the American Chemical Society* 2003, *125*, 12928.

(60) Schubert, M. M.; Hackenberg, S.; van Veen, A. C.; Muhler, M.; Plzak, V.; Behm, R. J. *Journal of Catalysis* 2001, *197*, 113.

(61) Rodriguez, P.; Feliu, J. M.; Koper, M. T. M. *Electrochemistry Communications* 2009, *11*, 1105.

(62) Kita, H.; Nakajima, H.; Hayashi, K. *Journal of Electroanalytical Chemistry* 1985, *190*, 141.

(63) Shue, C.-H.; Ou Yang, L.-Y.; Yau, S.-L.; Itaya, K. *Langmuir* 2005, *21*, 1942.

(64) Sun, S.-G.; Cai, W.-B.; Wan, L.-J.; Osawa, M. *The Journal of Physical Chemistry B* 1999, *103*, 2460.

(65) Blizanac, B. B.; Arenz, M.; Ross, P. N.; Marković, N. M. *Journal of the American Chemical Society* 2004, *126*, 10130.

(66) Gallagher, M. E.; Blizanac, B. B.; Lucas, C. A.; Ross, P. N.; Markovic, N. M. *Surface Science* 2005, *582*, 215.

(67) Shaikhutdinov, S. K.; Meyer, R.; Naschitzki, M.; Bäumer, M.; Freund, H. J. *Catalysis Letters* 2003, *86*, 211.

(68) Overbury, S. H.; Schwartz, V.; Mullins, D. R.; Yan, W.; Dai, S. *Journal of Catalysis* 2006, *241*, 56.

(69) Zanella, R.; Giorgio, S.; Shin, C.-H.; Henry, C. R.; Louis, C. *Journal of Catalysis* 2004, *222*, 357.

(70) Lamy, C.; Lima, A.; LeRhun, V.; Delime, F.; Coutanceau, C.; Léger, J.-M. *Journal of Power Sources* 2002, *105*, 283.

(71) Assiongbon, K. A.; Roy, D. *Surface Science* 2005, *594*, 99.

(72) Borkowska, Z.; Tymosiak-Zielinska, A.; Shul, G. *Electrochimica Acta* 2004, *49*, 1209.

(73) Park, I.-S.; Lee, K.-S.; Cho, Y.-H.; Park, H.-Y.; Sung, Y.-E. *Catalysis Today* 2008, *132*, 127.

(74) Yu, C.; Jia, F.; Ai, Z.; Zhang, L. *Chemistry of Materials* 2007,*19*,6065

(75) Lamy, C.; Lima, A.; LeRhun, V.; Delime, F.; Coutanceau, C.; Leger, J.-M. *Journal of Power Sources* 2002, *105*, 283.

(76) Gong, J.; Mullins, C. B. *Journal of the American Chemical Society* 2008, *130*, 16458.

(77) Guan, Y.; Hensen, E. J. M. *Applied Catalysis A: General* 2009, *361*, 49.

(78) Xu, C.; Shen, P. k.; Liu, Y. *Journal of Power Sources* 2007, *164*, 527.

(79) Lima R B de; Varela, H. *Gold Bulletin* 2008, *41*, 15.

(80) Tremiliosi-Filho, G.; Gonzalez, E. R.; Motheo, A. J.; Belgsir, E. M.; Leger, J. M.; Lamy, C. *Journal of Electroanalytical Chemistry* 1998, *444*, 31.

(81) Tremiliosi-Filho, G.; Gonzalez, E. R.; Motheo, A. J.; Belgsir, E. M.; Léger, J. M.; Lamy, C. *Journal of Electroanalytical Chemistry* 1998, *444*, 31.

(82) Lai, S. C. S.; Kleijn, S. E. F.; Öztürk, F. T. Z.; van Rees Vellinga, V. C.; Koning, J.; Rodriguez, P.; Koper, M. T. M. *Catalysis Today* 2010, *154*, 92.

(83) Hernández, J.; Solla-Gullón, J.; Herrero, E.; Aldaz, A.; Feliu, J. M. *Electrochimica Acta* 2006, *52*, 1662.

(84) Sun, K.-Q.; Luo, S.-W.; Xu, N.; Xu, B.-Q. *Catalysis Letters* 2008, *124*, 238.

# Chapter Five: Modification of the Surface Core – Shell catalysts

## 1. Preparation of Core – Shell catalysts

The deposition of a foreign metal (shell) on to a substrate is of great significance and is also a great challenge in surface science and heterogeneous catalysts[1-6]. Redox replacement of a UPD layer plays an important role in preparation of layered catalysts. Amongst the metals investigated the UPD of Cu as the displacement layer has received much more attention[7-10].

In this work, the Au surface was modified with Pt or Pd via the redox replacement of a Cu monolayer. At the beginning, the correct composition of the electrolyte system was chosen by analysing the deposition of Cu in three different electrolyte systems. The Cu ad-layer on the Au surface can be dissolved in acidic solution. Therefore three neutral compositions were analysed.

1. $CuCl_2$ / NaCl
2. $CuSO_4$ / $Na_2SO_4$
3. $Cu(ClO_4)_2$ / $NaClO_4$

CVs of Au electrode (5 mm diameter) were obtained in each of the electrolyte systems and are presented in Figure 5-1.

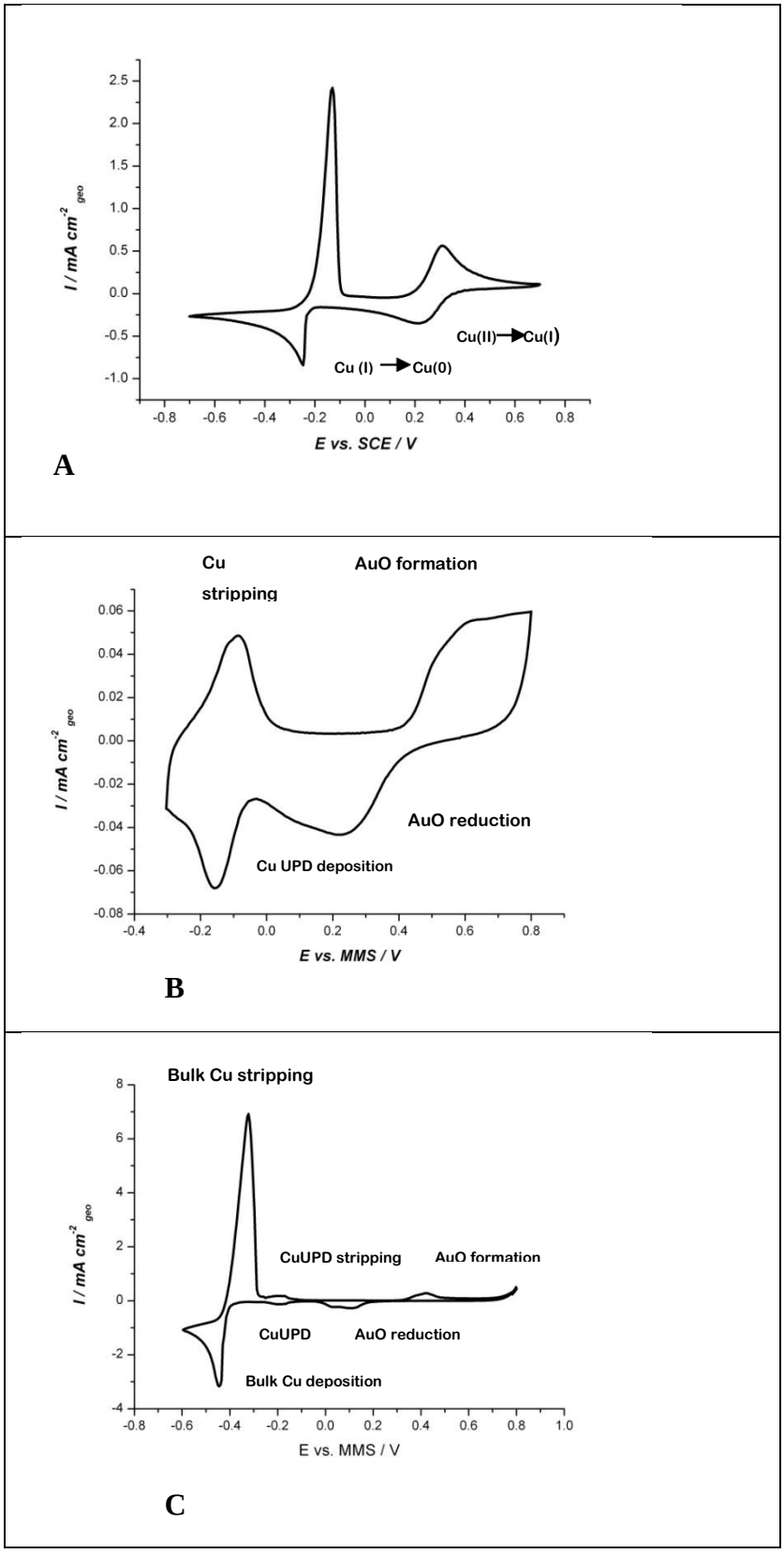


**Figure 5-1: CV curves of gold disc (5mm diameter) in (A) 0.01 mol $dm^{-3}$ $CuCl_2$ / 3 mol $dm^{-3}$ NaCl, (B) 0.01 mol $dm^{-3}$ $CuSO_4$ / 0.1 mol $dm^{-3}$ $Na_2SO_4$ and (C) 0.01 mol $dm^{-3}$ $Cu(ClO_4)_2$ / 0.1 mol $dm^{-3}$ $NaClO_4$. Scan rate 20 mV $s^{-1}$.**

In the chloride system, the redox couple of $Cu^{2+}/Cu^{+}$ is clearly seen in the region 0.25 V to 0.35 V. The bulk deposition and the corresponding stripping are observed at ~ -0.2 V. However, the UPD region is not clearly noticeable. In the sulphate system, the Au oxide reduction and the oxidation of Au are observed at 0.35 V and 0.65 V respectively. The UPD and the corresponding stripping of Cu are observed at ~0.1 V, but, the bulk deposition is not visible. In the perchlorate system, the region of Au oxide formation and its reduction are seen at 0.4 V and 0.1 V respectively. The region of the deposition of Cu and the stripping are seen at ~ -0.2 V. The bulk deposition began beyond the potential at ~-0.4 V.

Therefore the chloride system was automatically eliminated due to the absence of UPD. To choose the best electrolyte composition, the sulphate and perchlorate systems were compared in the UPD region and are shown in Figure 5-2.

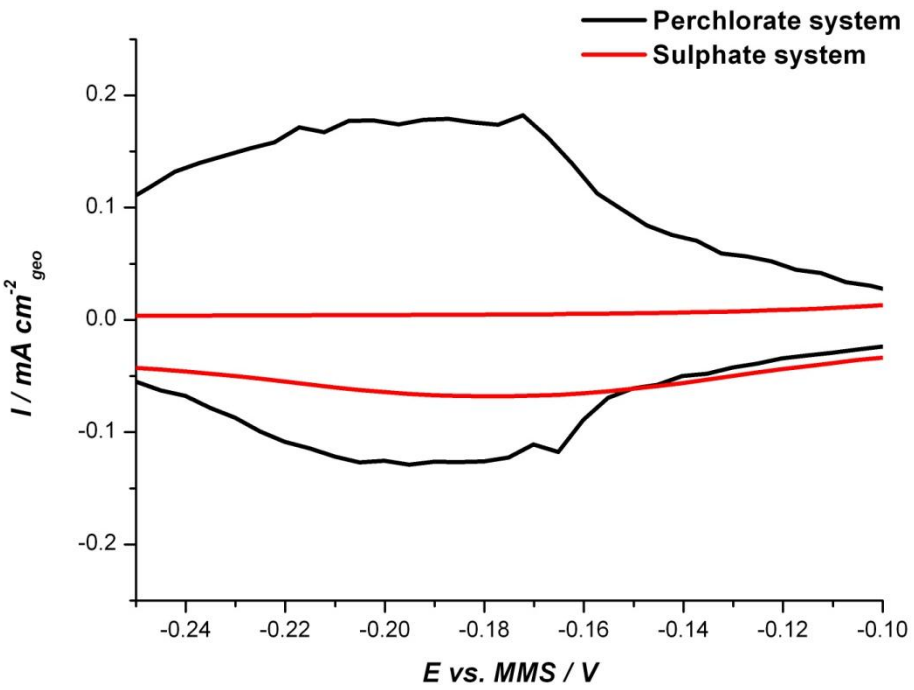


**Figure 5-2: Comparison of perchlorate and sulphate system in the UPD region. Scan rate 20 mV $s^{-1}$.**

The current in the perchlorate system is larger than that in the sulphate system. This can be explained by the stronger adsorption of sulphate anions when compared to perchlorate anions. In other words, $SO_4^{2-}$ and $HSO_4^{-}$ have to be displaced before the

adsorption of $Cu^{2+}$ on the surface and $Cu^{2+} \rightarrow Cu^{0}$ is very inefficient. Therefore, the perchlorate composition was chosen as a suitable electrolyte system for the UPD of Cu on Au surfaces.

Once the perchlorate system was chosen, the UPD method was used to modify the prepared catalysts. Vulcan carbon powder was also tested in $Cu(ClO_4)_2$ / $NaClO_4$ solution to see whether there is any Cu deposition on the carbon powder and the CV was plotted in Figure 5-3.

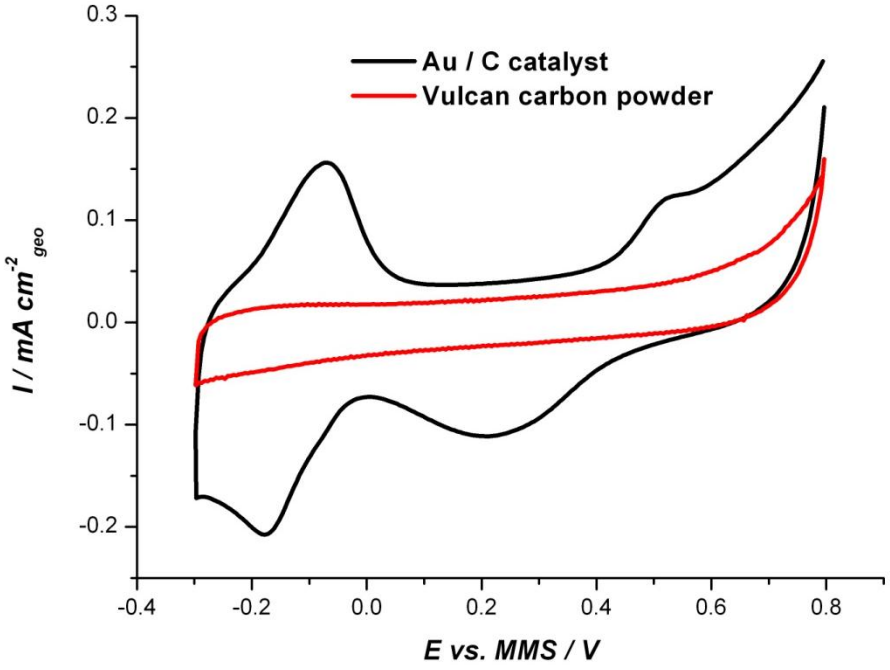


**Figure 5-3: CV curve of 25 wt % Au/C (GC disc 5 mm diameter) in 0.01 mol $dm^{-3}$ Cu $(ClO_4)_2$ & 0. 1mol $dm^{-3}$ $NaClO_4$. Scan rate 20 mV $s^{-1}$.**

The conclusion that can be made is that there is no significant deposition of Cu on the carbon powder up to -300 mV vs. MMS.

Therefore to form a Cu monolayer on the Au surface all the prepared catalysts were linearly scanned from 0.8 V to -0.25 V in 0.01 mol $dm^{-3}$ $Cu(ClO_4)_2$ / 0.1 mol $dm^{-3}$ $NaClO_4$ at 20 mV $s^{-1}$ scan rate. Then the electrode was held at -0.25 V for 10 min to ensure the formation of a complete Cu layer. Once the Cu monolayer was formed on the Au surface, the replacement of the UPD monolayer was carried out by immersing

the electrode in $N_2$ saturated 5 mmol $dm^{-3}$ $K_2PtCl_4$ (in the case of Pt shell–Au core) or in 5 mmol $dm^{-3}$ $K_2PdCl_4$ (in the case of Pd shell–Au core) for 15 minutes to make sure the complete replacement of Cu by Pt or Pd.

The displacement reaction during which the Cu layer is replaced with Pt or Pd can be explained according to the following overall Equations.

$$Cu^0/Au + PtCl_4^{2-} \rightarrow Pt^0/Au + Cu^{2+} + 4Cl^- \quad \textbf{[5-1]}$$

$$Cu^0/Au + PdCl_4^{2-} \rightarrow Pd^0/Au + Cu^{2+} + 4Cl^- \quad \textbf{[5-2]}$$

The driving force for this displacement mechanism is the positive difference between the equilibrium potential of Pt or Pd in contact with its complexes and the equilibrium potential of the UPD layer. Thus the Cu atoms on the surface get oxidized by the Pt or Pd complexes and are replaced by Pt or Pd atoms respectively. Through this mechanism the amount of metal deposited is determined by the stoichiometry of the redox reaction.

In work described in this Chapter, all the Au catalysts were modified with Pt or Pd. The modified catalysts have been characterized by cyclic voltammetric and CO stripping experiments. Then they were compared for the oxygen reduction and ethanol oxidation reactions. The effect of the Pt or Pd over-layer on the electrochemical activity will be investigated. Most of the experimental techniques were discussed in Chapter two section 3.3 and Chapter four. The CO stripping method is described below.

The experimental setup is similar to the one explained in Chapter two section 3.3, measurements were conducted in 1 mol $dm^{-3}$ $H_2SO_4$ solution. The CO stripping experiment was carried out by holding the potential at -0.65 V vs. MMS while purging with CO for 10 min to adsorb CO on to the Pt or Pd surface. Thereafter $N_2$ was purged for 20 min to remove any dissolved CO, ensuring that any CO oxidation observed in the voltammetric response is from CO adsorbed on the Pt or Pd surface only. Then 2 scans were obtained from -0.65 V to 1 V vs. MMS (in the case of Pt),

and -0.4 V to 0.4 V (in the case of Pd) at a scan rate of 10 mV $s^{-1}$. The second scan was subtracted from the first one using the GPES software.

# 2. CV characteristics of the core–shell catalysts

## 2.1 Pt modified Au catalysts

Before analysing the Pt modified Au catalysts, the CV features of a 20 wt % Pt on Vulcan carbon powder from JMTC (particle size 3.2 nm) was studied.

### 2.1.1 Voltammetric features of the 20 wt % Pt/C

Figure 5-4 represents the CV of 20 wt % Pt/C in $N_2$ saturated 1 mol $dm^{-3}$ $H_2SO_4$.

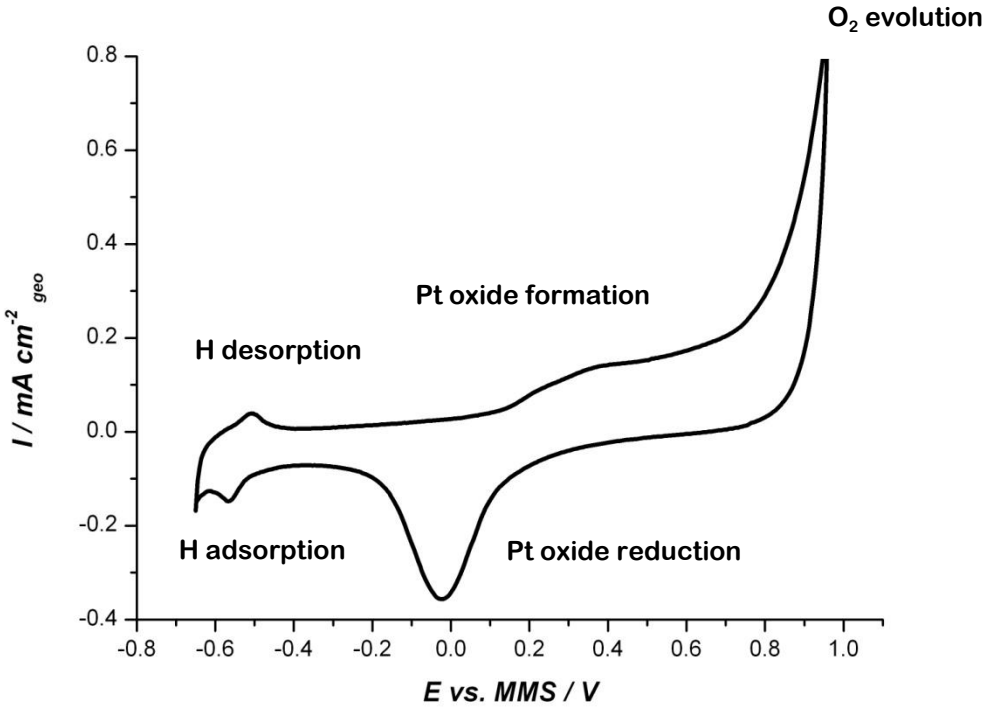


**Figure 5-4: CV of 20 wt % Pt / C on GC electrode (5 mm diameter) electrode in 1 mol $dm^{-3}$ $H_2SO_4$ deoxygenated with $N_2$. Scan rate 20 mV $s^{-1}$.**

Three distinct regions were observed including the double layer region.

**(a) H region (-0.7 V to -0.4 V)**

$$Pt + H^+ + e^- \leftrightarrow Pt - \mathrm{H_{ads}} \quad \textbf{[5-3]}$$

The forward scan represents the desorption of H from the Pt surface and the reverse scan represents the adsorption of H on to the Pt surface. The peak position correlates with the relative strength of the hydrogen adsorption. The area under the hydrogen adsorption peaks is used to calculate the Pt surface area as hydrogen will adsorb to complete a full monolayer on Pt surfaces[11]. At -0.7 V $H_2$ evolution begins.

**(b) Oxide region (0.3 V to 0.8 V)**

$$Pt + H_2O \leftrightarrow Pt - OH_{ads} + H^+ + e^- \quad \textbf{[5-4]}$$

$$Pt - OH_{ads} \leftrightarrow PtO + H^+ + e^- \quad \textbf{[5-5]}$$

Oxide formation starts around 0.3 V. When the Pt surface has been saturated with a monolayer of oxide, Pt continues to form oxides and then a multilayer is formed due to the place exchange mechanism[12]. On the reverse scan, the peak at ~ 0 V is the reduction of the oxide peak. The peak position and the area under this peak depend on the length of time spent in the oxide region and the upper potential limit of the voltammogram. Oxygen evolution begins at ~ 0.8 V.

CO stripping method is an important method for the analysis of atomic surface structure of the catalyst. When a monolayer of CO is adsorbed on to the surface a remarkable change in the CV is observed (Figure 5-5). The first and second scans were plotted on the same graph to see the difference between them.

The stripping of CO can be explained using the following Equation

$$Pt - CO + H_2O \rightarrow Pt + CO_2 + 2H^+ + 2e^- \quad \textbf{[5-6]}$$

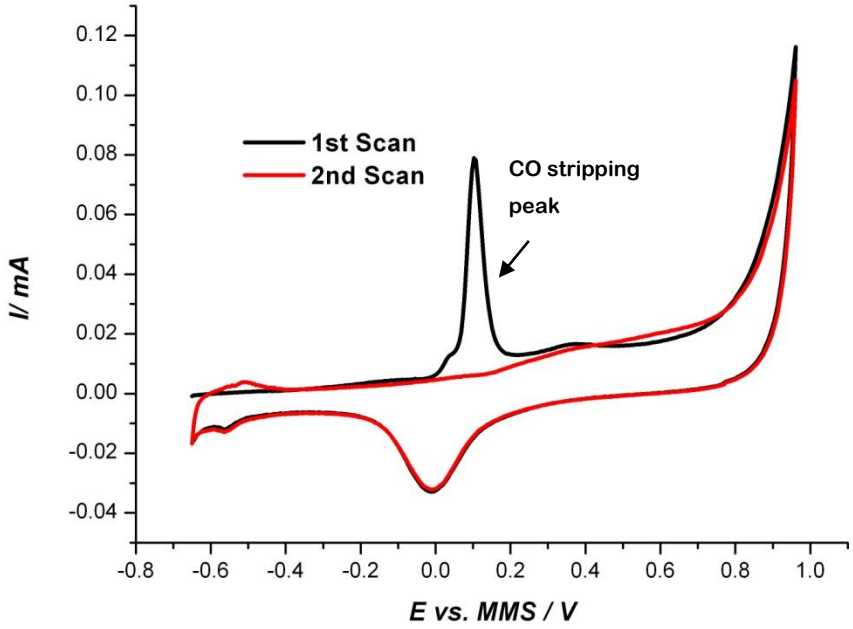


**Figure 5-5: CO stripping CVs of 20 wt % Pt/C on GC electrode (5 mm diameter) electrode in 1 mol dm$^{-3}$ $H_2SO_4$. First and second scans are shown. Scan rate 10 mV s$^{-1}$.**

CO binds strongly with Pt. Consequently it blocks the adsorption sites for hydrogen. Therefore in the first forward (positive going) scan, the H desorption peak is not visible. However the adsorption peak is visible in the reverse (negative going) scan. This is due to the available Pt sites after CO oxidation. At ~ 0.1 V the oxidation of CO to $CO_2$ occurs. After that the surface is available for oxide formation (forward scan) and reduction (reverse scan). Once the CO has been removed from the Pt surface (second scan) the CV feature is similar to the CV observed in Figure 5-4.

As CO adsorption on a Pt surface is limited to single monolayer coverage, the area under the CO adsorption peak can be used to determine the available Pt surface area. The charge coupled with a monolayer of CO on a Pt surface is 420 μC cm$^{-2}$ Pt[13]. The active surface area of Pt is the ratio between the charge under the CO oxidation and the constant charge for a monolayer of CO on a cm$^2$ of Pt (Equation 5-7).

$$Pt_{real\ area} = \frac{Charge\ under\ the\ CO\ stripping\ peak\ /\mu C}{420\ \mu C\ cm^{-2}\ Pt} \quad \textbf{[5-7]}$$

## 2.1.2 Voltammetric features of the Pt modified Au catalysts

Figure 5-6 shows the recorded CVs of the Pt modified Au catalysts in $N_2$ saturated 1 mol $dm^{-3}$ $H_2SO_4$ on RDE. The current was normalized by the Au real surface area before Pt deposition.

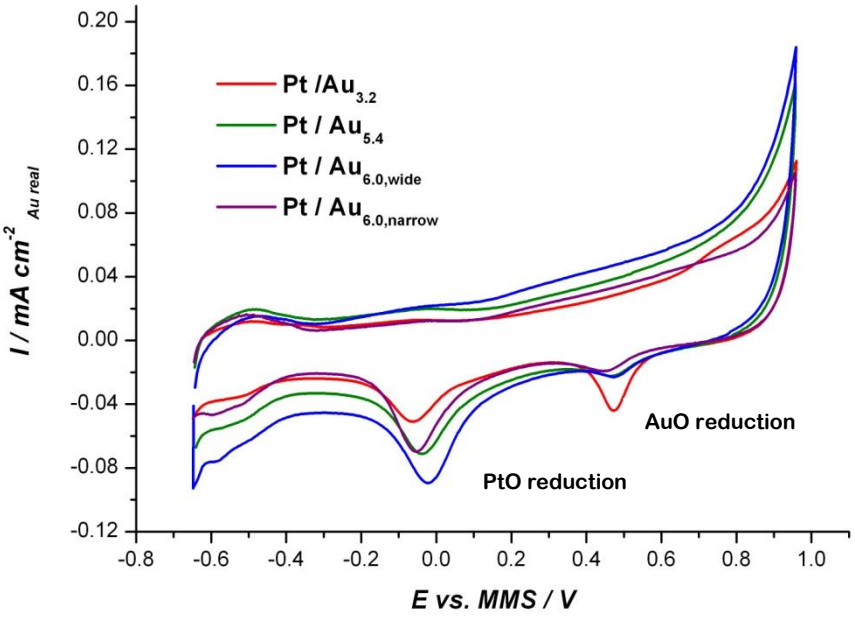


**Figure 5-6: CV curves of the Pt modified Au catalysts on GC disc (5 mm diameter) electrode in 1 mol $dm^{-3}$ $H_2SO_4$ deoxygenated with $N_2$. Scan rate 20 mV $s^{-1}$.**

The CV consists of a hydrogen adsorption-desorption region (-0.7 V to -0.4 V) as well as Pt and Au oxide formation/reduction regions. The reduction of Au oxide is observed at ~ 0.5 V and the reduction of Pt oxide is seen at ~ 0 V. Appearance of the Au oxide reduction peak indicates that the Pt ad-layer is not a complete monolayer (not a pure epitaxial growth) and some of the Au sites are still exposed. There can be two reasons for the incomplete monolayer of Pt. Either the Cu does not form a complete monolayer on Au (This is proved that it only gives around half the

total area of the gold for the oxide stripping) or the Pt replacement with Cu is not 100% efficient. However, the amount of Au remaining was shown to decrease as Pt coverage increased, i.e. the Au oxide reduction current decreased while the Pt oxide reduction current increased as the amount of Pt increased. This suggests that the Pt atoms are selectively deposited on Au catalysts and not on the carbon[14].

A rough estimation of the Pt coverage can be made from the H region as well as Pt oxide reduction peak. It is very clear that the amount of Pt deposited increases with increasing the size of Au core.

The peak position of the Pt modified Au catalysts are tabulated in Table 5-1.

**Table 5-1: Cyclic voltammetric parameters of the Pt modified Au catalysts.**

| Pt modified Au catalysts | Pt oxide stripping peak / V |
|---|---|
| $Pt/Au_{3.2}$ | -0.06 |
| $Pt/Au_{5.4}$ | -0.04 |
| $Pt/Au_{6.0,wide}$ | -0.02 |
| $Pt/Au_{6.0,narrow}$ | -0.05 |

As the amount of Pt increased, Pt oxide reduction peak is shifted to a less negative potential value. This is an indication that the oxygen species bind more strongly to the Pt on the Pt modified Au catalysts when the amount of Pt decreases. This observation was clarified by Noel Kristan and coworkers[2]. They considered that the chemical potential of a metal could be viewed as the work function. The work function values of Pt and Au are 5.40 and 5.32 respectively. When the Pt and Au are in contact with each other there will be a flow of electrons from Au to Pt until the chemical potentials are equal in both the metals. At lower coverage of Pt, the Pt on Au surface has more negative charge per atom and therefore a more negative potential would be needed for the Pt oxide reduction. In other words, the bond between the Pt and O is stronger at lower coverage of Pt. This is also explained by Norskov *et al.*[15] using a *d* – band model. They concluded that when the Pt monolayer

is deposited on Au there will be an upwards shift in the *d*-band centre and this leads to higher adsorption energies for oxygen containing species.

The CO stripping voltammogram of the Pt modified Au catalysts in 1 mol $dm^{-3}$ $H_2SO_4$ on RDE are represented in Figure 5-7.

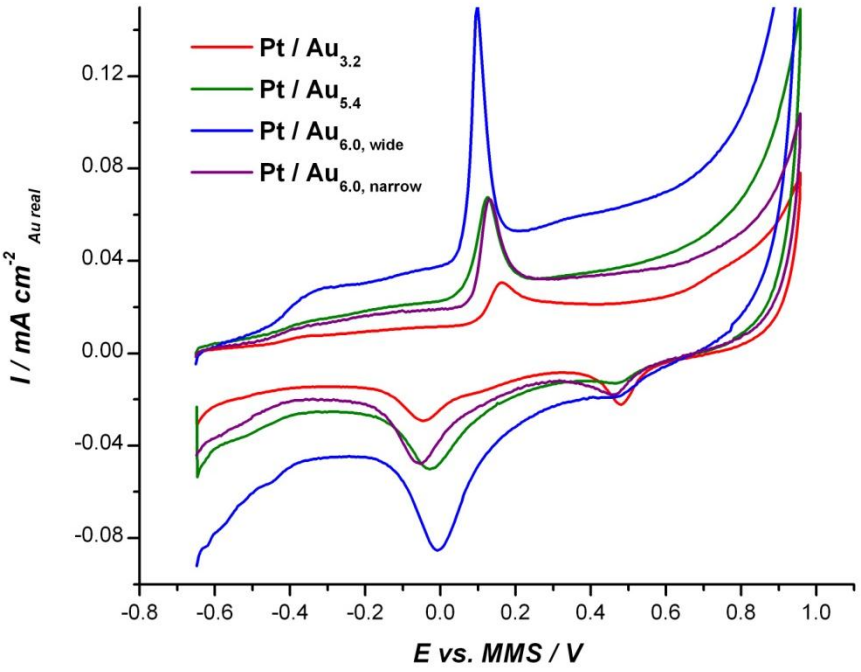


**Figure 5-7: CO stripping CVs of the Pt modified Au catalysts on GC electrode (5 mm diameter) in 1 mol $dm^{-3}$ $H_2SO_4$. Only the first scan is shown. Scan rate 10 mV $s^{-1}$.**

There was no detectable CO peak observed on the Au/C catalysts (not shown). Therefore all CO peaks shown here can be assigned to CO adsorption on Pt sites. CO stripping peak is observed at ~ 0.1 V, and a smaller/broad peak at ~ -0.4 V corresponding to the onset of CO oxidation for all the catalysts. The positions of the CO peak and as well as the ratio of the Pt real surface area (based on the CO stripping peak area using Equation 5-6) to the Au real surface area before the Pt deposition(based on the Au oxide stripping peak) are tabulated in Table 5-2.

**Table 5-2: CO stripping parameters of the Pt modified Au catalysts.**

| Catalyst | Position of CO peak / V | Ratio of Pt real area to the Au real area / Pt:Au |
|---|---|---|
| Pt /$Au_{3.2}$ | 0.16 | 0.46 |
| Pt/$Au_{5.4}$ | 0.12 | 0.82 |
| Pt/$Au_{6.0,wide}$ | 0.10 | 0.94 |
| Pt/$Au_{6.0,narrow}$ | 0.12 | 0.70 |

It is clearly seen from the Table 5-2, that the ratio of Pt real area to the Au real area generally increases with increasing size of Au with the exception of Pt /$Au_{6.0,\ narrow}$. When comparing Figures 5-5 and 5-7, the CO oxidation on 20 wt % Pt/C is slightly more negative than the Pt modified Au catalysts. This is due to the tensile strain induced by Au which strengthens the Pt–CO bond and as a result the oxidation potential increases[16]. The Pt modified Au catalysts display Pt coverage dependent peak positions, shifting to more negative values for larger sizes of Au compared to the smaller ones. The oxidative removal of CO on Pt sites mostly depends on the availability of active oxygen species on the neighbouring sites. At higher coverage of Pt, the water activation begins at more negative potential (Figure 5-6) and hence facilitates the CO oxidation[17].

# 2.2 Pd modified Au catalysts

## 2.2.1 Voltammetric features of the 20 wt % Pd/ C

A CV of a 20 wt % Pd on Vulcan carbon powder from JMTC in $N_2$ saturated 1 mol $dm^{-3}$ $H_2SO_4$ on RDE is presented in Figure 5-8.

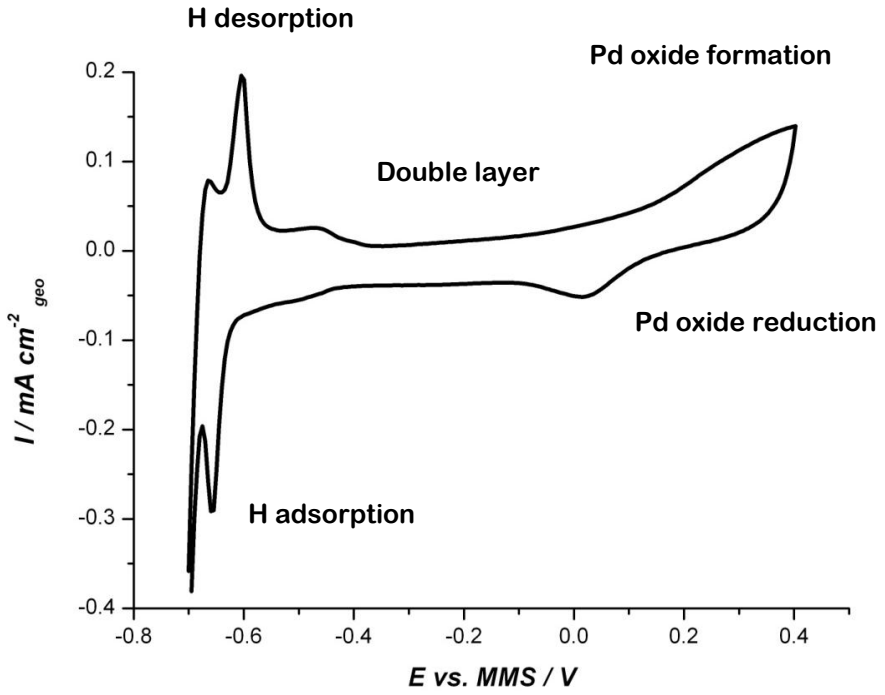


**Figure 5-8: CV of 20 wt % Pd/C on GC electrode (5 mm diameter) electrode in 1 mol dm$^{-3}$ $H_2SO_4$, deoxygenated with $N_2$. Scan rate 20 mV s$^{-1}$.**

Due to the solubility of Pd oxide in the $H_2SO_4$ solution, the anodic potential was limited to 0.4 V vs. MMS. As seen in the Figure, the CV of Pd is similar to that of Pt. The Pd CV also has a H adsorption/desorption region (-0.7 V to -0.5 V) and a Pd oxide formation/reduction region (-0.1 V to 0.4 V). A small peak at ~ -0.5 V could be due to an additional hydride peak, but may also be associated with contributions from $HSO_4^-$ and $SO_4^{2-}$ adsorption[18].

Anodic stripping voltammetry was used to study the electro-oxidation of adsorbed CO. Figure 5-9 shows the CO stripping of 20 wt % Pd/C catalyst in 1 mol dm$^{-3}$ $H_2SO_4$.

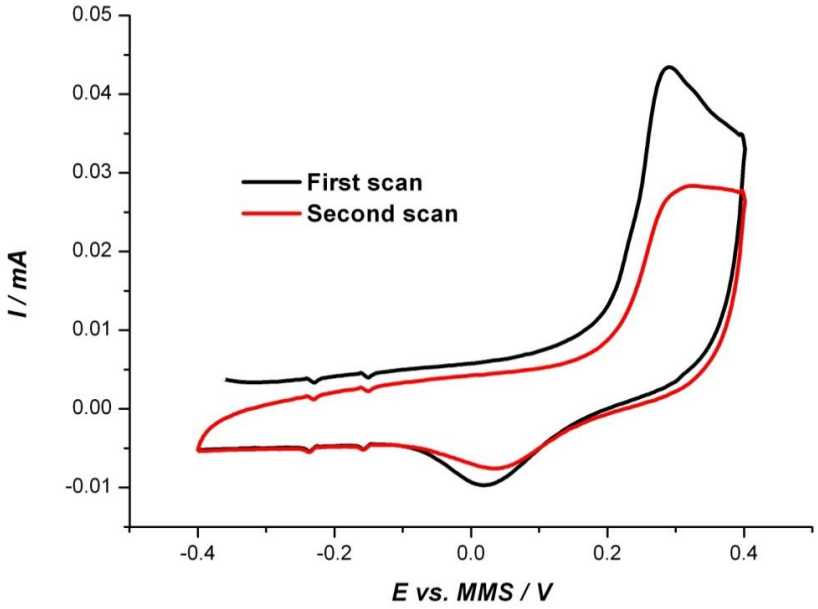


**Figure 5-9: CO stripping CVs of 20 wt % Pd / C on GC electrode (5 mm diameter) electrode in 1 mol dm$^{-3}$ $H_2SO_4$. First and second scans are shown. Scan rate 10 mV s$^{-1}$.**

Unlike Pt, the Pd CO stripping peak coincides with the onset of oxide formation. The first scan corresponds to a combination of CO stripping, Pd surface oxidation, and anion adsorption. In the second scan the entire CO has been oxidized as a result the subtraction of second scan from the first scan will give the CO stripping charge.

Similar to Pt, the charge under the CO stripping peak was used to determine the electroactive area of Pd. It is considered that the dominant adsorption site is the bridge binding site with a CO: Pd ratio of 1:2[19].
The stripping of CO can be explained using the following Equation

$$(CO)Pd_2 + H_2O \rightarrow 2Pd + CO_2 + 2H^+ + 2e^- \quad \textbf{[5-8]}$$

Since one electron is involved per one Pd atom the real area of Pd will be given as,

$$Pd_{real\ area} = \frac{Charge\ under\ the\ CO\ stripping\ peak\ /\mu C}{210\ \mu C\ cm^{-2}\ Pd} \quad \textbf{[5-9]}$$

## 2.2.2 Voltammetric features of the Pd modified Au catalysts

CVs were performed on RDE with the solution of $N_2$ saturated 1 mol $dm^{-3}$ $H_2SO_4$ to obtain the surface composition and characteristics of the Pd modified Au catalysts and the results are shown in Figure 5-10.

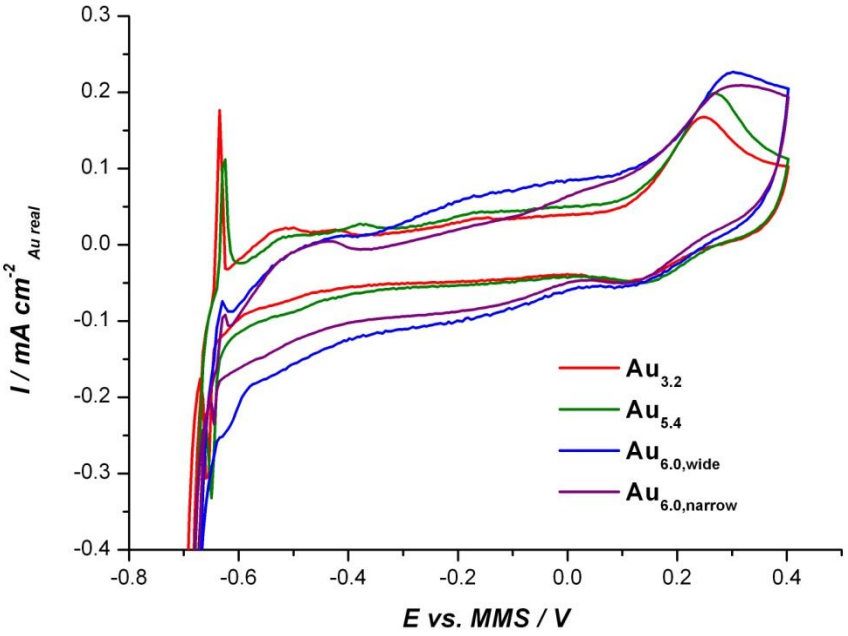


**Figure 5-10: CV curves of the Pd modified Au catalysts on GC disc (5 mm diameter) electrode in 1 mol $dm^{-3}$ $H_2SO_4$, deoxygenated with $N_2$. Scan rate 20 mV $s^{-1}$.**

The reduction of gold oxide is not seen due to the limitation of the anodic potential. The H region observed in the potential region -0.6 V to -0.7 V is the indication of the deposition of Pd on Au surfaces. Unlike the Pt modified Au catalysts, the hydrogen region is not clear. This may be due to the Pd dissolution in acidic media. However, similar to Pt, Pd also shows size dependent activity. Higher loading of Pd is observed on the larger size of Au. The oxide reduction current density of the catalysts clearly shows this size dependent activity.

Figure 5-11 shows the CO stripping scans for the Pd modified Au catalysts in 1 mol $dm^{-3}$ $H_2SO_4$.

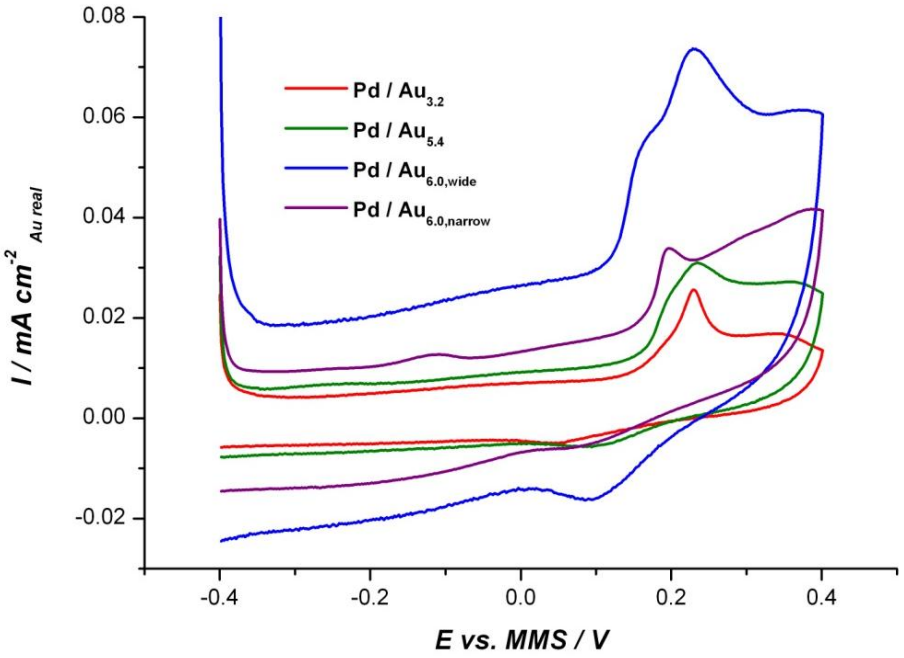


**Figure 5-11: CO stripping CVs of the Pd modified Au catalysts on GC electrode (5 mm diameter) in 1 mol $dm^{-3}$ $H_2SO_4$. Only the first scan is shown. Scan rate 10 mV $s^{-1}$.**

As seen in the Figure 5-11, the Pd modified Au catalysts display a size dependent activity towards the CO oxidation. Compared to Pt modified catalysts, the peaks for CO oxidation are broader. This may be due to the overlap of Pd oxidation and the CO stripping.

The CO peak positions as well as the calculated real surface area of Pd (using Equation 5-9) with respect to the Au real area are tabulated in Table 5-3.

**Table 5-3: CO stripping parameters of the Pd modified Au catalysts.**

| Catalyst | Position of CO peak / V | Pd real area to the Au real area / Pd:Au |
|---|---|---|
| Pd / $Au_{3.2}$ | 0.23 | 0.52 |
| Pd / $Au_{5.4}$ | 0.23 | 0.70 |
| Pd / $Au_{6.0,wide}$ | 0.22 | 0.92 |
| Pd / $Au_{6.0,narrow}$ | 0.19 | 0.84 |

According to Table 5-3, it is apparent that there is no clear difference in the CO peak positions on the above catalysts except for the $Pd/Au_{6.0,\ narrow}$ catalyst. There is a noticeable difference in the ratio of Pd real area to the Au real area with the size of Au. The ratio increases with increase in the size of Au. This result is in excellent agreement with the Pt modified Au catalysts.

# 3. Oxygen Reduction Reaction (ORR)

Pt or Pd modified Au catalysts dispersed on high surface area of carbon have been shown to exhibit superior activity for oxygen reduction[5,10,20]. In this work the oxygen reduction was investigated on Pt or Pd modified Au catalysts and the results will be compared to those on monatomic catalysts (i.e. Pt/C, Pd/C and Au/C). Emphasis will be placed on the effects of Pt or Pd coverage per $cm^2$ Au core.

## 3.1 ORR on 20 wt % Pt / C

Most of the recent investigations of ORR at Pt have been in acidic media but there is increasing interest in alkaline solutions as well[21,22]. The mechanism of oxygen reduction on Pt is mainly a 4 e-process. But it can be either a direct four $e^-$ reduction or 2- step four $e^-$ reduction. Once again much of the focus on the fundamental side has been on studies of single crystal electrode surfaces.

The rotating disc experimental measurements of the oxygen reduction on 20 wt % Pt/C (particle size 3.2 nm) were performed on RDE in $O_2$ saturated 0.5 mol $dm^{-3}$ KOH solution at a scan rate of 10 mV $s^{-1}$ and the current as a function of rotation rate is represented in Figure 5-12.

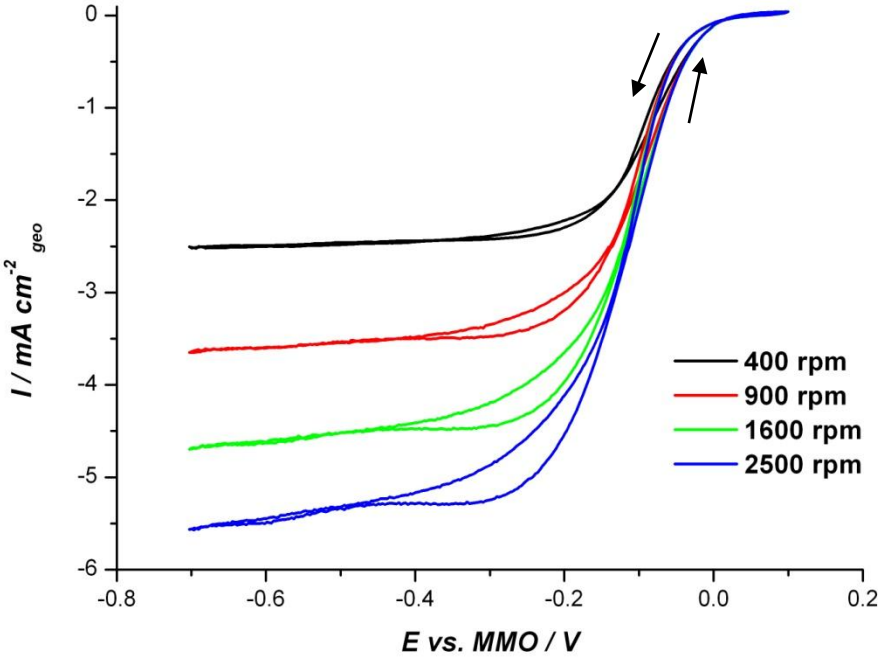


**Figure 5-12: $O_2$ reduction polarisation curves on 20 wt % Pt/C on GC disc (5 mm diameter) in $O_2$ saturated 0.5 mol $dm^{-3}$ KOH. Scan rate 10 mV $s^{-1}$.**

The onset of oxygen reduction potential starts at ~ 0 V vs. MMO the mixed region was observed at potential between 0 V and -0.2 V and beyond -0.2 V the current is predominantly mass transport controlled. There is a little hysteresis between the forward and the backward scans and this increase with increasing scan rate. This may be explained as a change in activity between reduced and the oxidized Pt with the reduced Pt being more active.

Figure 5-13 represents the potential dependence of the specific activity. The Pt real surface area was calculated using the charge under the CO stripping peak.

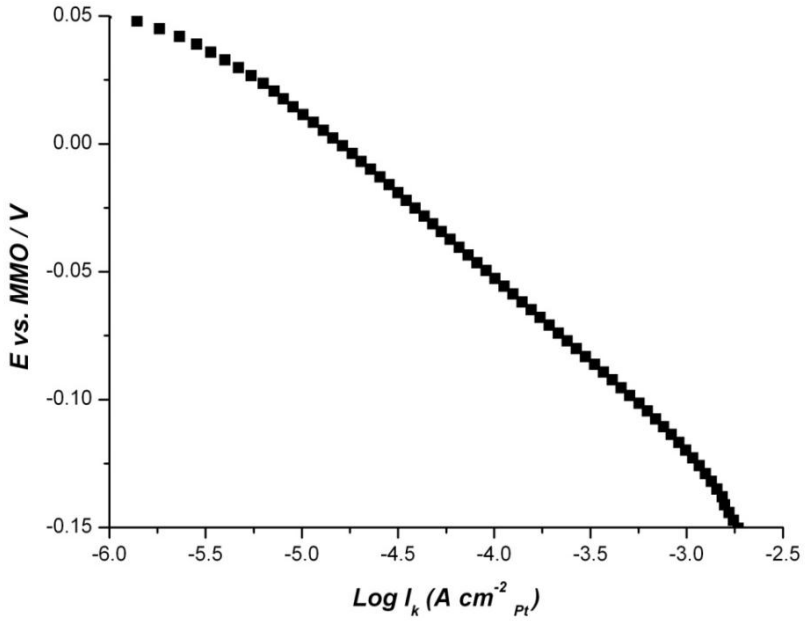


**Figure 5-13: Tafel plot corresponding to the data obtained at 900 rpm in Figure 5-12.**

The SA value obtained for 20 wt % Pt / C at -0.06 V is 138 µA $cm^{-2}_{Pt}$. However the SA value reported by Genies *et al.*[21] for 20 wt % Pt / C in 1 mol $dm^{-3}$ NaOH is 97 µA $cm^{-2}_{Pt}$. The difference in activity might be attributed to the use of lower concentration of KOH in the study reported here compared to NaOH used by Genies *et al*. Due to the variations in size of the $Na^+$ and $K^+$ cations, the oxygen solubility, viscosity and the diffusion coefficient of oxygen differs. Jin *et al.*[24] explained that this enhanced activity in KOH solution is mainly due to the increase in mass transport of oxygen, which is generally governed by the oxygen solubility and the diffusion coefficient. Jin and coworkers also observed a concentration dependent oxygen reduction activity in the above solutions. They noticed an increase in the current density and a positive shift for the onset of oxygen reduction at lower concentrations of electrolytes.

# 3.2 ORR on Pt modified Au catalysts

Polarisation curves for the ORR obtained using a RDE at several rotation rates on Pt modified Au/C catalysts in $O_2$-saturated 0.5 mol $dm^{-3}$ KOH are presented in Figure 5-14.

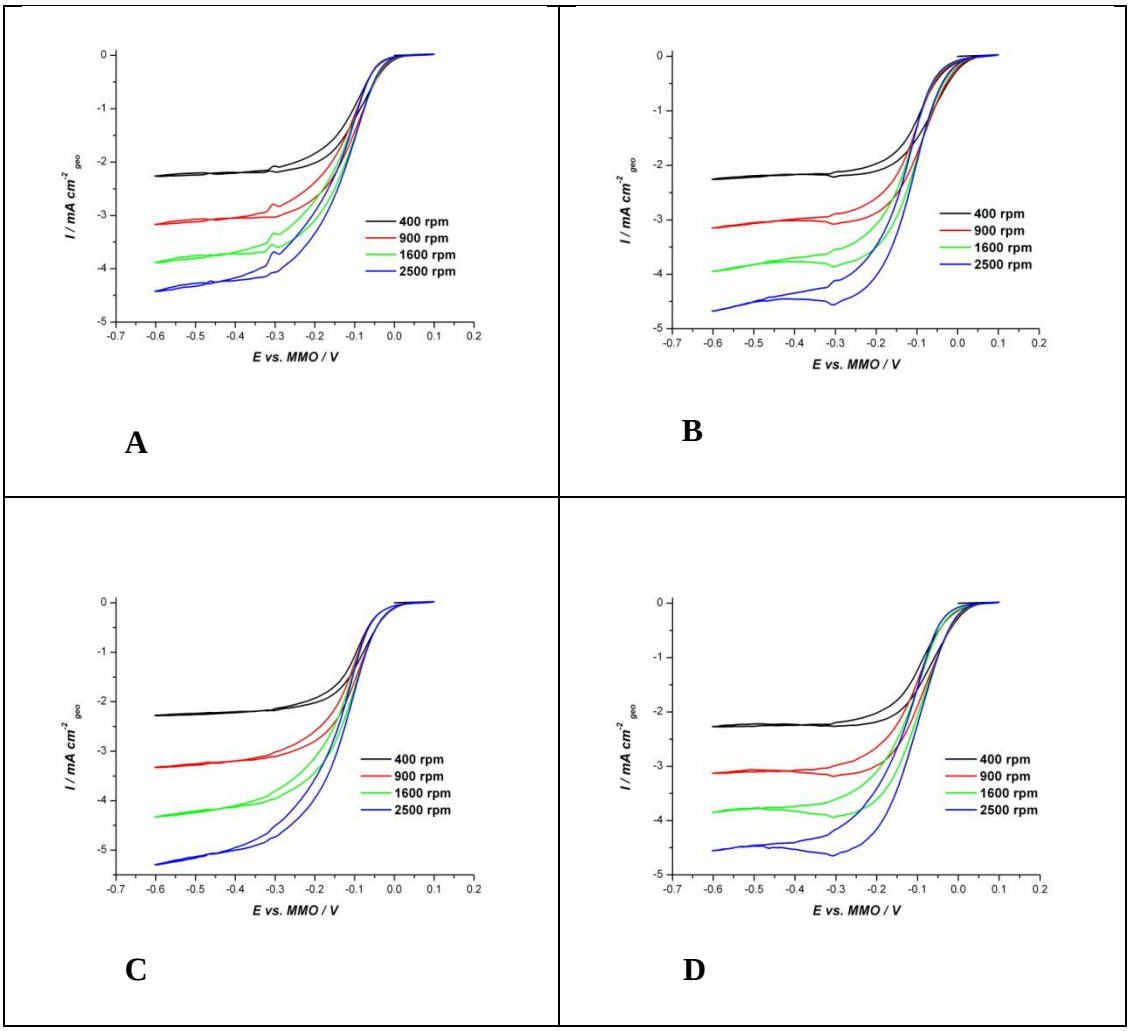


**Figure 5-14: Oxygen reduction rotating disc voltammograms of the Pt modified Au/C catalysts (A) $Pt/Au_{3.2}$, (B) $Pt/Au_{5.4}$, (C) $Pt/Au_{6.0,wide}$ and (D) $Pt/Au_{6.0,narrow}$ on GC electrode (5 mm diameter) in $O_2$ saturated 0.5 mol $dm^{-3}$ KOH. Scan rate 10 mV $s^{-1}$.**

Single $O_2$ reduction sigmoidal curves and well defined plateaus in the mass transport controlled region were observed. As explained in section 2.1.2, the Pt ad-layer on the Au surface is not a complete monolayer. As a result there will be some exposed Au and this will also take part in ORR. Therefore the current obtained in oxygen reduction is the total current from the oxygen reduction on Pt and Au.

The ORR curves from the Pt modified Au catalysts at 900 rpm are presented in Figure 5-15. The plot for the 20 wt % Pt/C is also incorporated for the sake of comparing the efficiency of ORR activity.

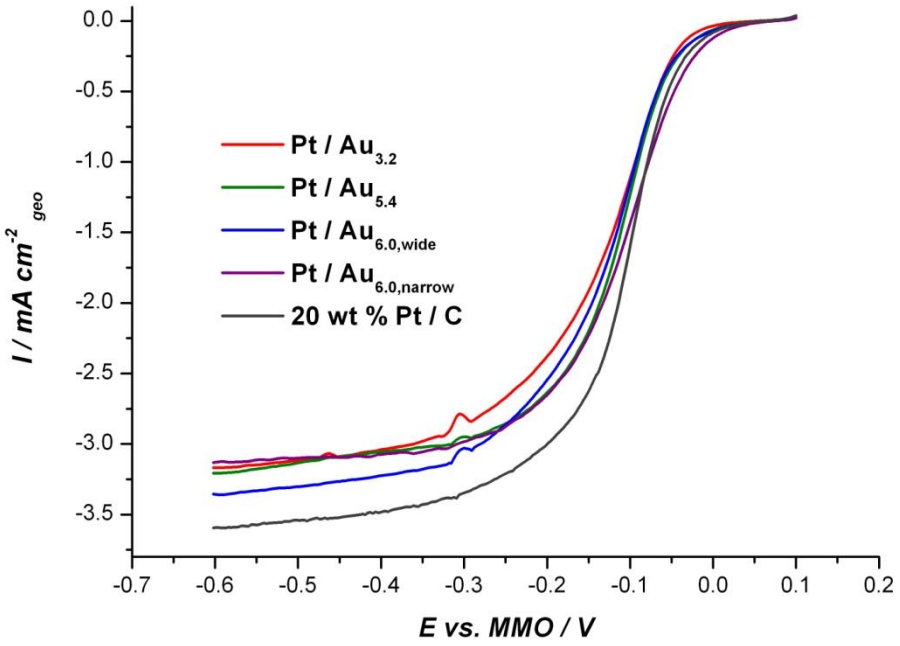


**Figure 5-15: ORR on Pt modified Au catalysts and the 20 wt % Pt/C on GC electrode (geometric area 0.196 $cm^2$).in oxygen saturated 0.5 mol $dm^{-3}$ KOH at 900 rpm. Scan rate 10 mV $s^{-1}$. Only the negative going scans were selected.**

The onset potential for ORR at all the catalysts is ~ 0 V. From 0 V to -0.3 V, the process is under mixed kinetic and diffusion control. Beyond -0.3 V it is almost purely mass transport controlled. It is also noted that the ORR limiting current values of the Pt modified Au catalysts were close for Pt/C catalyst. This indicates that the ORR reaction on the modified catalysts follows mainly the 4-electron pathway.

To compare the oxygen reduction activity on these different Pt modified Au catalysts and the 20 wt % Pt/C, the current was normalized by the real area of Pt obtained from the CO stripping CVs, and current density *vs.* the potential was plotted (Figure 5-16). However due to an incomplete monolayer coverage of Pt there were some exposed Au atoms as well, which may be a source of error in the measurements.

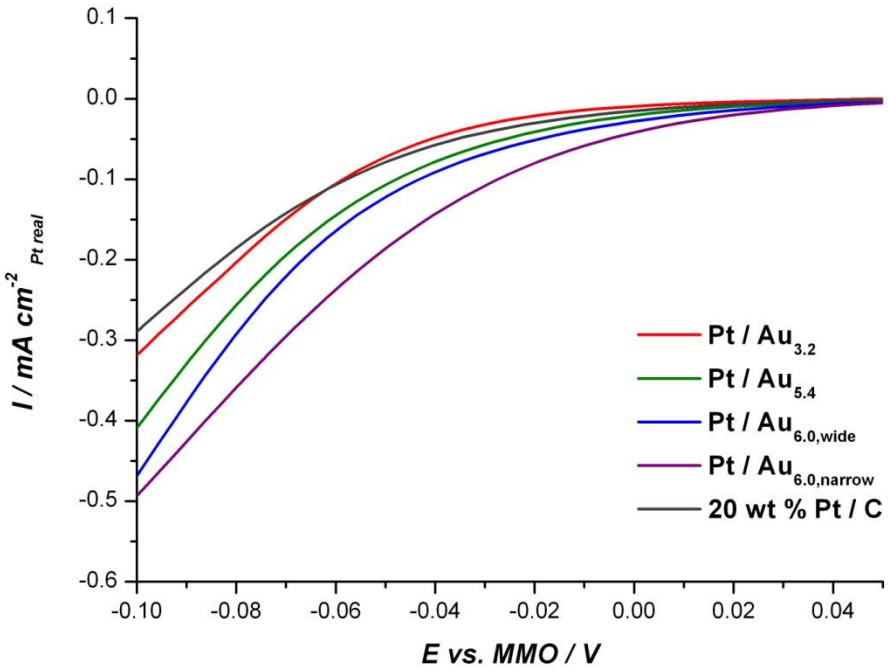


**Figure 5-16: ORR on Pt modified Au catalysts and 20 wt % Pt/C catalyst on GC electrode (geometric area 0.196 $cm^2$).in oxygen saturated 0.5 mol $dm^{-3}$ KOH at 900 rpm. Scan rate 10 mV $s^{-1}$. Only the negative going scans around the activation controlled region were selected. The current was normalized by the Pt real area.**

The onset potential for the oxygen reduction is tabulated in Table 5-4.

**Table 5-4: Oxygen reduction polarisation parameters of the Pt modified Au catalysts and the 20 wt % Pt/C.**

| Catalyst | Onset potential of oxygen reduction at -10 µA $cm^{-2}_{Pt}$/ V |
|---|---|
| $Pt/Au_{3.2}$ | 0.004 |
| $Pt/Au_{5.4}$ | 0.018 |
| $Pt/Au_{6.0,\ wide}$ | 0.027 |
| $Pt/Au_{6.0,\ narrow}$ | 0.036 |
| 20 wt % Pt/C | 0.004 |

It has been previously reported in Table 5-2 that on the larger Au particles there was a greater coverage of Pt compared to smaller particles. It is clearly seen in Table 5-4

that when the Pt coverage increases the onset of oxygen reduction shifted to more positive potential. The positive shift of onset potential is also evidenced by facile removal of oxide from the Pt as shown in Table 5-1. The onset potential of 20 wt % Pt/C is similar to $Pt/Au_{3.2}$ and it shows lowest current density amongst the Pt modified catalysts. Consequently there will be some influence from Au that enhances the oxygen reduction activity.

Figure 5-17 shows the Tafel plot corresponding to the specific activity of each of the Pt modified Au catalysts and the 20 wt % Pt/C.

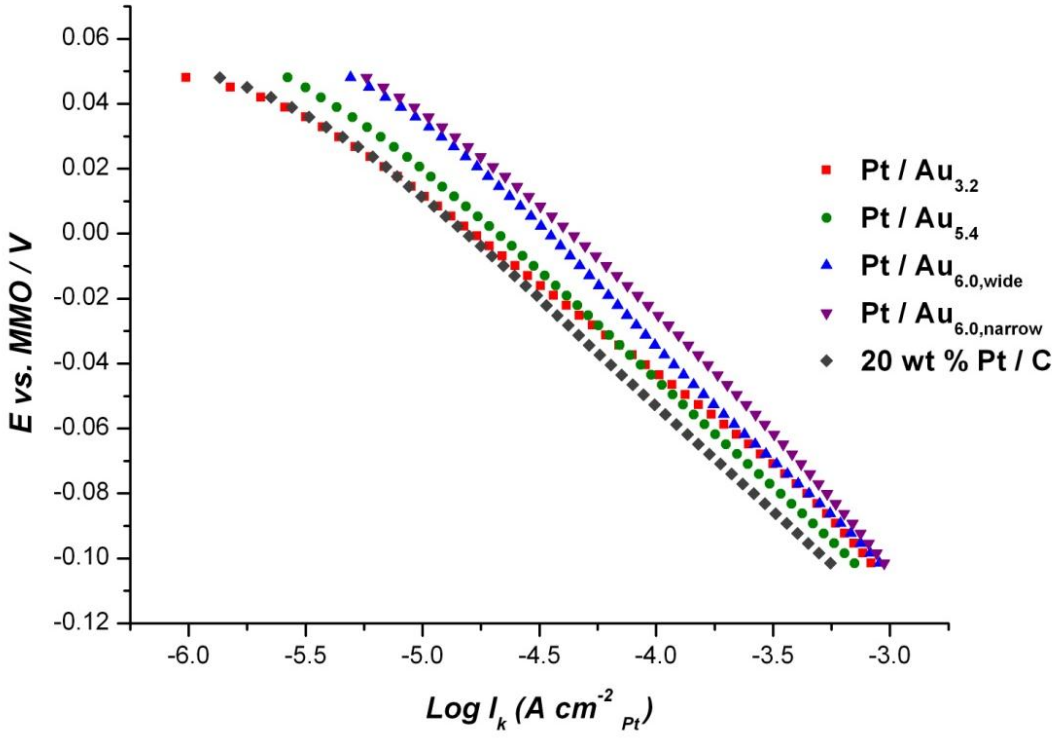


**Figure 5-17: Tafel plot for Pt modified Au catalysts and the 20 wt % Pt/C in oxygen saturated 0.5 mol $dm^{-3}$ KOH at 900 rpm.**

From the Tafel plot, the SA values of the Pt modified Au catalysts and 20 wt % Pt/C catalysts were determined at -0.03 V vs. MMO and tabulated in Table 5-5. For the sake of comparing the effect of Pt over-layer towards the ORR, SA values of the corresponding Au/C catalysts are also included.

**Table 5-5: Kinetic parameters of oxygen reduction on Pt modified Au catalysts, 20 wt % Pt/C and Au catalysts in 0.5 mol dm$^{-3}$ KOH at rotation speed 900 rpm.**

| Pt Catalysts | SA at -0.03 V / μA cm$^{-2}$ $_{Pt}$ | Au Catalysts | SA at -0.03 V / μA cm$^{-2}$ $_{Au}$ |
|---|---|---|---|
| Pt/Au$_{3.2}$ | 61 | Au$_{3.2}$ | 9 |
| Pt/Au$_{5.4}$ | 62 | Au$_{5.4}$ | 25 |
| Pt/Au$_{6.0, wide}$ | 90 | Au$_{6.0, wide}$ | 26 |
| Pt/Au$_{6.0, narrow}$ | 125 | Au$_{6.0, narrow}$ | 33 |
| 20 wt % Pt/C | 46 | | |

It is worth noticing that the specific activities are increasing with increase in coverage of Pt which is proportional to the size of the catalyst. There are several reasons for the increased activity on larger Pt particles. Usually on smaller particles a larger overpotential is needed to drive the reaction. Furthermore, Hydroxyl ion adsorption is a critical parameter in determining the activity of Pt. It has been reported that on smaller particles a higher degree of hydroxyl ion adsorption is observed due to its oxophilic nature and this blocks the active sites for the adsorption of oxygen; in addition to that smaller particles of Pt can be easily oxidized to PtO which is inactive for ORR[25].

Moreover, the above results also show the superior specific activity of the Pt over-layer catalysts compared to the Au catalysts and the 20 wt % Pt/C. There are various explanations for the enhancement of electroactivity of Pt modified Au catalysts. Luo *et al.*[26] who worked on Au-Pt bimetallic catalysts stated that the oxygen reduction on the Au-Pt surface occurs through a synergetic mechanism. In general hydroxyl ion adsorption on the Pt surfaces inhibits the oxygen reduction by blocking the active sites of Pt for the adsorption of oxygen. However adding Au will overcome this problem. Au promotes oxygen reduction on the Pt surface by forming Au–OH bonds that reduces the Pt–OH formation by lateral repulsion between the OH on Pt and the OH on Au. Luo *et al.* believed that the increase in activity is the cooperation of activation of Pt via the oxygen dissociation and promotion of Au site by hydroxyl adsorption. They proposed a model to explain this behaviour for a

bimetallic alloy. The Pt modified Au catalysts also have some Au sites exposed. Therefore that model may also be applicable for the Pt modified catalysts reported in this Chapter.

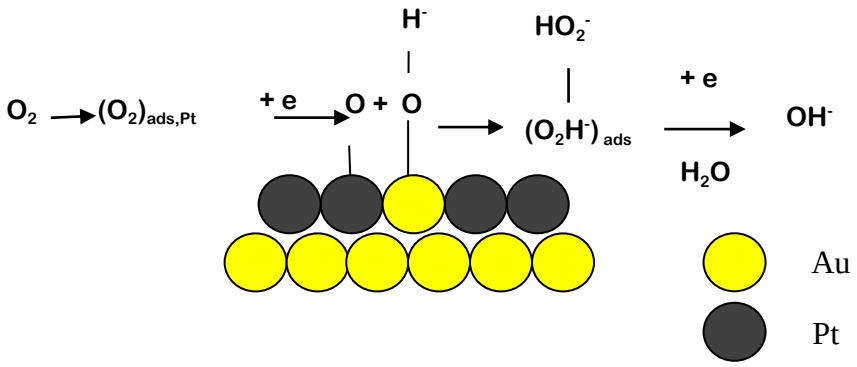


**Figure 5-18: Schematic diagram of synergetic oxygen reduction activity on Pt modified Au catalysts.**

As seen in Figure 5-18, adsorbed oxygen on Pt dissociates and forms a hydroxyl bond with Au; this results in the formation of $HO_2^-$ and facilitates the 4 e- reduction.

However the above conclusion is in contradiction with Vukmirovic and coworkers[27]. According to their view the bonding between the Au and OH is weak and consequently that will not promote the oxygen reduction on Pt.

Zhang *et al.*[28] claimed that the Au core in the core shell catalyst stabilizes the Pt surface under highly oxidizing conditions and prevents the dissolution of Pt during the reduction of oxygen. The stability of Au@Pt core shell catalysts was also explained by Xiaowei Li and coworkers using XPS measurements [29]. They observed an increase in binding energy for Pt modified Au/C catalysts compared to Pt/C catalysts. This variation in the oxidation state of the Pt shell accounts for the stabilization of the core shell catalysts.

The *d*-band vacancy of metal plays an important role in the process of oxygen reduction. As discussed in Chapter one, the activity of an ORR catalyst is related to the centre of the *d*-band (Norskov model)[30]. The *d*-band centre of the metal atoms on the surface of the catalyst particles can be modified by the layers below the surface[31]. This electronic effect is in addition to the lattice expansion in compression of the

monolayer (morphological effect). Such effects in the *d*-band centre have been studied by Zhang *et al.*[5] who reported that a tensile strain and an up shift in the *d*-band centre of Pt are observed when it is deposited on to an Au (111) facet. Hence Pt on Au is expected to be more active for ORR.

# 3.3 Pd modified catalysts

Even though the Pt based catalysts have been shown to demonstrate enhanced activity in the reaction of oxygen reduction they are not practical for large scale applications. Therefore currently Pd modified catalysts gained much more interest to reduce the cost of Pt[32-36].

## 3.3.1 ORR on 20 wt % Pd/C

Potentiodynamic polarisation curves for oxygen reduction currents obtained from 20 wt % Pd/C in $O_2$ saturated 0.5 mol $dm^{-3}$ KOH on RDE at scan rate 10 mV $s^{-1}$ is presented in Figure 5-19.

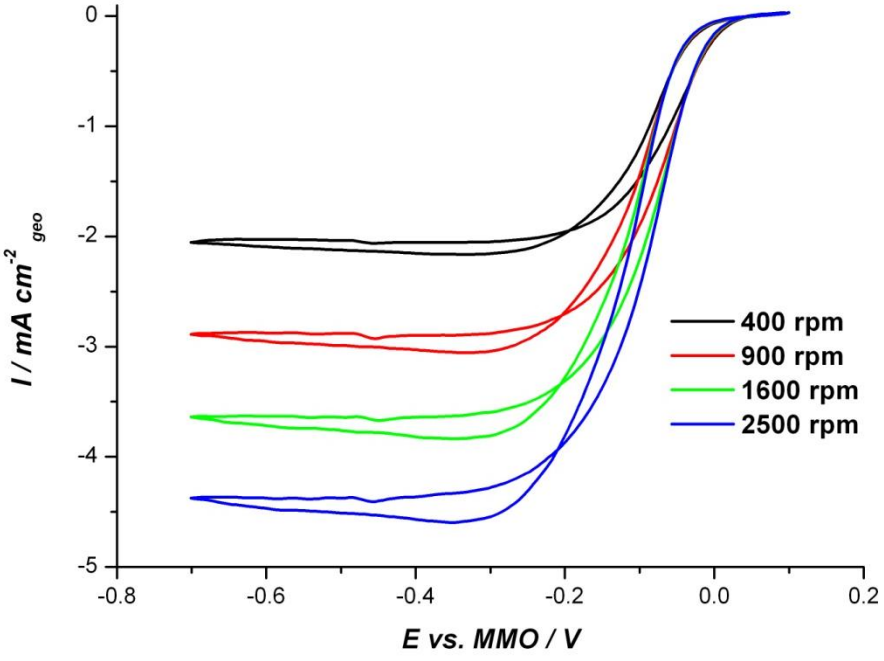


**Figure 5-19: $O_2$ reduction polarisation curves on 20 wt % Pd/C on GC disc (5 mm diameter) in $O_2$ saturated 0.5 mol $dm^{-3}$ KOH. Scan rate 10 mV $s^{-1}$.**

Single sigmoidal curves were observed for all rotation rates. The onset potential for oxygen reduction starts at ~ 0 V vs. MMO which is independent of the rotation speed, the mixed kinetic and diffusion controlled region was observed in the region from 0 V to -0.2 V and beyond -0.2 V, the ORR is diffusion controlled region.

The mass transport corrected Tafel plot at 900 rpm is given in Figure 5-20.

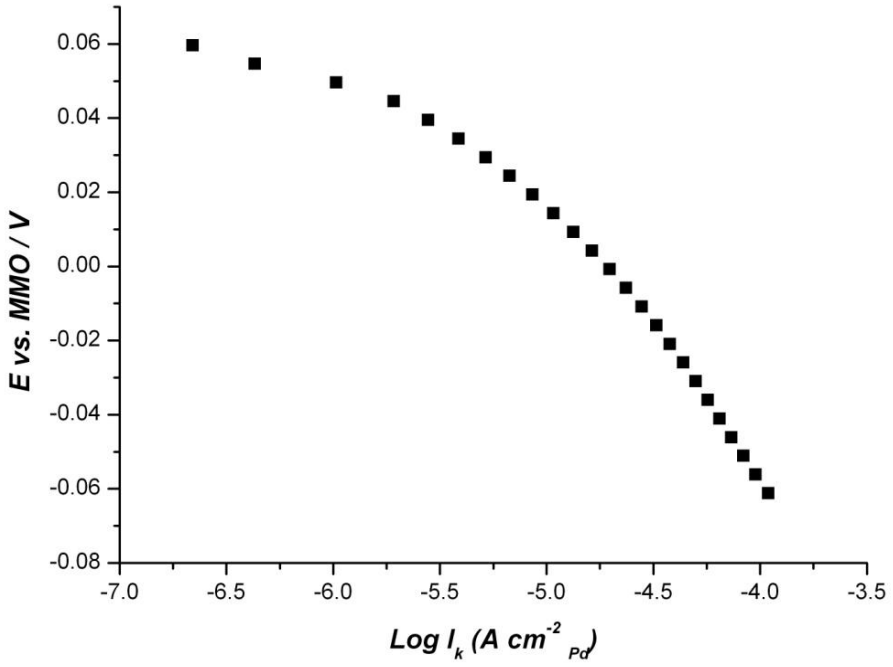


**Figure 5-20: Tafel plot corresponding to the data obtained at 900 rpm in Figure 5-21.**

The specific activity at -0.03 V vs. MMO is 50 μA $cm^{-2}_{Pd}$.

## 3.3.2 ORR on Pd modified Au catalysts

The ORR reaction changes when a monolayer of Pd is deposited on Au electrode. Oxygen reduction polarization curves on Pd modified Au catalysts in oxygen saturated 0.5 mol $dm^{-3}$ KOH at several rotation speeds are shown in Figure 5-21.

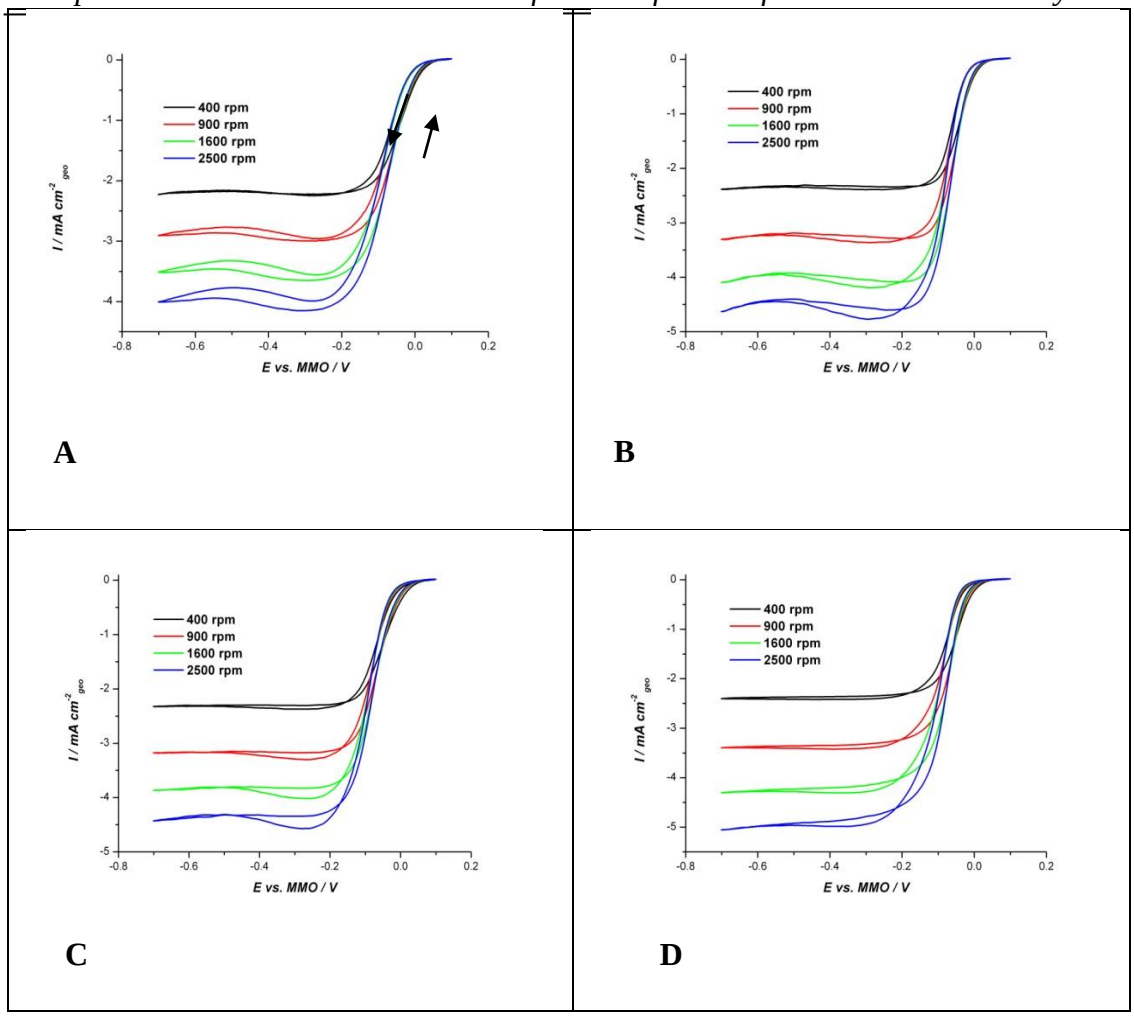


**Figure 5-21: Oxygen reduction rotating disc voltammogram of the Pd modified Au/C catalysts (A) $Pd/Au_{3.2}$, (B) $Pd/Au_{5.4}$, (C) $Pd/Au_{6.0,wide}$ and (D) $Pd/Au_{6.0,narrow}$ on GC electrode (5 mm diameter) in $O_2$ saturated 0.5 mol $dm^{-3}$ KOH. Scan rate 10 mV $s^{-1}$.**

Single sigmoidal curves were obtained for all the Pd modified Au catalysts. Well defined plateaus were observed at all the rotation rates for all the Pd modified Au catalysts indicating that the oxygen reduction is mass transport controlled. As explained in section 3.1.2 the Pd modified catalysts also have some Au sites exposed hence the current obtained during oxygen reduction is a sum of the reduction current on Pd as well as on Au.

The curves were compared at 900 rpm and presented in Figure 5-22.

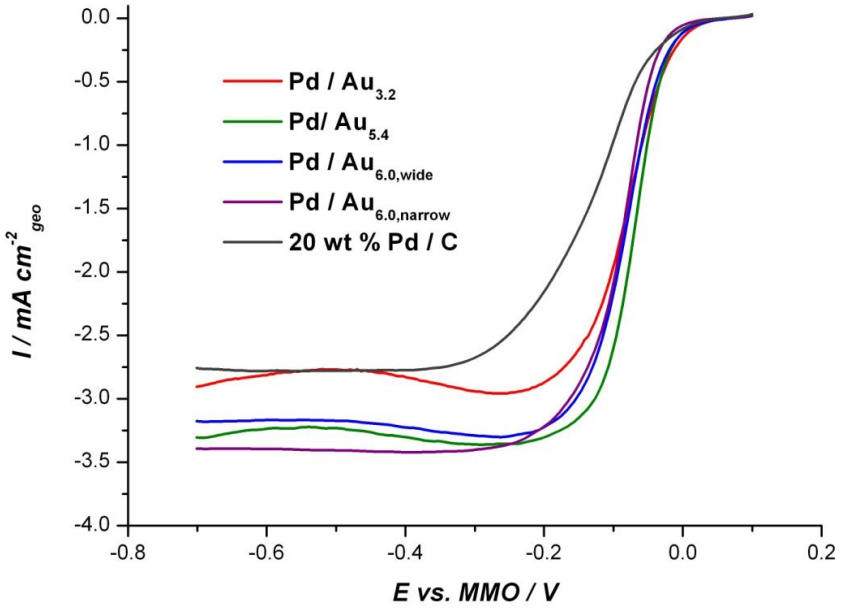


**Figure 5-22: ORR on Pt modified Au catalysts and the 20 wt % Pd/C on GC electrode (geometric area 0.196 $cm^2$) in oxygen saturated 0.5 mol $dm^{-3}$ KOH at 900 rpm. Scan rate 10 mV $s^{-1}$. Only the negative going scans were selected.**

To compare the size dependent activity of the Pd modified Au catalysts, the currents were normalized by the real area of Pd and represented as current density (Figure 5-23).

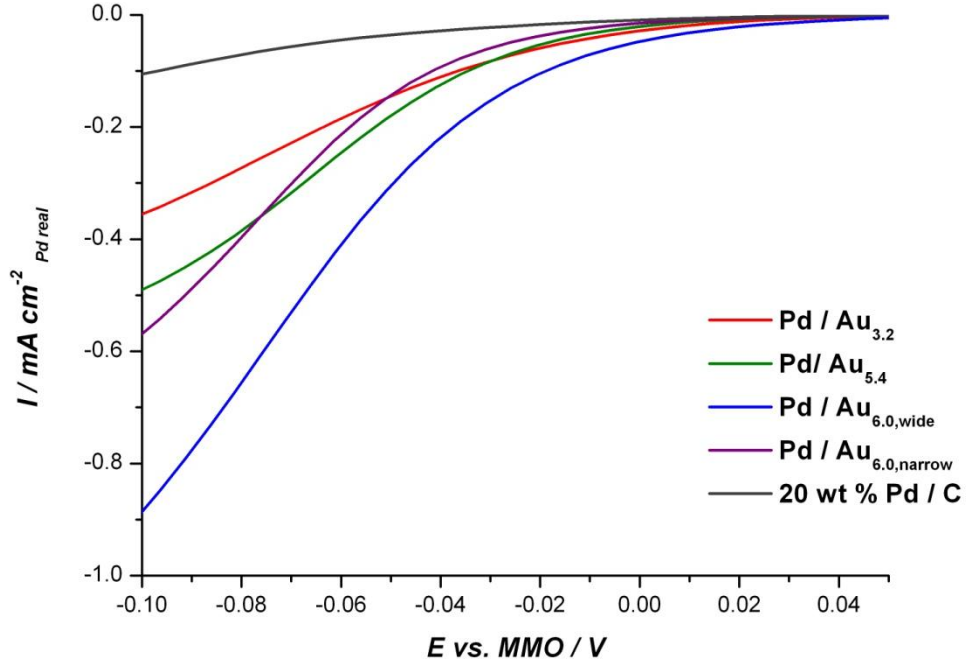


**Figure 5-23: ORR on Pd modified Au catalysts and 20 wt % Pd/C catalyst in oxygen saturated 0.5 mol $dm^{-3}$ KOH at 900 rpm. Scan rate 10 mV $s^{-1}$. Only the negative going scans were selected. The current was normalized by the Pd real area.**

From Figure 5-23 it is obvious that there are considerable differences in activities of the different Pd modified Au catalysts. The onset potential for oxygen reduction is tabulated in Table 5-6.

**Table 5-6: Oxygen reduction polarisation parameters of the Pd modified Au catalysts and the 20 wt % Pd/C.**

| Catalyst | Onset potential of oxygen reduction at 10 μA $cm^{-2}_{Pd}$ / V |
|---|---|
| $Pd/Au_{3.2}$ | 0.02 |
| $Pd/Au_{5.4}$ | 0.02 |
| $Pd/Au_{6.0,\ wide}$ | 0.03 |
| $Pd/Au_{6.0,\ narrow}$ | 0.01 |
| 20 wt % Pd/C | -0.01 |

It is clearly seen from the above Figure that the onset potential for the reduction of oxygen on Pd/C catalyst is more negative compared to the Pd modified catalysts even though there is no significant change amongst the Pd modified Au catalysts.

A Tafel plot was constructed and the specific activity (SA) at a given potential is calculated using the Figure 5-24.

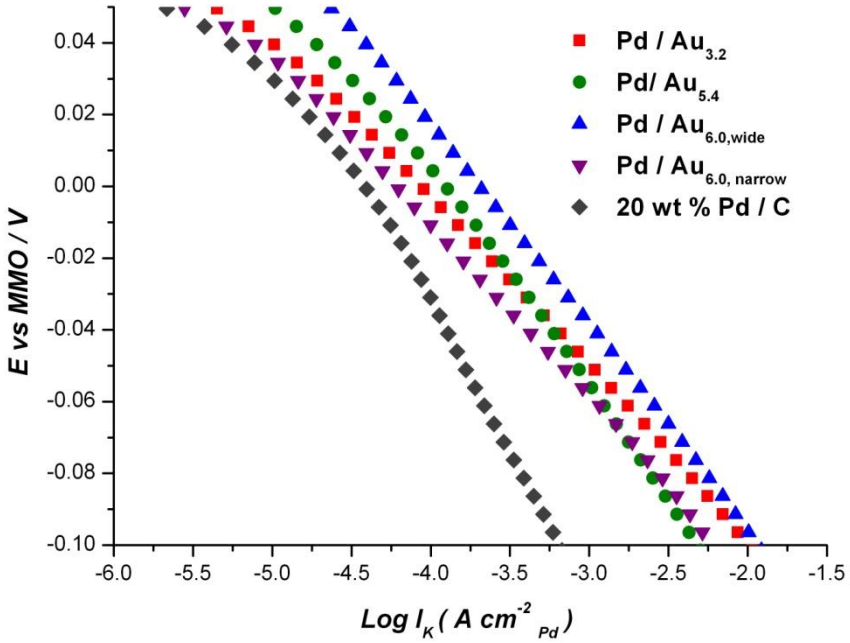


**Figure 5-24: Tafel plot for Pd modified Au catalysts and the 20 wt % Pd/C in oxygen saturated 0.5 mol dm$^{-3}$ KOH at 900 rpm.**

From the Tafel plot the SA values of the Pd modified Au catalysts and 20 wt % Pd /C catalysts were determined at -0.01 V vs. MMO and tabulated in Table 5-7.

**Table 5-7: Kinetic parameters of oxygen reduction on Pd modified Au catalysts on 20 wt % Pd/C and on Au catalysts in 0.5 mol dm$^{-3}$ KOH at rotation speed 900 rpm.**

| Catalyst | SA at -0.03 V / µA cm$^{-2}$ $_{Pd}$ | Au Catalysts | SA at -0.03 V / µA cm$^{-2}$ $_{Au}$ |
|---|---|---|---|
| Pd/Au$_{3.2}$ | 200 | Au$_{3.2}$ | 9 |
| Pd/Au$_{5.4}$ | 202 | Au$_{5.4}$ | 25 |
| Pd/Au$_{6.0,\ wide}$ | 369 | Au$_{6.0,\ wide}$ | 26 |
| Pd/Au$_{6.0,\ narrow}$ | 130 | Au$_{6.0,\ narrow}$ | 33 |
| 20 wt % Pd/C | 50 | | |

In agreement with the Pt modified catalysts, there is no significant change in SA values between the catalysts Pd/Au$_{3.2}$ and Pd/Au$_{5.4}$. However the SA values are

higher in Pd modified catalysts compared to Pt modified catalysts. SA values are increasing with increase in the size of Au particle (increasing the Pd loading).
The enhanced activity of the modified Au catalysts is evidenced of the Au substrate on activity of the Pd surface. Zekerya *et al.*[20] studied the ORR on a Pd ad-layer modified Au (111) electrode in alkaline solution using cyclic voltammetric measurements and they confirmed that the enhanced activity is due to the synergistic effect from Au and Pd, which creates more active surfaces for ORR. Au substrate adsorbs more $OH^-$ and there will be a strong interaction between the adsorbed $O_2$ on Pd and the adsorbed $OH^-$ on Au. As a result O-O bond weakens and hence this facilitates the ORR. The model in Figure 5-18 may also be applicable in this case.

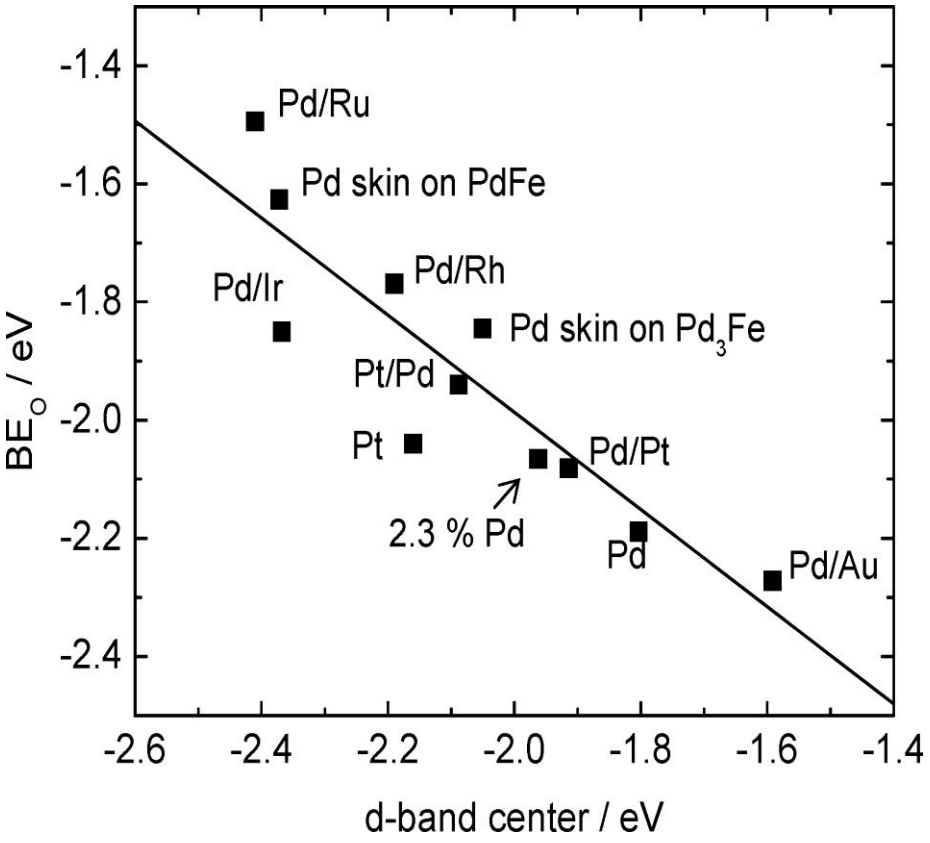


**Figure 5-25: Oxygen binding energies of Pd and Pt over layers against the *d*-band centre of Pd[36].**

According to the above Figure, Pd/Au catalyst has the highest *d*- band centre and as a result there will be a stronger interaction of the 2*p* level of oxygen with the Pd metal *d* orbital. This stronger bond of Pd-O drives the O-O bond cleavage.

# 4. Ethanol Oxidation Reaction

Over the past few years interest has been focused on ethanol oxidation on Pt and Pd based catalysts and significant progress has been made in their development[37-40]. In contrast to gold based catalysts (where acetate is the only product), the oxidation of ethanol on Pt and Pd catalysts proceeds via a dual path mechanism as shown in Figure 5-26.

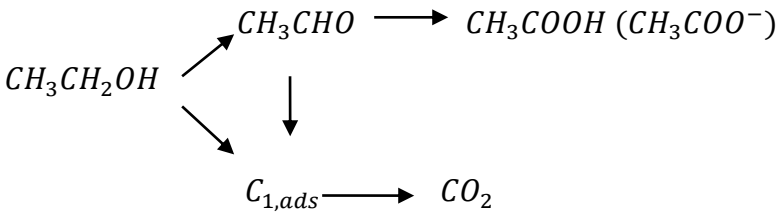


**Figure 5-26: Schematic diagram of the dual oxidation pathway.**

Ethanol can be oxidised to acetaldehyde and consequently to acetic acid (acetate) with the transfer of 4 electrons ($C_2$ pathway). On the other hand, the C-C bond in ethanol or acetaldehyde can be cleaved to yield $CO_{ads}$ and $CH_{x,ads}$, and then these species can subsequently be oxidized to $CO_2$ with the transfer of 12 electrons ($C_1$ pathway). Even though, the $C_1$ pathway is preferred from a fuel cell point of view, it needs a high overpotential and the $C_2$ pathway is the most predominant mechanism while formation of $CO_2$ has only a minor contribution[41].

The aim of this work is to investigate the reactivity of Pt or Pd modified Au catalysts towards the ethanol oxidation reaction. Importance will be placed on advantage of the core/shell structure and the loading of Pt or Pd on Au.

# 4.1 Ethanol oxidation on Pt based catalysts

## 4.1.1 20 wt % Pt/C

Figure 5-27 represents the potentiodynamic measurements of ethanol electro-oxidation on 20 wt % Pt/C catalysts on RDE in $N_2$ saturated 0.2 mol $dm^{-3}$ EtOH + 0.05 mol $dm^{-3}$ KOH solution. The CV of Pt in 0.05 mol $dm^{-3}$ KOH in the absence of ethanol is shown in the inset in the Figure.

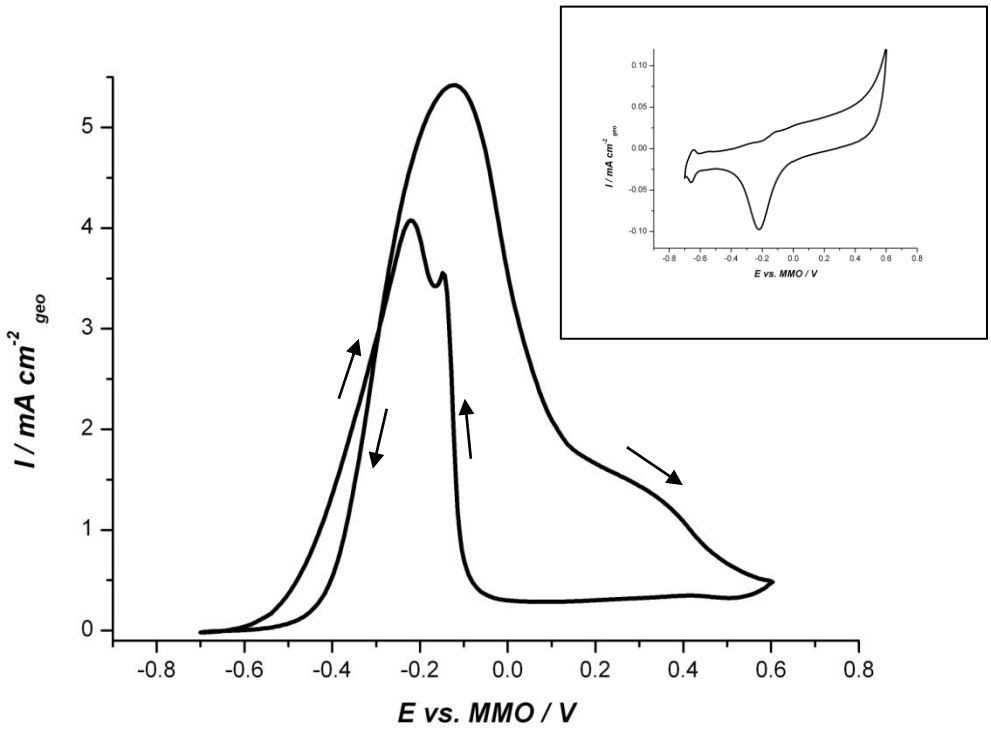


**Figure 5-27: CV curves for ethanol electro-oxidation on 20 wt % Pt/C on GC disc (5mm diameter) in $N_2$ saturated 0.2 mol $dm^{-3}$ EtOH + 0.05 mol $dm^{-3}$ KOH solution. (The inset Figure shows the CV of Pt/C in ethanol free solutions). Scan rate 10 mV $s^{-1}$.**

As revealed from above Figure, the hydrogen desorption/adsorption region is suppressed in the presence of ethanol. In the forward scan, ethanol oxidation starts at ~ -0.6 V, goes to maximum at ~ -0.1 V, and beyond -0.1 V the oxidation current sharply decreases due to the formation of surface oxide. In the reverse scan, ethanol

oxidation reactivates at ~ -0.1 V and goes to maximum at ~ -0.3 V. A small dip in the current at ~ -0.2 V is mainly attributed to the reduction of Pt oxide.

The mechanism of ethanol oxidation on Pt (a parallel path mechanism) was proposed by Tripkovic *et al.*[42]. This included the production of reaction intermediates and the poisoning species. According to this model, initially an ethanol molecule adsorbs on active sites of Pt and reacts with $OH^-$ ions adsorbed on Pt to produce $CH_3CO_{ad}$.

$$CH_3CH_2OH \rightarrow CH_3CH_2OH_{ads} \quad \textbf{[5-10]}$$

$$OH^- \rightarrow OH_{ads} + e^- \quad \textbf{[5-11]}$$

$$CH_3CH_2OH_{ads} + 3OH_{ads} \rightarrow CH_3CO_{ads} + 3H_2O + 3e^- \quad \textbf{[5-12]}$$

Then the reaction intermediate $CH_3CO_{ad}$ interact with $OH_{ad}$ and produce $CH_3COOH$, which will be readily converted to $CH_3COO^-$ in alkaline solution.

$$CH_3CO_{ad} + OH_{ad} \rightarrow CH_3COOH \quad \textbf{[5-13]}$$

$$CH_3COOH + OH^- \rightarrow CH_3COO^- + H_2O \quad \textbf{[5-14]}$$

For the poisoning species $CO_{ads}$,

$$CO_{ads} + 2OH_{ads} + 2OH^- \rightarrow CO_3^{2-} + 2H_2O \quad \textbf{[5-15]}$$

Therefore, $OH^-$ ions are crucial for the electro-oxidation of ethanol. However, the coverage of $OH_{ads}$ increases with increasing potential. At higher potentials the reversible $OH_{ads}$ will be transformed to irreversible Pt-OH bond and hence it could be further converted to PtO. As a result the rate of ethanol oxidation slows down and eventually stops[38].

## 4.1.2 Pt modified Au catalysts

Figure 5-28 shows the ethanol oxidation reaction on one of the Pt modified Au catalysts (Pt/ $Au_{6,narrow}$) in $N_2$-saturated 0.2 mol $dm^{-3}$ EtOH + 0.05 mol $dm^{-3}$ KOH.

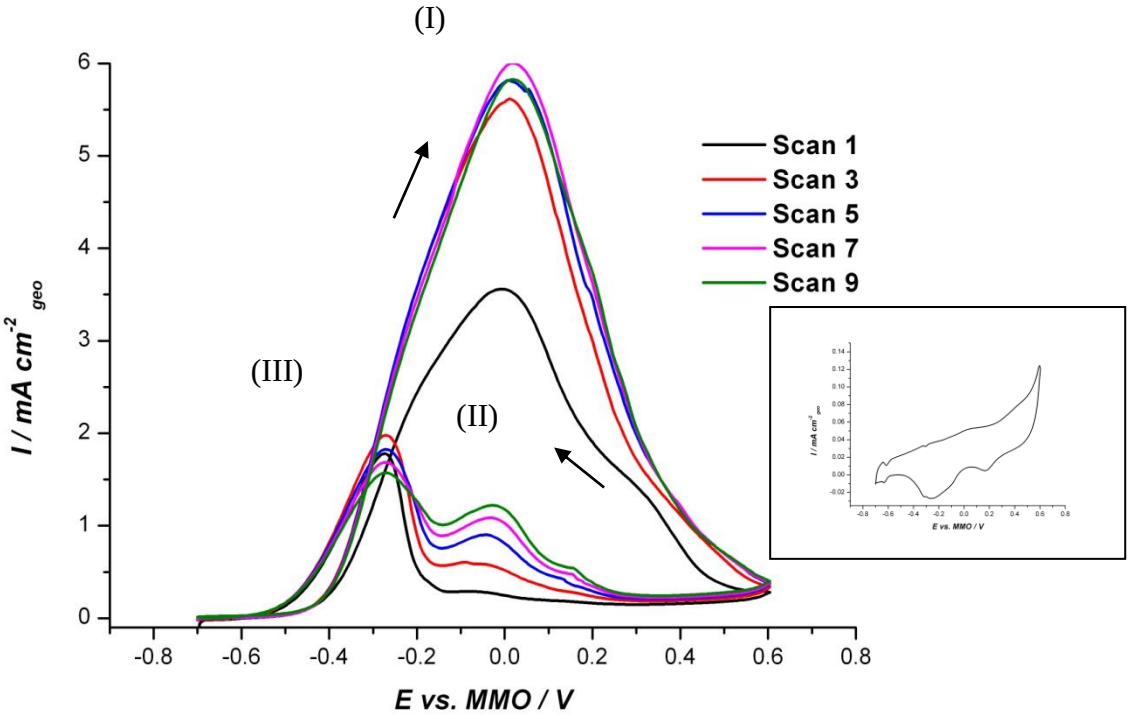


**Figure 5-28: Cyclic voltammograms for Pt/ $Au_{6, narrow}$ on GC disc (5mm diameter)in $N_2$ saturated 0.2 mol $dm^{-3}$ EtOH + 0.05 mol $dm^{-3}$ KOH at a scan rate 10 mV $s^{-1}$. (Inset Figure shows the CV of Pt/$Au_{6, narrow}$ in ethanol free solutions.**

It can be confirmed from Figures 4-21 (Chapter four) and 5-31 that the peak I corresponds to the oxidation of ethanol on both Pt and Au surfaces. As seen in inset Figure, the stripping of Au oxide and Pt oxide occurs at ~ 0.2 V and -0.2 V respectively. Therefore, the peaks II and III should belong to the reactivation of ethanol oxidation on Au and Pt surfaces correspondingly.

Careful consideration of the Figure 5-28 shows that peaks I and III increase up to a certain number of scans and then decay, whilst, on the other hand, peak II continuously increases. This is primarily due to the increase in exposed Au sites on

the electrode surface. As the electrode is cycled; either the Pt is stripped off the Au and lost in to the solution or the Pt and Au mix, exposing Au on the surface.

Therefore to maintain the consistency only the first scan was selected to compare the activity of these catalysts in all cases.

Figure 5-29 shows representative current–potential curves for the ethanol oxidation at the Pt modified Au/C catalysts on the RDE in $N_2$-saturated 0.2 mol $dm^{-3}$ EtOH + 0.05 mol $dm^{-3}$ KOH.

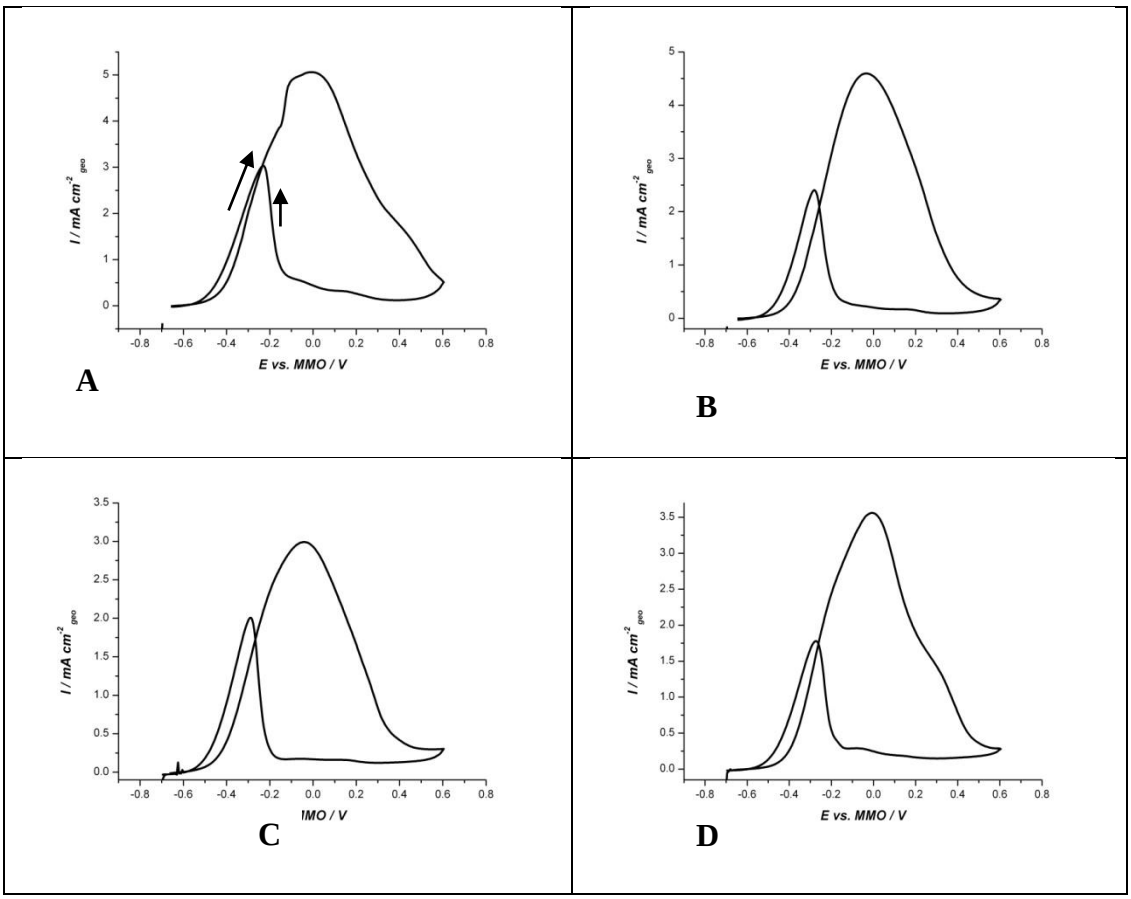


**Figure 5-29: Cyclic voltammograms for (A) $Pt/Au_{3.2}$, (B) $Pt/Au_{5.4}$, (C) $Pt/Au_{6.0,wide}$ and (D) $Pt/Au_{6.0,narrow}$ on GC electrode (5 mm diameter) in $N_2$ saturated 0.2 mol $dm^{-3}$ EtOH + 0.05 mol $dm^{-3}$ KOH at a scan rate 10 mV $s^{-1}$.**

The CV features of the Pt modified Au catalysts are similar to those observed for 20 wt % Pt/C catalyst. However, the ethanol oxidation on Au sites is also observed on Pt modified Au catalysts in the range of 0.2 V to 0 V.

To compare the activities of the catalysts, the current (A) and the current density (B) of the Pt modified Au catalysts are plotted in Figure 5-30.

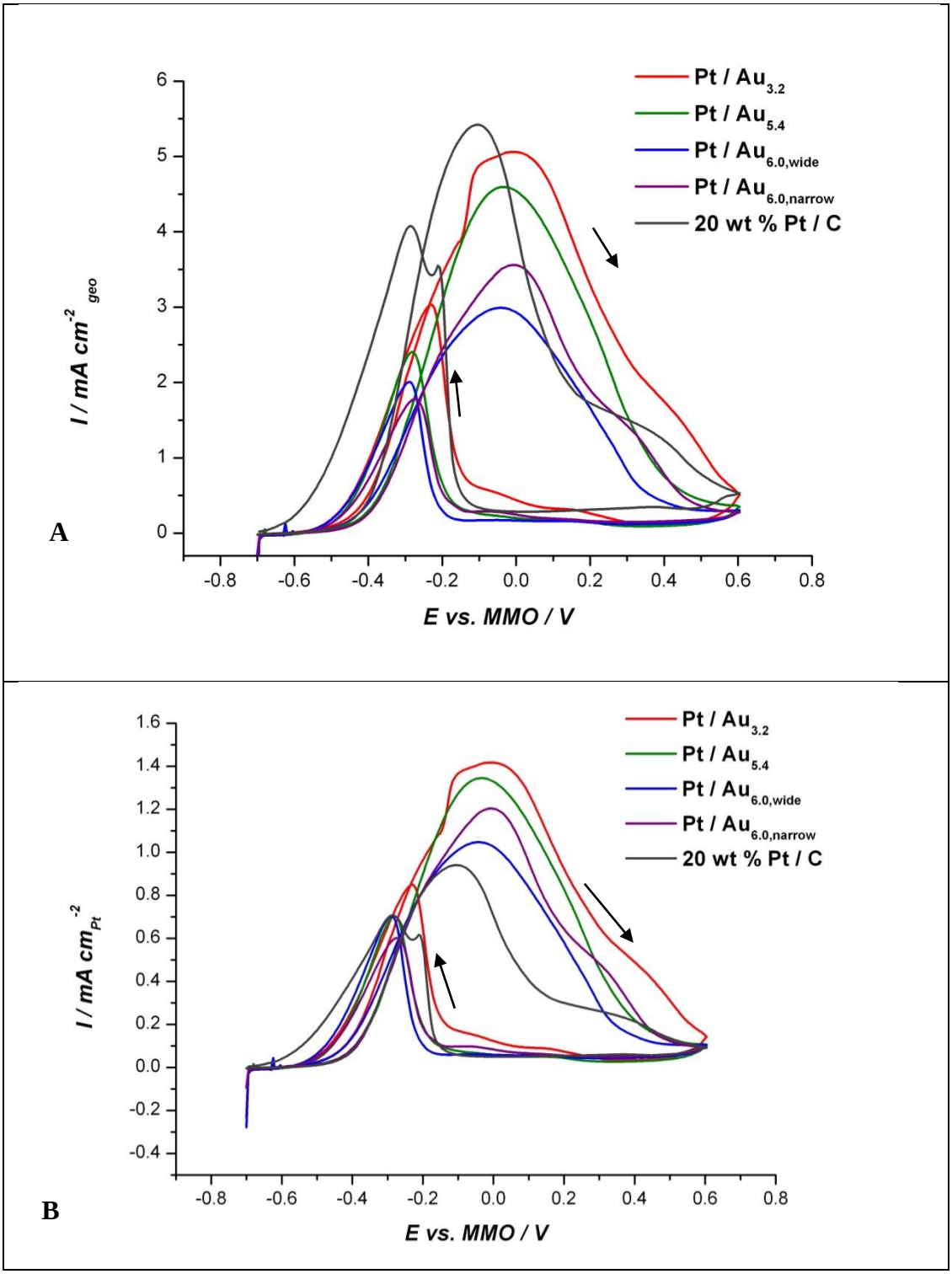


**Figure 5-30: Comparison of the catalysts in $N_2$ saturated 0.2 mol $dm^{-3}$ EtOH + 0.05 mol $dm^{-3}$ KOH. Scan rate 10 mV $s^{-1}$. (A) Total metal loading (B) specified Pt metal loading and the current was normalized by the Pt real area.**

Figure 5-30 (A) shows the ethanol oxidation activity on both Pt and Au catalysts. Figure 5-30 (B) shows that the activities of Pt modified Au catalysts are coverage dependent. Furthermore, the ethanol oxidation increases with the decrease in the coverage of Pt. This is due to the increase in remaining Au sites with decrease in coverage of Pt (Table 5-2). The onset potential for the oxidation and their corresponding current densities are tabulated in Table 5-8.

**Table 5-8: Ethanol oxidation parameters for the Pt modified Au catalysts.**

| Catalysts | Anodic onset potential at 20 μA $cm^{-2}_{Pt}$/ V | Anodic peak current density / mA $cm^{-2}_{Pt}$ | Cathodic peak current density/ mA $cm^{-2}_{Pt}$ |
|---|---|---|---|
| $Pt/Au_{3.2}$ | -0.49 | 1.42 | 0.85 |
| $Pt/Au_{5.4}$ | -0.48 | 1.34 | 0.71 |
| $Pt/Au_{6.0,wide}$ | -0.50 | 1.04 | 0.71 |
| $Pt/Au_{6.0,narrow}$ | -0.49 | 1.20 | 0.60 |
| 20 wt % Pt/C | -0.47 | 0.94 | 0.71 |

Even though, there is no discernible difference between the onset potentials of the modified catalysts, the activity of the catalysts varies in their anodic current densities. Higher anodic current density observed for the lower coverage of Pt ($Pt/Au_{3.2}$). In addition, it is worth noting, that the Pt modified Au catalysts show superior activity over the Pt/C catalyst. The activity enhancement is mainly attributed to the presence of Au underneath a very thin layer of Pt. The electron transfer between the Pt and Au will promote active oxygen species ($OH^-$) on Pt and as a result facilitates the reaction kinetics. Furthermore, a thin shell provides a greater number of Pt-Au interface per Pt atom and this leads to a higher activity of the lower Pt loading catalyst[43].

# 4.2 Ethanol oxidation on Pd based catalysts

## 4.2.1 20 wt % Pd/C

A mechanism of ethanol oxidation on Pd catalyst was proposed by Liang *et al*.[39] This is similar to that proposed for Pt catalyst. Figure 5-31 shows the CV curve of ethanol electro-oxidation on 20 wt % Pd/C catalysts on RDE in $N_2$ saturated 0.2 mol $dm^{-3}$ EtOH + 0.05 mol $dm^{-3}$ KOH solution.

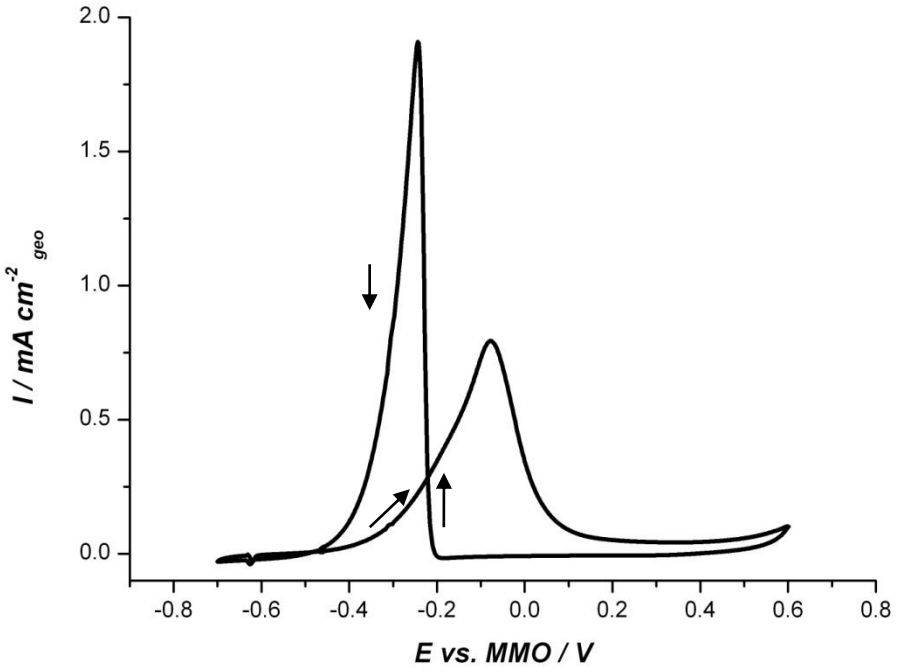


**Figure 5-31: CV curves for ethanol electro-oxidation on 20 wt % Pd / C on GC disc(5mm diameter)in $N_2$ saturated 0.2 mol $dm^{-3}$ EtOH + 0.05 mol $dm^{-3}$ KOH solution. Scan rate 10 mV $s^{-1}$.**

In the positive going scan the ethanol oxidation begins at ~ -0.5 V and a current peak centred at ~ -0.1 V is observed. In the reverse scan, the oxidation current starts to increase at ~ -0.2 V and a current peak is found centred at ~ -0.3V. Strong adsorption of ethoxy intermediate $CH_3CO_{ad}$ on Pd surface blocks the H absorption/ adsorption thus reducing the H peaks. The CV features are similar to the behaviour observed with the Pt catalyst, however a larger current was observed on the reverse sweep

compared in Pd catalysts. The reason may be due to the poisoning of Pt by adsorbed species coming from the dissociative adsorption of ethanol[40].

## 4.2.2 Pd modified Au catalysts

Figure 5-32 shows representative current–potential curves for the ethanol oxidation of Pd modified Au/C catalysts on the RDE in $N_2$-saturated 0.2 mol $dm^{-3}$ EtOH + 0.05 mol $dm^{-3}$ KOH. As explained in Figure 5-33 only the first scan was selected.

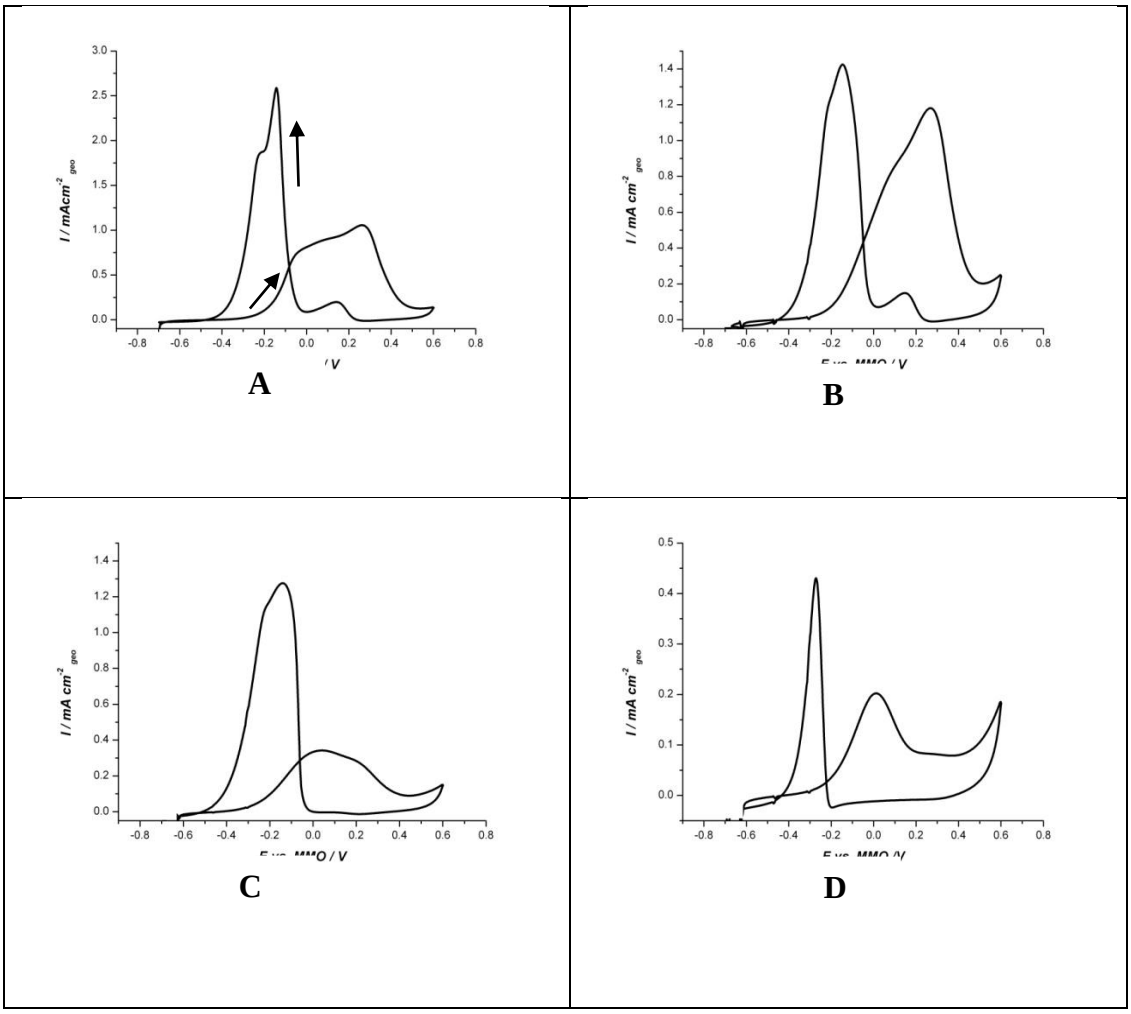


**Figure 5-32: Cyclic voltammograms for (A) $Pd/Au_{3.2}$, (B) $Pd/Au_{5.4}$, (C) $Pd/Au_{6.0,wide}$ and (D) $Pd/Au_{6.0,narrow}$ on GC electrode (5 mm diameter) in $N_2$ saturated 0.2 mol $dm^{-3}$ EtOH + 0.05 mol $dm^{-3}$ KOH at a scan rate 10 mV $s^{-1}$.**

To compare the activities of the Pd modified Au catalysts, the scans from each of the catalysts are plotted in the same Figure (Figure 5-33).

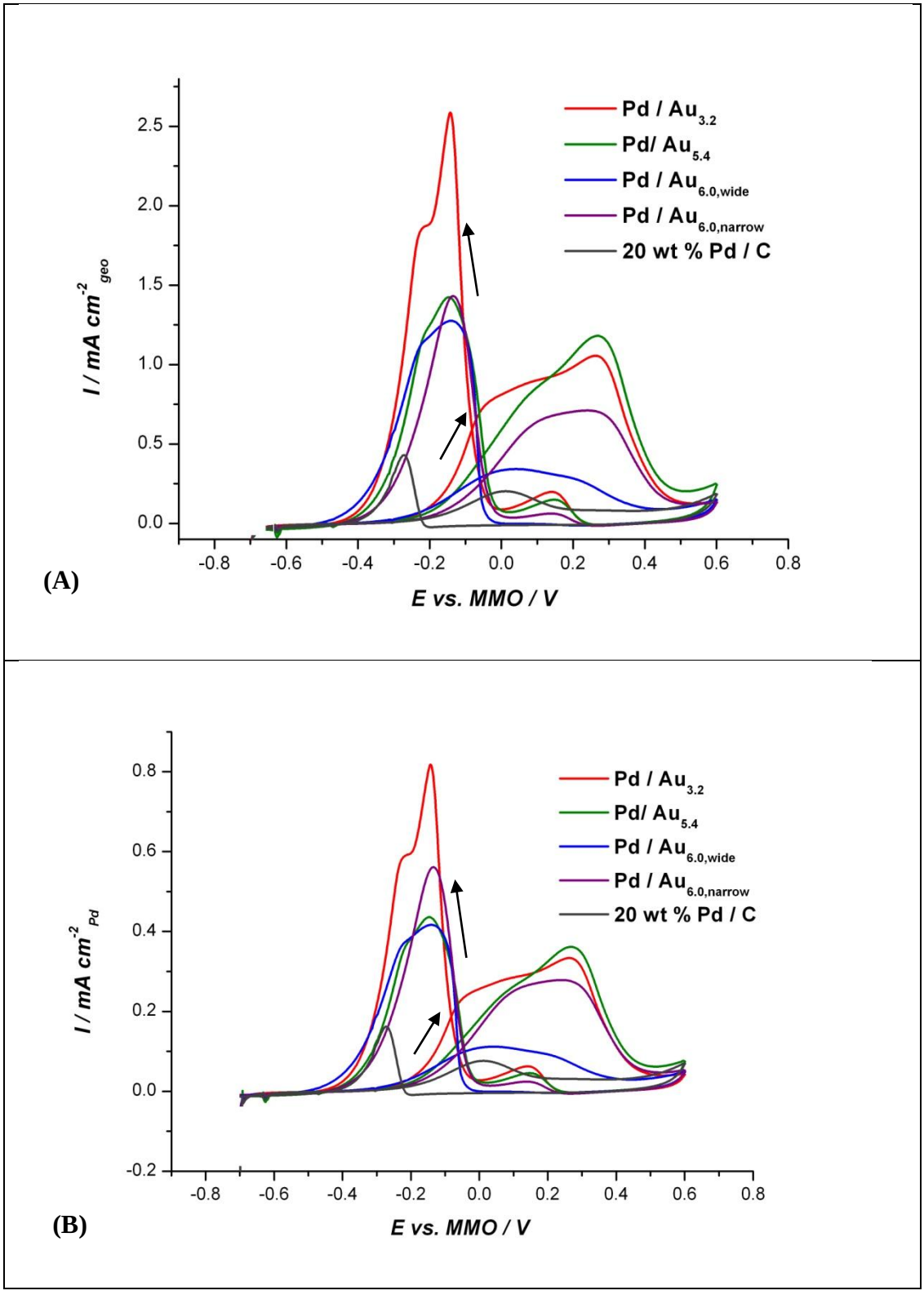


**Figure 5-33: Comparison of the catalysts in $N_2$ saturated 0.2 mol $dm^{-3}$ EtOH + 0.05 mol $dm^{-3}$ KOH. Scan rate 10 mV $s^{-1}$. (A) Total metal loading (B) specified Pd metal loading and the current was normalized by the Pd real area.**

Similar to the Pt modified catalysts, in the backward scan the ethanol oxidation on Au sites was observed in the potential region between 0 V and 0.2 V and this current increases with decrease in size of Au (decrease in Pt coverage).

The onset potential for the oxidation and their corresponding current densities are tabulated in Table 5-9.

**Table 5-9: Ethanol oxidation parameters for the Pd modified Au catalysts and the 20 wt % Pd/C catalyst.**

| Catalysts | Anodic onset potential at 20 μA $cm^{-2}{}_{Pt}$ / V | Anodic peak current density / mA $cm^{-2}{}_{Pd}$ | Cathodic peak current density / mA $cm^{-2}{}_{Pd}$ |
|---|---|---|---|
| $Pd/Au_{3.2}$ | -0.23 | 0.33 | 0.81 |
| $Pd/Au_{5.4}$ | -0.21 | 0.36 | 0.44 |
| $Pd/Au_{6.0,wide}$ | -0.24 | 0.11 | 0.41 |
| $Pd/Au_{6.0,narrow}$ | -0.19 | 0.28 | 0.56 |
| 20 wt % Pd / C | -0.16 | 0.08 | 0.16 |

Although there is no trend in onset potentials for the oxidation of ethanol on the catalysts, they vary in their current densities. The anodic and cathodic current densities of the Pd modified catalysts are larger compared to the Pd/C catalysts, this indicates the superior activity of the Pd modified catalysts. This is due to the enhanced activity of Au that increases the poisoning tolerance of the Pd modified catalysts. Faliang Cheng and co-workers[44] explained this superior activity using the synergic effect of Au and Pd. In general, Pd acts as active sites for the dehydrogenation of ethanol while Au is capable of oxidising CO like intermediates and prevents the interaction between the Pd as follows.

$$CO_{ads} + Au - OH_{ads} \rightarrow Au - CO - OH \rightarrow Au - COOH \rightarrow Au + CO_2 + H_2O \quad \textbf{[5-16]}$$

There are a few reports demonstrating the enhanced activity of the Pd modified catalysts. Zhu *et al.*[45] prepared the Pd monolayer or sub-monolayer on Au/C catalysts by controlling the Pd:Au atomic ratio using epitaxial growth method. They confirmed that the superior activity of the modified catalysts is due to the electronic interaction between the Au support and the Pd.

Considering the Tables 5-8 and 5-9, it is apparent that the current densities are larger at corresponding potentials on Pt/C catalysts compared to that on Pd/C catalyst. In addition, the onset potential for ethanol oxidation on Pt/C catalyst is more negative for 170 mV (in anodic direction) compared with that on Pd/C catalyst. Therefore the results show that Pt has superior activity for ethanol oxidation compared to Pd. However, the above results are in contradiction with Xu *et al.*[40] who studied the ethanol oxidation of Pt/C and Pd/C catalysts in alkaline media. Furthermore, the results from this work also confirm the superior activity of the Pt modified catalysts in comparison of the Pd modified catalysts.

Even though the size dependent activity is not clearly seen in both Pt and Pd modified Au catalysts, the enhanced activities of these modified catalysts were observed compared to monometallic Pt or Pd catalysts. Furthermore, this work also confirms that the addition of a monolayer of Pt or Pd enhances the activity of the gold based catalysts. A more negative onset potential as well as the larger current densities for the oxidation of modified catalysts makes them superior in the electro oxidation of ethanol compared to Au catalysts. In addition, the final product of ethanol oxidation on gold is acetate with 4 electrons transfer. However, on the modified catalysts the analysis for the carbonate in the resultant solution (effervescence with 1 mol $dm^{-3}$ $H_2SO_4$) was positive. This is the indication of the 12 electron transfer reaction with the cleavage of C – C bond.

# 5. Conclusion

In this work Pt or Pd modified Au catalysts were successfully prepared using the Cu UPD redox replacement techniques. In all the electrochemical reactions, these Pt or Pd modified Au catalysts exhibit enhanced activity compared to the monometallic Pt, Pd and Au. Furthermore, the coverage dependent activity was also observed among the modified catalysts. Higher Au surface coverage by Pt or Pd enhances the reduction of oxygen while the lower coverage of Pt or Pd facilitates the ethanol oxidation reactions. The possible reason can be explained using the hydroxyl coverage. Stronger adsorption of hydroxyl ions on lower coverage of Pt or Pd makes ethanol oxidation reaction (where it occurs at more negative potentials) more facile while the stronger adsorption of hydroxyl ions on lower coverage of Pt or Pd retards the oxygen reduction reaction (where it happens at comparatively positive potentials) by blocking the active sites.

However, the major disadvantage of the modified catalysts is the instability during the reactions. Dissolution of Pt or Pd occurs at higher anodic potentials. This is severe in the ethanol oxidation reaction where the scan goes to a very high potential. Therefore the conclusion can be made is that one monolayer is not sufficient for the stability and it needs at least two monolayers.

# 6. References


(1) Luo, J.; Wang, L.; Mott, D.; Njoki, P. N.; Lin, Y.; He, T.; Xu, Z.; Wanjana, B. N.; Lim, I. I. S.; Zhong, C. J. *Advanced Materials* **2008**, *20*, 4342.

(2) Kristian, N.; Wang, X. *Electrochemistry Communications* **2008**, *10*, 12.

(3) Kristian, N.; Yu, Y.; Gunawan, P.; Xu, R.; Deng, W.; Liu, X.; Wang, X. *Electrochimica Acta* **2009**, *54*, 4916.

(4) Luo, J.; Wang, L.; Mott, D.; Njoki, P. N.; Lin, Y.; He, T.; Xu, Z.; Wanjana, B. N.; Lim, I. I. S.; Zhong, C.-J. *Advanced Materials* **2008**, *20*, 4342.

(5) Zhang, J.; Vukmirovic, M. B.; Xu, Y.; Mavrikakis, M.; Adzic, R. R. *Angewandte Chemie International Edition* **2005**, *44*, 2132.

(6) Baldauf, M.; Kolb, D. M. *The Journal of Physical Chemistry* **1996**, *100*, 11375.

(7) Yu, Y.; Hu, Y.; Liu, X.; Deng, W.; Wang, X. *Electrochimica Acta* **2009**, *54*, 3092.

(8) Zhang, J.; Lima, F. H. B.; Shao, M. H.; Sasaki, K.; Wang, J. X.; Hanson, J.; Adzic, R. R. *The Journal of Physical Chemistry B* **2005**, *109*, 22701.

(9) Tang, H.; Chen, J. H.; Wang, M. Y.; Nie, L. H.; Kuang, Y. F.; Yao, S. Z. *Applied Catalysis A: General* **2004**, *275*, 43.

(10) Junfeng Zhai, M. H., Shaojun Dong, *Electroanalysis* **2007**, *19*, 506.

(11) Doña Rodríguez, J. M.; Herrera Melián, J. A.; Pérez Peña, J. *Journal of Chemical Education* **2000**, *77*, 1195.

(12) Conway, B. E. *Progress in Surface Science* **1995**, *49*, 331.

(13) Vidakovic, T.; Christov, M.; Sundmacher, K. *Electrochimica Acta* **2007**, *52*, 5606.

(14) Park, I.-S.; Lee, K.-S.; Jung, D.-S.; Park, H.-Y.; Sung, Y.-E. *Electrochimica Acta* **2007**, *52*, 5599.

(15) Hammer, B.; Nørskov, J. K. In *Advances in Catalysis*; Bruce C. Gates, H. K., Ed.; Academic Press: 2000; Vol. Volume 45, p 71.

(16) Rincón, A.; Pérez, M. C.; Gutiérrez, C. *Electrochimica Acta* **2010**, *55*, 3152.

(17) Du, B.; Tong *The Journal of Physical Chemistry B* **2005**, *109*, 17775.

(18) Hoshi, N.; Kagaya, K.; Hori, Y. *Journal of Electroanalytical Chemistry* **2000**, *485*, 55.

(19) Kunimatsu, K. *The Journal of Physical Chemistry* **1984**, *88*, 2195.

(20) Dursun, Z.; Ulubay, Ş.; Gelmez, B.; Ertaş, F. *Catalysis Letters* **2009**, *132*, 127.

(21) Genies, L.; Faure, R.; Durand, R. *Electrochimica Acta* **1998**, *44*, 1317.

(22) Tammeveski, K.; Tenno, T.; Claret, J.; Ferrater, C. *Electrochimica Acta* **1997**, *42*, 893.

(23) Elezovic.N.R, B. B. M., Vracar.LJ.M,Krstajc.N.V *J. Serb. Chem. Soc.* **2007**, *72*, 699.

(24) Jin, W.; Du, H.; Zheng, S.; Xu, H.; Zhang, Y. *The Journal of Physical Chemistry B* **2010**, *114*, 6542.

(25) Jiang, L.; Hsu, A.; Chu, D.; Chen, R. *Journal of The Electrochemical Society* **2009**, *156*, B370.

(26) Luo, J.; Njoki, P. N.; Lin, Y.; Wang, L.; Zhong, C. J. *Electrochemistry Communications* **2006**, *8*, 581.

(27) Vukmirovic, M. B.; Zhang, J.; Sasaki, K.; Nilekar, A. U.; Uribe, F.; Mavrikakis, M.; Adzic, R. R. *Electrochimica Acta* **2007**, *52*, 2257.

(28) Zhang, J.; Sasaki, K.; Sutter, E.; Adzic, R. R. *Science* **2007**, *315*, 220.

(29) Li, X.; Liu, J.; He, W.; Huang, Q.; Yang, H. *Journal of Colloid and Interface Science* **2010**, *344*, 132.

(30) Nørskov, J. K.; Rossmeisl, J.; Logadottir, A.; Lindqvist, L.; Kitchin, J. R.; Bligaard, T.; Jónsson, H. *The Journal of Physical Chemistry B* **2004**, *108*, 17886.

(31) Norskov, J. K.; Bligaard, T.; Rossmeisl, J.; Christensen, C. H. *Nat Chem* **2009**, *1*, 37.

(32) Cui, G.; Song, S.; Shen, P. K.; Kowal, A.; Bianchini, C. *The Journal of Physical Chemistry C* **2009**, *113*, 15639.

(33) Grden, M.; Lukaszewski, M.; Jerkiewicz, G.; Czerwinski, A. *Electrochimica Acta* **2008**, *53*, 7583.

(34) Huang, Y.; Zhou, X.; Liao, J.; Liu, C.; Lu, T.; Xing, W. *Electrochemistry Communications* **2008**, *10*, 621.

(35) Liu, Z.; Hong, L.; Tham, M. P.; Lim, T. H.; Jiang, H. *Journal of Power Sources* **2006**, *161*, 831.

(36) Shao, M.; Liu, P.; Zhang, J.; Adzic, R. *The Journal of Physical Chemistry B* **2007**, *111*, 6772.

(37) de Souza, J. P. I.; Queiroz, S. L.; Bergamaski, K.; Gonzalez, E. R.; Nart, F. C. 2002; Vol. 106, p 9825.

(38) Jiang, L.; Hsu, A.; Chu, D.; Chen, R. *International Journal of Hydrogen Energy* **2010**, *35*, 365.

(39) Liang, Z. X.; Zhao, T. S.; Xu, J. B.; Zhu, L. D. *Electrochimica Acta* **2009**, *54*, 2203.

(40) Xu, C.; Shen, P. k.; Liu, Y. *Journal of Power Sources* **2007**, *164*, 527.

(41) Lai, S. C. S.; Kleyn, S. E. F.; Rosca, V.; Koper, M. T. M. *The Journal of Physical Chemistry C* **2008**, *112*, 19080.

(42) Tripkovic, A. V.; Popovic, K. D.; Lovic, J. D. *Electrochimica Acta* **2001**, *46*, 3163.

(43) Zeng, J.; Yang, J.; Lee, J. Y.; Zhou, W. *The Journal of Physical Chemistry B* **2006**, *110*, 24606.

(44) Cheng, F.; Dai, X.; Wang, H.; Jiang, S. P.; Zhang, M.; Xu, C. *Electrochimica Acta* **2010**, *55*, 2295.

(45) Zhu, L. D.; Zhao, T. S.; Xu, J. B.; Liang, Z. X. *Journal of Power Sources* **2009**, *187*, 80.

# Chapter Six: Conclusion

The major aim of this work was to determine the effects of particle size for gold based nanoparticular catalysts in the process of electrocatalysis. The gold nanoparticles were prepared using thiol as an encapsulating agent and loaded on to Vulcan carbon powder support. Then appropriate heat treatment techniques were applied to prepare different sizes of Au. The catalysts have been mainly characterized by TEM, XRD, EXAFS and cyclic voltammetric measurements including UPD techniques.

Chapter three explained the general characterization of the catalysts. TEM results revealed that the particles are less than 10 nm in diameter and showed a clear size difference amongst the catalysts. XRD and UPD techniques confirm the crystallinity of the catalysts and the presence of Au (110) and Au (111) facets. EXAFS analysis proved the purity of the catalyst and the retention of the FCC structure, while confirming a near spherical particle shape. All the above characterization techniques validate the spherical nature of the particle.

Chapter four detailed the size dependent activity of these catalysts towards the oxygen reduction, ethanol oxidation and carbon monoxide oxidation reactions. Superior activity was observed in alkaline media due to the activation of the Au electrode by the partially discharged hydroxyl ions. Two electron reduction was observed during the reduction of one molecular oxygen. This can be explained by the absence of Au (100) facet which is normally responsible for the four electron reduction reaction. Enhanced activity of CO oxidation was observed on gold catalysts where adsorbed CO usually blocks the active sites of Pt. Further, the gold catalysts showed considerable activity towards the oxidation of ethanol. However the activity is lower compared to the bulk gold. Amongst the prepared gold catalysts, size dependent activity is clearly seen towards the above electrochemical reactions. The results showed that the smaller catalysts favour the CO oxidation reaction while

the larger particular catalysts favour the ethanol oxidation and oxygen reduction reactions. The difference in activity towards the electrochemical reactions on different sizes of Au catalysts can be explained with the aid of hydroxyl ion adsorption. In this work only three different sizes of Au catalysts were analysed over a limited size range. Most of the works in the literature have been shown that the activity of the catalysts decreases beyond a certain size of Au[1-5]. Therefore, further investigation should be carried out to validate the above results.

However, gold alone is not the most active catalyst in the process of electrocatalysis. The second aim of this work was to explore the enhancement of the catalytic properties of gold modified by a Pt or Pd monolayer by means of redox replacement of Cu. In this work Pt or Pd was successfully deposited on Au surface. However the complete monolayer was not obtained using this method. Chapter five detailed the activity of Pt or Pd modified catalysts towards the oxygen reduction and ethanol oxidation reactions. Enhanced activity of these modified catalysts was observed compared to the monatomic Pt, Pd or Au catalyst. Electrochemical measurements indicated that the presence of Au enhanced the activity towards the reactions. In addition to that, Pt or Pd coverage dependent (dependency on Au core size) activity was also observed amongst the modified catalysts. Higher coverage of Pt or Pd (larger Au core) increases the activity of the oxygen reduction reaction. However, the lower coverage of Pt or Pd (smaller Au core) increases the ethanol oxidation reaction. However, Pt or Pd dissolution was observed during the electrochemical reactions, which lead to the instability of the catalysts. This is worse in the case of ethanol oxidation reaction where the scan goes to a more positive potential value and, at this higher potential, stripping of Pt or Pd occurs. Therefore, further work should be carried out using two monolayers of Pt or Pd instead to explore the effects on stability. Moreover, another disadvantage is that the preparation method is not suitable for large scale applications. Therefore further investigations should be carried out to use replace the UPD replacement technology with another surface modification strategy.

Finally, this work has shown the enhanced catalytic properties of gold based catalysts. Further, this work also has proved that, it is possible to enhance the oxygen reduction and ethanol oxidation activity with reduced Pt or Pd content by using the core–shell structure electrocatalysts.

# References

(1) Haruta, M.; Tsubota, S.; Kobayashi, T.; Kageyama, H.; Genet, M. J.; Delmon, B. *Journal of Catalysis* **1993**, *144*, 175.

(2) Valden, M.; Lai, X.; Goodman, D. W. *Science* **1998**, *281*, 1647.

(3) Sun, K.-Q.; Luo, S.-W.; Xu, N.; Xu, B.-Q. *Catalysis Letters* **2008**, *124*, 238.

(4) Guan, Y.; Hensen, E. J. M. *Applied Catalysis A: General* **2009**, *361*, 49.

(5) Inasaki, T.; Kobayashi, S. *Electrochimica Acta* **2009**, *54*, 4893.